Title
Structural and Functional Adaptive Optics Retinal Imaging

Author
Mozaffari, Sanam

Publication Date
2021

Peer reviewed|Thesis/dissertation

Structural and Functional Adaptive Optics Retinal Imaging

By

Sanam Mozaffari

A dissertation submitted in partial satisfaction of the

requirements for the degree of

Doctor in Philosophy

in

Vision Science

in the

Graduate Division

of the

University of California, Berkeley

Committee in charge:

Professor Austin Roorda, Chair
Professor Richard Kramer
Professor Laura Waller

Spring 2021

Structural and Functional Adaptive Optics Retinal Imaging

by Sanam Mozaffari

Abstract

Structural and Functional Adaptive Optics Retinal Imaging

by

Sanam Mozaffari

Doctor of Philosophy in Vision Science

University of California Berkeley

Professor Austin Roorda, Chair

Ophthalmic technologies have evolved over the past ten years to not only resolve every photoreceptor within the densely packed fovea, but also to reveal hidden structures within the translucent retinal layers. Although structurally intact, patches of seemingly healthy photoreceptors could have a decreased sensitivity indicating signs of pathology with no structural discrepancies visible. To better understand the health of the retina we have further developed both structural and functional retinal imaging to shed light on the photoreceptors as a more precise indicator of health by probing the sensitivity and physical elongation of these neurons upon stimulation. With a cellular-scale tool which can quantify both the neuron's structure and function, the health of the retina can be precisely monitored and probed to bring new insights into pathophysiology and diagnostics of retinal diseases.

Adaptive optics scanning laser ophthalmoscopy (AOSLO) is a powerful tool for imaging the retina at high spatial and temporal resolution. In this dissertation, four developments are documented based on AOSLO technology for imaging the structure and function of the retina.

Firstly, a wide-vergence, multi-spectral AOSLO was designed, constructed, and experimentally verified by measuring the point spread function (PSF) of the illumination and collection paths for each spectral channel via a phase retrieval technique. The system's optical quality was then demonstrated by resolving the foveal cone mosaic in all three imaging channels from human volunteers and comparing against expected performance.

Secondly, a multi-detector scheme for AOSLO with two main detection configurations was developed: pixel reassignment and offset aperture imaging. In the multi-detector scheme, the single element detector of the standard AOSLO was replaced by a fiber bundle which couples the detected light into multiple detectors. The pixel reassignment configuration enabled high resolution imaging with an increased light collection efficiency. The offset aperture imaging configuration enhanced the detection of multiply scattered light, which improves the contrast of retinal vasculature and inner retinal layers.

Thirdly, an additional system was built with active eye motion correction for an optical coherence tomography (OCT). The AOSLO was an integral part for driving the aberration correction and tracking the eye motion to guide the AOOCT. An independent focus adjustment was implemented into the AOOCT path for imaging the nerve fiber layers and ganglion cells

with optimal lateral resolution while maintaining high fidelity photoreceptor mosaic for AOSLO tracking.

Lastly, by using the complex field from measured AOOCT interferogram, the phase information was acquired to measure the physiological response of the photoreceptors with nm scale accuracy and record the elongation of the cone outer segment in response to a stimulus. This system successfully characterized the optoretinogram of photoreceptors which has potential to be further utilized as an optical biomarker for the function of the neuron allowing both the classification of the cone type and the assessment of the photoreceptor's health.

Table of Contents

List of Figures

Chapter 1:

Chapter 2:

Chapter 3:

Chapter 4:

Chapter 5:

List of Abbreviations

ANSI: American National Standard Institute
AO: Adaptive optics
AOM: Acousto-optic modulator
AOOCT: Adaptive optics optical coherence tomography
AOSLO: Adaptive optics scanning laser ophthalmoscopy
CM: Curved mirror
COST: Cone Outer Segment Tips
DAC: Digital-to-analog converter
dB: Decibels
DM: Dichroic Mirror
FFT: Fast Fourier transform
FOV: Field of view
FPGA: Field programmable gate array
FT: Fourier transform
FWHM Full width at half maximum
GCL Ganglion cell layer (of the retina)
Hz: Hertz
INL: Inner nuclear layer
IPL: Inner plexiform layer
IR: Infrared
ISOS: Inner Segment Outer Segment junction
kHz: kilohertz
L-, M-, and S-cones, respectively
LCA: Longitudinal chromatic aberration
mfERG: Multi-focal electroretinogram
mm: Millimeter
ms: Millisecond
NFL: Nerve fiber layer
nm: Nanometer
OCT: Optical coherence tomography
OPL: optical path length
PMT: Photomultiplier tube
PRL: Preferred retinal locus of fixation
RGC: Retinal Ganglion Cells
PSF: Point spread function
ROI: Region of interest
TSLO Tracking scanning laser ophthalmoscope
μm: microns

Acknowledgements

Firstly, I would like to thank the person who made this all possible, my graduate mentor, Austin Roorda. From the financial support to the mentorship and the opportunity to learn such an intricate system for my graduate work; I am thankful for the hands-on environment which taught me more than I ever thought I was capable of. I am sincerely grateful for every opportunity you have given me to develop as a scientist and as a person.

Appreciation is also due to the members of my committee, Professor Richard Kramer and Laura Waller, for their feedback and time take in review of these concepts over the years and their support.

Next, I want to thank all of the coauthors and the Roorda lab members and mentors who have taught me most of what I know today offered me intellectual support and personal friendship. Thank you to Fabio Feroldi, Ally Boehm, Francesco LaRocca, Volker Jaedicke, Swati Bhargava, Charolotte Wang, Ethan Bensinger, Kat Foote, Will Tuten, Ram Sabesan, John Eric Vanston, Nicolas Bensaid, Brian Schmidt, Natalie Stepien. And a special thanks to the glue that holds the Roorda lab together, Pavan Tiruveedhula you were always there to help us and saved us so many times; none of this would have worked without your support.

I also want to thank the friends I have made throughout these years who have supported me through early mornings and long days with never ending strada runs. All of my vision science classmates have inspired me on the daily basis with their love for science and amazing work they do, thank you to everyone at Berkeley who I was lucky enough to cross paths with! Special thank you to, Vasha Dutell, Angelica Godinez, Teresa Canas Bajo, Susan Hao, Kelly Byrne, Cecile Fortuny.

I especially want to thank my family who have made me into the person I am today. Most importantly thank you to my parents who taught me the values of education and inspired me on the daily basis, Taraneh Bahrami and Mohammad Mozaffari. To my sisters Saba Mozaffari and Sahar Mozaffari, you both make me better person every day. To my favorite people, Peymaneh Bahrami and Mahmood Mozaffari. And to my wonderful grandmother, Sedigeh Abdarbashi. To the not so little devils, Shawheen Ghezavat and Nima Ghezavat; of course, Maryam Mozaffari and Amir Ghezavat. Special thank you to Harikrishnan Kuppasamykrishnan and of course Meeka&Boo!

Chapter 1. Introduction

1.1. Introduction to Retina Physiology

The human retina is a complex structure which actively processes a spectrum of information from a basic photocurrent to complex visual scenes encoding temporal, spectral, and spatial information. The retina has many layers embedded with different neural circuits each of which have an independent processing methods. This dissertation will focus on the initial input of the retina, the photoreceptors; in particular, imaging the structural and functional properties of these photosensitive cells.

1.1.1. Anatomy of the Retinal Layers

The retinal layers are depicted in Figure 1.1; starting from superficial layers which encounter light first: the inner limiting membrane, nerve fiber layer, ganglion cell layer, inner plexiform layer, inner nuclear layer, outer plexiform layer, outer nuclear layer, external limiting membrane, inner segment outer segment layers, and the retinal pigment epithelium layer.

The inner limiting membrane is a membrane superficial to the nerve's fibers on which Müller cell end feet reside. The ganglion cell layer comprises the cell bodies which are most superficial whose axons consist of the nerve fiber layers which bundle to form the optic nerve. These neurons are the only neurons which fire action potentials, although their main input is a neurotransmitter release, a graded potential in the inner plexiform layer from the amacrine cells and bipolar cells. The inner nuclear layer consists of the cell bodies of the amacrine cells, bipolar cells and the horizontal cells which have their synapses in the outer plexiform layer feeding from the photosensitive rod and cone projections. The outer nuclear layer consists of photoreceptor the cell bodies of the photosensitive cells which are contained within the external limiting membrane which refers to the interface of the cell body and the inner segment. The inner segment outer segment (ISOS) junction refers to the reflection band separating the photoreceptor inner segment and outer segment, from which point the cell body interfaces with the outer segment which consists of the flattened membrane discs embedded with photopigments integral to the phototransduction cascade. The last layers of disks reflect light back referred to the cone outer segment tips (COST) The last layer is the retinal pigment epithelium which provides the photosensitive cells with nutrition and supports their function.

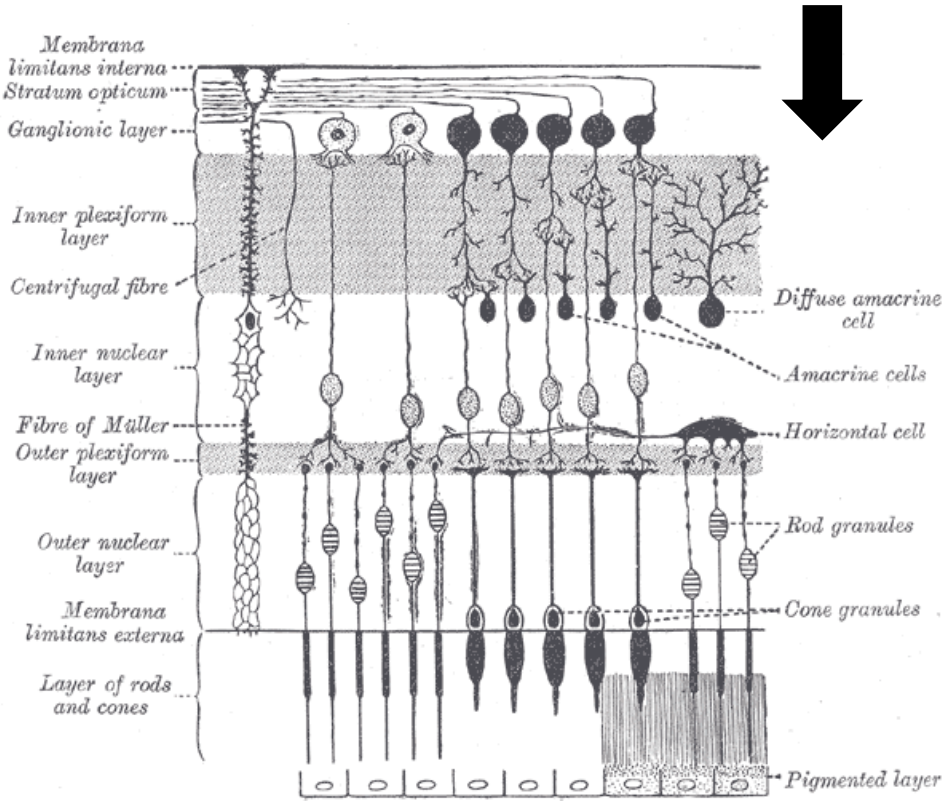

Figure 1.1: This diagram shows the main neuron types in the retina and the arrow in the top right indicates the incoming light beam. Here we can appreciate the three distinct layers of cell bodies in the retina.(Gardner & Osburn, 1978)

There are two main types of photosensitive cells in the eye, the color sensitive cone photoreceptors and the low light sensitive rods photoreceptors. Cone cells have been classified into three sub-types, the long wavelength cones (L-cones, 558 nm), medium wavelength cones (M-cones, 531 nm) and the short wavelength cones (S-cones, 419 nm). The rods are structurally distinct with longer outer segments and all have the same sensitivities with a peak at 496 nm. These structural differences can be appreciated in Figure 1.2. The photoreceptors in the retina contain large amounts of a tightly packed membrane which is embedded with the photopigments that absorb light. All the photopigments embedded in the disk membranes have a protein base called opsin, which is attached to a chromophore. As retinal absorbs the photon a molecule changes configuration from 11-cis to all-trans, triggering a signal transduction cascade.

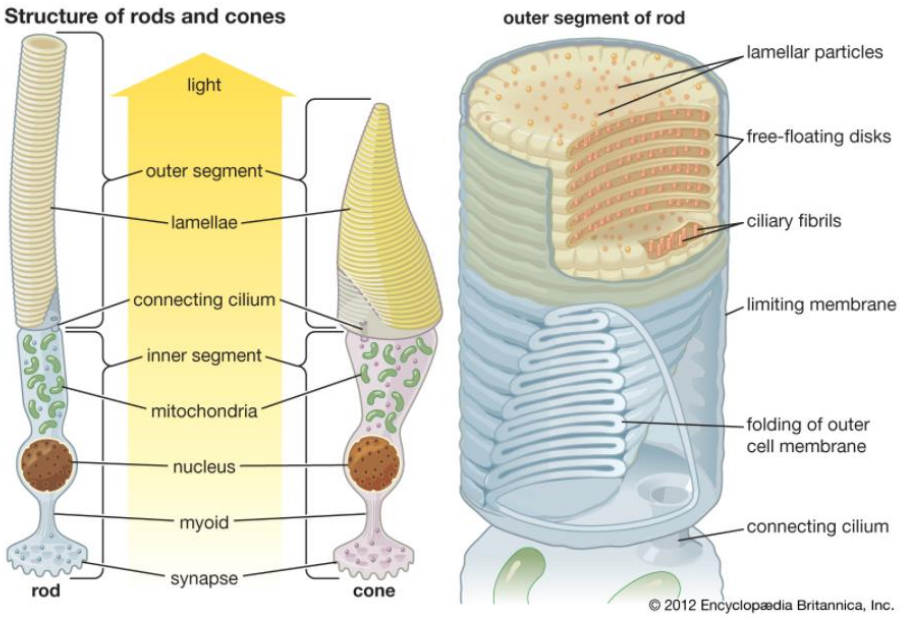

Figure 1.2: Photoreceptor cells have similar structure with the tightly packed disks in the outer segment. Here we can appreciate the difference in the rod to cone structure with respect to the inner segment diameter and outer segment length.(*Encyclopaedia Britannica*, 2012)

1.1.2 Introduction to Optophysiology

Optophysiology has been recently established as a label-free optical probe for recording the membrane potential from cells ex vivo physiology (Cordeiro et al., 2017; Ling et al., 2019) and more recently in the human retina in vivo(Boyle et al., 2020; Pandiyan et al., 2020). Previous studies have shown that neural axons experience a displacement in volume which accompanies action potentials, resulting in changes of the light scattering (Bryant & Tobias, 1952; Cohen et al., 1968; Hill, 1950; Salzberg et al., 1985) to be known as an intrinsic optical signal (Fields, 2011; Fields et al., 2009; Sasaki et al., 2002). The volume displacement has been studied in the squid retina and amphibian retina (Matsumoto et al., 1983; Tasaki & Byrne, 1987), olfactory bulbs (Tasaki et al., 1989; Tasaki & Byrne, 1988), dorsal root ganglia (Matsumoto et al., 1983), frog spinal cord (Tasaki & Byrne, 1984), invertebrate axon (Bryant & Tobias, 1955; Hill, 1950), giant squid axon (Akkin et al., 2009; Iwasa et al., 1980; Terakawa, 1983), and the mammalian neurohypophysis (Kim et al., 2007; Salzberg et al., 1985). The optical measure of action potentials has a synced time course with the membrane potential such that the amplitude of light scattering is proportional to the membrane potential squared (Kim et al., 2007). These measures of intrinsic optical signals are alterations in light scattering and optical retardation which stem from changes in the shape of the cell and the local changes in the index of refraction (Oh et al., 2012).

The origin of the shape changes in the cell that could affect light scattering would be the hydrostatic pressure, membrane tension and the stress exerted by the cytoskeleton. The mechanisms behind the intrinsic scattering changes are due to electrical-to-optical coupling of the plasma membrane. As shown in Figure 1.3, these coupling effects include: volume changes associated with the water transport carrying the ionic current (Kim et al., 2007); the electrostriction effects in which the plasma membrane dipole structure align causing alterations

in the membrane birefringence (Cohen & Keynes, 1971; Stepnoski et al., 1991); and electromotility which is the direct coupling effect between the membrane tension and membrane potential(Oh et al., 2012).

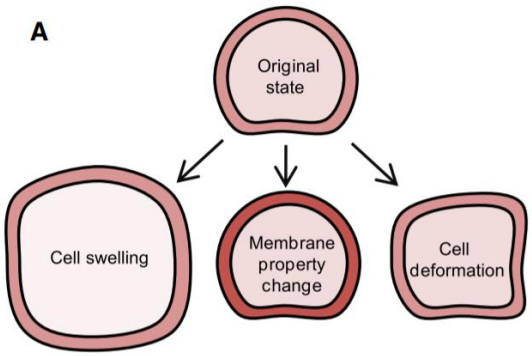

Figure 1.3: Here is a summary of the different attributions to a mechanical change in the neuron. Although there are three mechanisms at play, the resultant optical path length between these responses is similar (Oh et al., 2012).

The majority of biophysical modeling of action potentials including the classical Hodgkin-Huxley model(Hodgkin et al., 1952) has two main assumptions, the cells have a constant electric field which is independent of ion movements, and that there are no mechanical changes in the cells. Two parallel theories which both agree with the Hodgkin-Huxley model, but take into consideration both the electric field and mechanical changes are the soliton model depicted by Heimburg (Heimburg & Jackson, 2005) and the action waves model described by El Hady (El Hady & Machta, 2015).

The soliton model considers the action potentials to be a wave packet which have dispersive effects in media. The hydrodynamics of the ions during action potentials result in thermodynamic reactions. The Hodgkin-Huxley interpretation is that as a membrane capacitance is discharged, the initial sodium current releases heat; and as the potassium moves along the concentration gradients, heat is absorbed while the membrane capacitance recharges.

The action wave refers to a mechanical surface wave which is devised of compressive electrostatic force across the membrane. The action wave model predicts the change in mechanical, electrostatic heat and voltage based on a displacement field which is dependent on the energy stored within each structure of the cell. Potential energy is stored within the elastic membrane and the cytoskeleton of the cell while the kinetic energy is in the axoplasmic and extracellular fluid.

Recent work has shown the characteristics of this mechanical deformation with respect to temporal, spatial and amplitude factors align best with the voltage dependence of membrane tension model. Both the magnitude and frequency response correspond with the tensioned membrane in which these signal arise from the lateral repulsion of the ions at the neuron's bilayer membrane during action potentials(Ling et al., 2020).

1.1.3 Optoretinogram – Optophysiology of the human retina

As photoreceptors respond to light both electrical and biomechanical changes are taking place with the onset of the phototransduction cascade. The electrical signals have been closely

studied with patch clamp recordings and well characterized in vivo with functional electroretinograms. Over the years, different methods have been used to shed light on the biomechanical changes observed in the photoreceptors based on scattering changes (Abramoff et al., 2006; Bizheva et al., 2006; Grieve et al., 2006; Schallek et al., 2009; Ts'o et al., 2009) and fluctuations in the reflectance profile from interference based methods (Cooper et al., 2020; Jonnal et al., 2007; Litts et al., 2017; Miller et al., 2003; Zhang et al., 2005). As technology allowed, the new subfield of phase resolved interference methods have been recently established to quantify the changes in the outer segments with regards to photoreceptor disc shedding with respect to light (Azimipour, Migacz, et al., 2019; Boyle et al., 2020; Hillmann et al., 2016; Jonnal et al., 2012, 2016; Kocaoglu et al., 2014; Kurokawa et al., 2020; Liu et al., 2019; Migacz et al., 2019; Pandiyan, et al., 2020).

The initial concept of optically measuring the function of the retina was introduced by Mulligan in 1994 (Mulligan, 2019; Mulligan & Macleod, 1994). The optoretinogram has been well characterized since to have an early response (Boyle et al., 2020; Pandiyan et al., 2020) and a later response to a flash of light (Azimipour, Migacz, et al., 2019; Drexler, 2001; Kocaoglu et al., 2014, 2016; Liu et al., 2019; Miller et al., 2011; Zhang et al., 2019). The functional response of the photoreceptor was indicative of the photoreceptor type(Pandiyan et al., 2020; Zhang et al., 2019) and was further characterized for a potential diagnostic measures as the responses scaled with the flash intensity with an early response ranging from 5 to 57 nm and the late response ranging from 50 to 600 nm outer segment path length change.

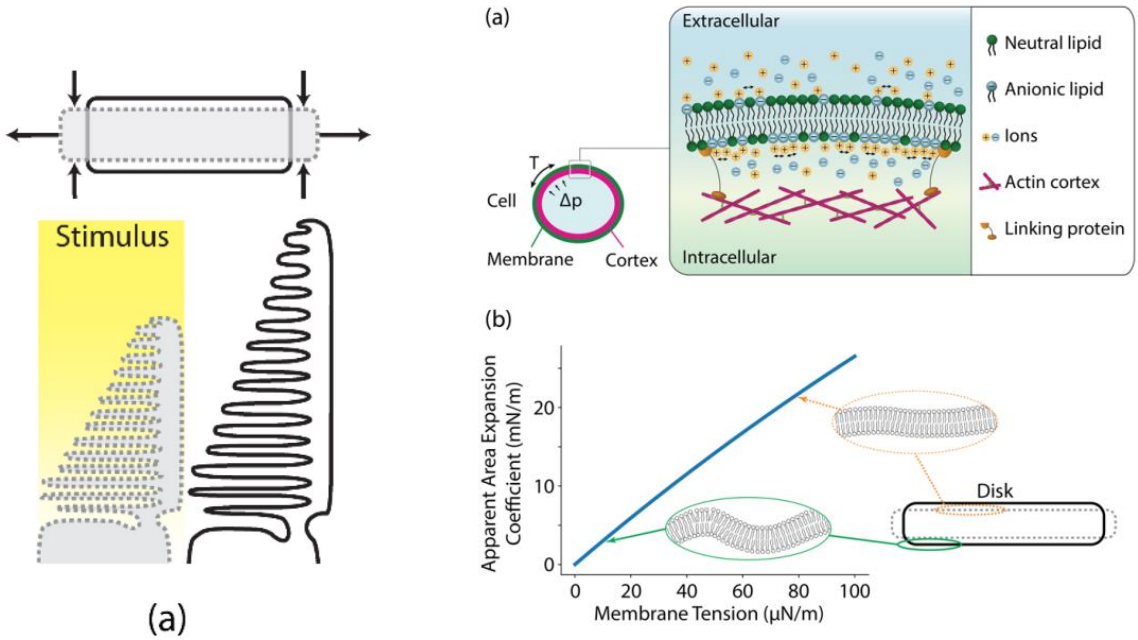

Figure 1.4: Shown above is the structural changes in the optoretinogram as the photoreceptor membrane stiffens the outer segment physically contracts.(Pandiyan, et al., 2020)

The early response peaks earlier with stronger stimuli directly correlated to the early receptor potential measure in patch clamp recording (Brown & Murakami, 1964; Hestrin & Korenbrot, 1990; Hodgkin & Obryan, 1977). As studied in more detail, the fast

hyperpolarization of the disk membrane increases the repulsive forces causing the disk to expand with a fixed volume, which flattens the disk and is recorded as a decrease in optical path length as the outer segment seemingly contracts as shown in Figure 1.4 (Boyle et al., 2020; Ling et al., 2019; Pandiyan et al., 2020).

The late response corresponds to a slow increase in the optical path length corresponding to the osmotic swelling caused by the ionic flux. This ionic flux is dependent of the class of photoreceptors with different response based on the amplitude of the functional response. The late response has been characterized to be due to the diffusion of water during the osmotic imbalance from the flood of ions during the phototransduction cascade. When testing for this mechanism using different knockout mice in rods, the transducin knockout did not show this osmotic swelling determining transducin must be one of the main contributors to the osmotic imbalance(Zhang et al., 2017).

In this thesis, a phase-sensitive low coherence optical system was developed to record the change in optical path length within the different retinal layers with potential to determine the functional biomarker in response to a stimulus as a future diagnostic to measure photoreceptor health.

1.2 Retinal Imaging

1.2.1 Scanning Laser Ophthalmoscopy

The simplest form of microscopy began with a camera which collected incident light from a sample onto a photosensitive material. Over time the field of microscopy advanced to develop larger field of views, faster acquisition, and resolution improvement. The largest development in this field was to manipulate the light illuminating the sample to replicate a focused spot to collect the light incident from a particular spot instead a full flash of light avoiding multiply scattered stray light. With this modality, the light collected consecutively in time resolves each point individually for a higher contrast image.

The next fundamental concept within the field of microscopy was confocal imaging; by using a pinhole in front of the detector only the incident light can be collected, filtering in depth with respect to the plane interest. Confocal imaging allows for sectioning in depth to increase the signal to noise ratio for the plane of interest rejecting light reflected from the other structures. A schematic of a confocal imaging system is shown below in Figure 1.5, specifically referring to the red beams which show that only light pertaining to the depth of interest is collected in the confocal pinhole in the detection.

The concepts originating from microscopy were adapted to ophthalmoscopy initially via fundus photography in which an image is taken with a full field flash of the back of the eye. This method relies on using the eye's lens to focus the light for collecting this light reflected from the fundus flash. The next method adapted to ophthalmoscopy is the scanning laser microscope which was adapted to design the scanning laser ophthalmoscope(Webb & Hughes, 1981) (SLO) consisting of a scanning beam utilizing the eye's lens as a microscope objective to image the point source onto the retina. The scanning laser ophthalmoscope additionally incorporates confocality(Webb et al., 2011) with pinholes before the detectors to section through the retinal layers enabling different structures to be visualized in high resolution.

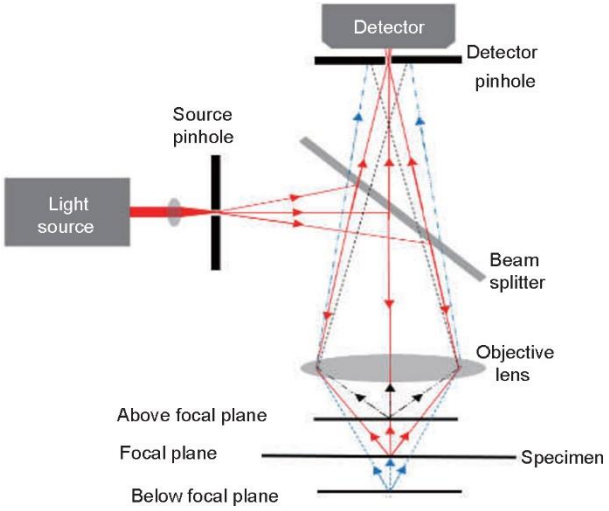

Figure 1.5: Here the different components of a confocal microscope depicted above. The main attribute to note is that only light reflected from plane of interest is allowed through the confocal pinhole and the light from other areas are rejected by the detector pinhole.(Wang et al., 2015)

Microscopy has been further developed to simultaneously maximize light collection and improve resolution. Evidently these are inversely correlated since majority of the light collected is rejected to optimize for the resolution via confocality, which shows a maximum resolution increase with a smaller pinhole. In order to take full advantage of the resolution improvement of the ideal confocal pinhole, the signal is significantly reduced which is detrimental for retinal imaging since it is already light starved. Pixel reassignment is a microscopy method in which the refocused light from the illuminated spot on the retina is sampled with a detector array such that the point spread function is subsampled distinctly and the multiply scattered light is reassigned with a subpixel shift to make a more efficient use of the signal while preserving high resolution(DuBose et al., 2019; Guizar-Sicairos et al., 2008; Roider et al., 2016; Roth et al., 2013).

Outside of the Airy disc diameter is low signal from the multiply scattered light reflecting light from different layers. One method used to collect additional light is to measure the offset aperture or multiple scattered light imaging in which the non-confocal light is efficiently collected and computationally redistributed accordingly(Chui et al., 2012; Guevara-Torres et al., 2015, 2016; Sapoznik et al., 2018; Scoles et al., 2013, 2014). This method is a type of phase contrast imaging revealing structures based on the index of refraction changes.

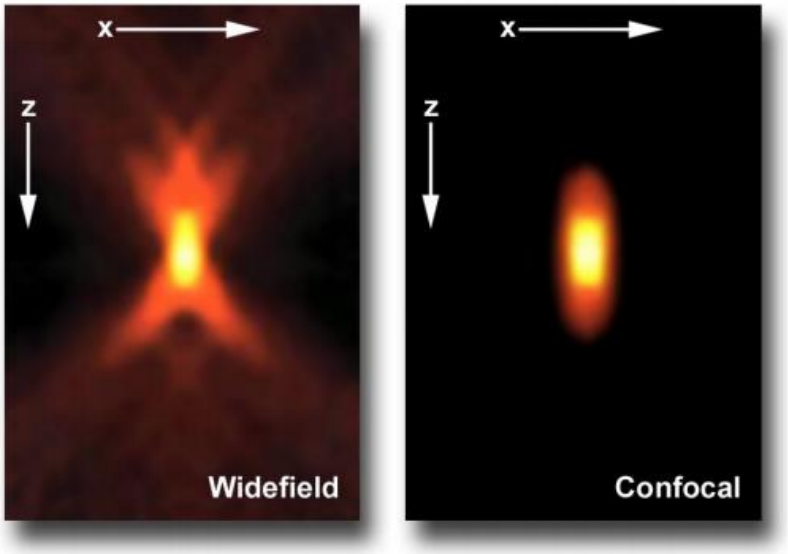

Figure 1.6: This image shows the point spread function collected in a normal scanning laser system compared to a confocal scanning laser system. The confocal pinhole rejects the signal outside the air disc diameter, collecting only the high fidelity portion of the point spread function. (Claxton et al., 2011)

Overall, SLO is a high-resolution retinal imaging tool that measures the structural topography in a confocal or multiply scattered light profile. The AOSLO system has been further developed in the Roorda Lab to track the retina and deliver stimuli particular cones to probe the neural circuitry of color vision(Harmening et al., 2012, 2014; Roorda et al., 2002; Sheehy et al., 2015; Stevenson et al., 2010). An imaging system can deliver a bright flash of light and measures the bleaching response of the cones based on their reflectance profile, a method known as densitometry; by measuring the bleaching curves to a series of different stimuli the cone class types can be deciphered based on the cone photoreceptor response(Roorda & Williams, 1999; Sabesan et al., 2015).

1.2.2 Optical Coherence Tomography

Optical coherence tomography (OCT) is a non-invasive imaging method which uses low-coherence light interferometry to measure the depth information of a sample (Drexler & Fujimoto, 2006; Srinivasan et al., 2006). Light backscattered from the sample arm interfering with the reference arm carries information that can be used to reconstruct the depth profile of the sample.

OCT has been developed over the years, starting from the original time domain OCT in which a reference arm is adjusted in length over time to acquire the depth information(Chinn & Swanson, 1997; Drexler & Fujimoto, 2006; Huang et al., 1991; Swanson, 1992). The common design implemented was the Michelson interferometer shown on the left of Figure 1.7 with a beam splitter reflecting part of the beam, creating two beam paths which are redirected to interfere at the beamsplitter, and the detector that records the resultant signal consecutively as the reference arm is moved in depth.

The next major development in this field was Fourier domain OCT which directly samples the spectral information to obtain an interferogram. As depicted on the right of Figure

1.7 there are two types of Fourier Domain OCT: spectral domain OCT which uses a broadband of light for imaging and separates the spectrum in the detector with a spectrometer(Choma et al., 2005; de Boer et al., 2003; Leitgeb et al., 2003; M. Wojtkowski et al., 2002; Maciej Wojtkowski et al., 2002, 2004), while swept source OCT optically sweeps through the wavenumber within the source and temporally deciphers the spectral information(Braaf et al., 2011; Choma et al., 2003). The main advantage of Fourier domain OCT systems is that their sensitivity is improved in the order of 100-1000 compared to time domain OCT, allowing correspondingly faster imaging.

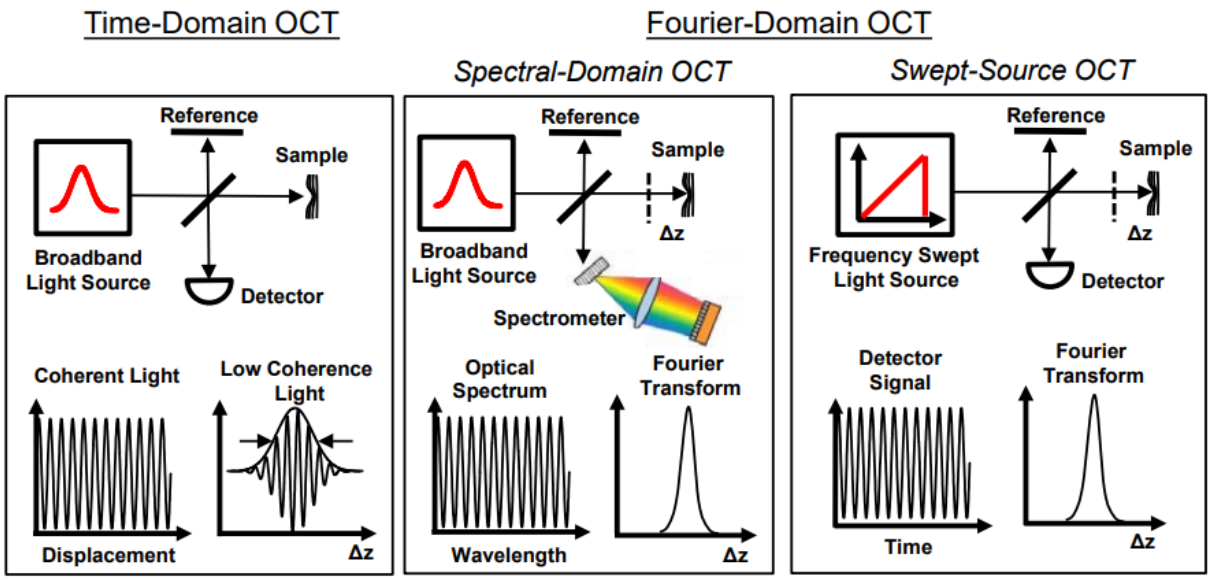

Figure 1.7: These schematics show the different types of OCT from the basic time-domain OCT which physically moves the reference, to the further developed Fourier-Domain OCT which spectrally samples depth. (Swanson & Fujimoto, 2017)

All these systems have their own advantages and disadvantages, the system described in this work utilizes a swept source OCT chosen for the 1050 nm wavelength which is just above the visible range for the retina. This OCT system consists of a swept source laser source centered at wavelength 1040 nm with a bandwidth of 90 nm and a sweep rate of 100 kHz. The axial resolution of the OCT path is measured to be 9.7 micrometers in air, 6.5 micrometers in tissue.

Equation 1 shows the equation for the spectral interferogram collected at the detector as function of the wavenumber $\widehat{D}_i[k_m]$is dependent on the source intensity profile as a function of the wavenumber $\hat{S}[k_m]$ and the reflected light at the reference and the sample R_R and R_S. Within the interference term one can see the depth information, z, as a function of wavenumber, k. To extrapolate the depth information, one can take the Fourier transform of Equation [1] to generate Equation 2. The first term refers to the DC component of the non-interfering term from the reference and sample arm. The last two terms refer to the depth location of the scatterer and the complex conjugate term.

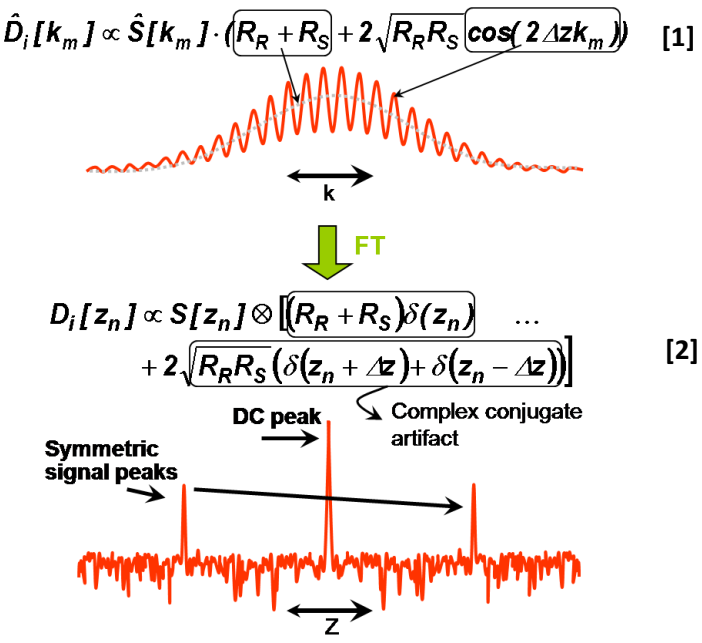

Figure 1.8: Equation 1 expresses the interferogram as a function of wavenumber for a Fourier Domain OCT. Equation 2 calculates the Fourier transform of Equation 1 to determine the depth location of the sample. The first plot shows the spectral interferogram with the underlying amplitude from the DC term and the overlying frequencies encoding the sample depth information. The second plot shows the Fourier transform of the interferogram creating a DC peak at 0 and the signal peaks in the depth direction. ((BORG), 2011)

A Fourier transform of the collected interferogram relays the relative depth information within the sample. The frequency of the interference fringes determines the depth of the sample and the amplitude of the fringes determines the signal strength. A broader bandwidth of the spectrum will produce interference patterns of a shorter temporal and spatial extent resulting in a higher resolution. The OCT source wavelength and bandwidth control the eye penetrability, visual sensitivity, and the OCT axial resolution. In regard to penetrability, the lower wavelengths have low penetration depth due to light scattering and higher wavelengths become problematic with absorption. Because of visual sensitivity, lower wavelengths are limited in power and the higher infrared wavelengths allow for higher power exposures. The lower wavelengths are optimal for improved resolution both axially and laterally.

Lateral resolution is determined by the diffraction limited beam size which is proportional to wavelength and inversely proportional to the numerical aperture. Axial resolution of the OCT is given by the coherence length of the source which is the center wavelength squared and divided by the spectral bandwidth [$\lambda 2/ \Delta\lambda$]. The spectrum of the source has a particular autocorrelation function which describes the relative correlation between the wavelengths within the coherence length, the autocorrelation function and the coherence length are inversely related, both determining the coherence gate for interference. The OCT measures the interference of a spectrum with respect to the sample and a known reference arm, so a broader bandwidth spectrum allows for larger range of frequencies to interfere, in turn increasing the sensitivity to OPL changes. Overall depth range is determined by the sampling of the spectrum. Since swept source has developed advancements in controlling the source sweep with instantaneous linewidth; this technology pushes the envelope in imaging depth range.

In order to utilize the OCT for phase imaging, the phase of each wavelength sweep needs to be known to account for the change in phase within the interferogram. The swept source OCT has a Mach Zhender interferometer embedded within the source to align the exact wavenumber sampling by optically measuring the small variations in k sweeps to sync the k-space of each A-scan(Braaf et al., 2011).

1.2.3 Adaptive Optics

Adaptive optics is a resolution improvement technique which was developed in astronomy; it was originally intended to image the stars through the atmosphere by measuring the aberrations in the atmosphere and correcting for the turbulence with an adaptive optic such as a deformable mirror. Astronomers began by dedicating a bright guide star as a beacon to measure the aberrations in the atmosphere. Since the guide star is assumed to be a point source in the atmosphere, the aberrations measured correspond to the atmospheric turbulence. A wavefront sensor can be used to then measure the aberrations and correct for them by using an adaptive optic to apply the phase correction. When the adaptive optics correction is active, the guide star's blur would approach a diffraction-limited spot and the imaging signal increases as aberrations are corrected. When the adaptive optics correction is applied, the blurry planets would become sharp images as the aberrations within the atmosphere are corrected the optical quality of the beam is enhanced to provide better lateral resolution. The wavefront of the atmospheric turbulence is measured with a wavefront sensor and the deformable mirror is driven to collect a flat wavefront for optimal beam quality as shown in Figure 1.9.

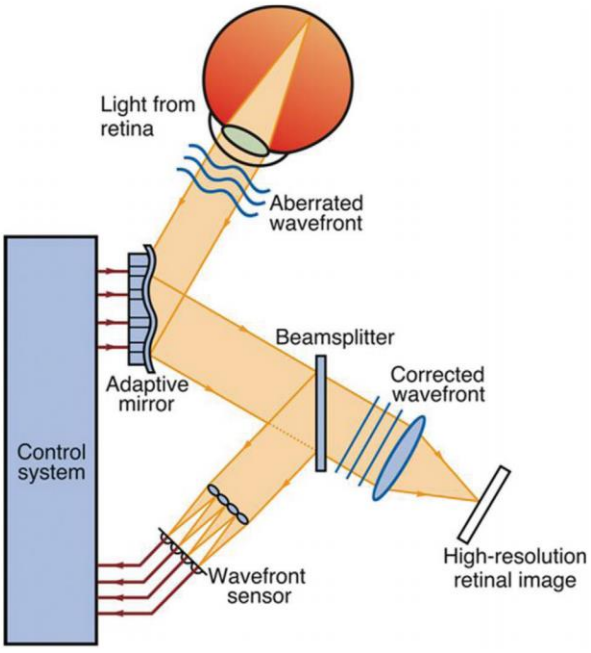

Figure 1.9: This schematic shows the main components of an adaptive optics closed loop correction. The aberrated light from the retina is measured by the wavefront sensor and correction by the adaptive mirror to relay a corrected wavefront to obtain a high resolution retinal image. (Max, 2014)

Adaptive optics was first applied to retinal imaging via fundus photography (Liang et al., 1997; Roorda & Williams, 1999) and later applied to SLO(Roorda et al., 2002). The common wavefront sensing technique for retinal imaging is the Shack-Hartmann wavefront sensor

implemented to measure the ocular aberrations. The Shack-Hartmann wavefront sensor consists of a lenslet array which is focused on a onto a camera; the wavefront sensor images the pupil measures the centroid of the beam focused from each lenslet. Each lateral dislocation in X and Y of the lenslet centroid measurements relays the local slope of the light attributing to the overall wavefront measurement. The wavefront is then quantified by fitting it with the Zernike polynomials to obtain the aberration estimation via Zernike coefficients.

The adaptive optics correction is implemented with the deformable optics mirror which can be shaped to account for the ocular aberrations to image a point source onto the eye and collect high resolution images. The adaptive optical component used in the AOSLO and AOOCT system was an ALPAO 97 actuator deformable mirror with magnetic membrane technology providing a smooth wavefront correction. When the adaptive optics correction is applied, the signal increases in both intensity and resolution as a finer point of focused energy is imaged and the collected is significantly increased. We can further appreciate the adaptive optics correction later in Chapter 3 as the AOOCT shifts focus through the retina.

Chapter 2. Wide-vergence, multi-spectral adaptive optics scanning laser ophthalmoscope with diffraction-limited illumination and collection

2.1 Abstract

Visualizing and assessing the function of microscopic retinal structures in the human eye is a challenging task that has been greatly facilitated by ophthalmic adaptive optics (AO). Yet, as AO imaging systems advance in functionality by employing multiple spectral channels and larger vergence ranges, achieving optimal resolution and signal-to-noise ratios (SNR) becomes difficult and is often compromised. While current-generation AO retinal imaging systems have demonstrated excellent, near diffraction-limited imaging performance over wide vergence and spectral ranges, a full theoretical and experimental analysis of an AOSLO that includes both the light delivery and collection optics has not been done, and neither has the effects of extending wavefront correction from one wavelength to imaging performance in different spectral channels. Here, we report a methodology and system design for simultaneously achieving diffraction-limited performance in both the illumination and collection paths for a wide-vergence, multi-spectral AO scanning laser ophthalmoscope (SLO) over a 1.2 diopter vergence range while correcting the wavefront in a separate wavelength. To validate the design, an AOSLO was constructed to have three imaging channels spanning different wavelength ranges (543 ±11 nm, 680±11 nm, and 840±6 nm, respectively) and one near-infrared wavefront sensing channel (940 ±5 nm). The AOSLO optics and their alignment were determined via simulations in optical and optomechanical design software and then experimentally verified by measuring the AOSLO's illumination and collection point spread functions (PSF) for each channel using a phase retrieval technique. The collection efficiency was then measured for each channel as a function of confocal pinhole size when imaging a model eye achieving near-theoretical performance. Imaging results from healthy human adult volunteers demonstrate the system's ability to resolve the foveal cone mosaic in all three imaging channels despite a wide spectral separation between the wavefront sensing and imaging channels.

2.2 Introduction

The adaptive optics scanning laser ophthalmoscope (AOSLO) is an important imaging tool that can achieve in vivo, near diffraction-limited visualizations of microscopic structures in the retina by compensating for the monochromatic aberrations of the eye(Liang et al., 1997; Roorda et al., 2002). Increasingly, adaptive optics systems are employing multiple wavelength channels for a range of imaging and vision testing applications(Carroll, 2008; Merino & Loza-Alvarez, 2016; Roorda et al., 2002). Most systems use different wavelengths for wavefront sensing and imaging(Dubra & Sulai, 2011; Li et al., 2011; Merino & Loza-Alvarez, 2016). Systems for AOSLO microperimetry and visual psychophysics employ NIR wavelengths for wavefront sensing and tracking and deliver AO- corrected flashes of visible light(Tuten et al., 2012, 2019). Other multi-wavelength applications include fluorescence(Morgan et al., 2009; Schallek et al., 2013; Tam et al., 2016), retinal oximetry(Li et al., 2011), multi-modal imaging(Liu et al., 2018) and possibly hyperspectral imaging(Dubra & Sulai, 2011). There are two important factors to consider when designing, building, and interpreting results from a high-fidelity multi-wavelength AOSLO system: the chromatic aberrations of the eye and the chromatic aberrations of the system. Chromatic effects of the eye: First and foremost, the chromatic dispersion of the eye needs to be considered(Marcos et al., 1999; Smirnov, 1961). The chromatic difference in defocus of the eye (longitudinal chromatic aberration, or LCA) has been extensively studied by many

groups each with large subject pools(Atchison & Smith, 2005), and its behavior is quite predictable and similar between individuals, albeit with inter-individual differences depending on the eye's specific optical parameters(Bedford & Wyszecki, 1957; Ogboso & Bedell, 1987; Simonet & Campbell, 1990) (e.g. corneal curvature). Since the LCA of the human retina is quite similar in the population, a single achromatizing lens(Lewis et al., 1982; Powell, 1981) can be designed to compensate LCA for retinal imaging(Fernández et al., 2008; LaRocca et al., 2014; Qiu et al., 2020; Zawadzki et al., 2008). Techniques for custom adjustment of LCA in an AOSLO can also be used(Jiang et al., 2019). However, this additional optic adds complexity by requiring the addition of another pupil-conjugate plane and, depending on how it is placed, can give rise to deleterious back-reflections. The transverse chromatic aberration, or TCA, of the eye has also been studied(Jiang et al., 2019; Thibos et al., 1990) and recently objective techniques to measure it(Harmening et al., 2012; Winter et al., 2016) and correct it(Boehm et al., 2018; Fernández et al., 2006; Harmening et al., 2012) have been employed. The extent to which the high order aberrations of the eye change with wavelength is less studied(Fernández et al., 2005; Llorente et al., 2003; López-Gil & Artal, 1997). As a rule, there must be differences in high-order aberrations as the ray paths that different wavelengths of light take through the optical system to reach a focus on the retina are different. But, researchers generally agree that these differences are small and often fall within the range of measurement error of the system(Llorente et al., 2003; Manzanera et al., 2008; Vinas et al., 2015). In the current study, our aim was to carefully explore the implications of using NIR wavelengths for wavefront sensing and visible light for imaging. In a diffraction-limited system, the size of the point spread function is proportional to wavelength, so the best possible outcome is that the changes in high-order aberrations between wavelengths are negligible, and the benefits of reduced diffraction would yield increasingly sharp images at progressively shorter wavelengths even if wavefront sensing was performed at long (NIR) wavelengths. In the worst possible outcome, the high order aberrations would change enough to offset the benefits of reduced diffraction when imaging at wavelengths shorter than the wavefront sensing wavelength. Chromatic effects of the AOSLO system: To facilitate an exploration of the implications of high-order changes in chromatic aberrations in the eye for multi-wavelength AOSLO systems, it is paramount to minimize or fully characterize the chromatic effects of the AOSLO itself. The bulk of this manuscript describes this effort. Current-generation AOSLOs are typically able to achieve high resolution while driving the deformable mirror over wide vergence ranges (~3 diopters). Optimal performance has been achieved by designing the relay telescopes in the AOSLO with either a non-planar design using off-axis spherical mirrors(Dubra et al., 2009; Dubra & Sulai, 2011), a planar design using a combination of off-axis toroidal and spherical mirrors(Liu et al., 2013), or an on-axis, lens-based design using polarized light and polarization gating to minimize back-reflections from refractive surfaces(Felberer et al., 2012).

However, to our knowledge, a similar consideration of vergence effects in the collection path of an AOSLO has not yet been described, despite the use of off-axis optical elements such as plate/wedge beamsplitters and dichroic mirrors in the collection path, which induce vergence-dependent aberrations. In order to quantify how close the optical quality of the AOSLO was compared to theoretical design, the measurements required the dismantling of the of the AOSLO system iteratively and required a series of images to perform the phase reconstruction needed to quantify the point spread function most accurately. Here, we present a multi-spectral AOSLO design with diffraction-limited performance in both the illumination and collection paths with vergence offsets ranging to 1.2 diopters between spectral channels. The optical design utilized all

acommercially available off-the-shelf optics thereby improving the cost-efficiency of our system compared to prior AOSLOs using custom-sized spherical mirrors(Dubra & Sulai, 2011) or custom toroidal mirrors(Liu et al., 2013). To facilitate the optical alignment and construction of this AOSLO design, we developed a detailed optomechanical model and constructed a laser-cut polycarbonate stencil, which indicated the placement of all optomechanics onto an optical table. After the AOSLO was constructed and aligned, we experimentally validated the system's resolution and collection efficiency using a phase retrieval technique and a model eye setup. Finally, we present imaging results at the fovea in two healthy adult volunteers and quantitatively compare resolution across imaging channels using a Fourier analysis. While wavefront sensing at 940 nm, the benefits of reduced spot size extends to images taken in shorter wavelengths based on the diffraction-limited point spread function in the eye. In the two subjects that were imaged using optimal confocal pinholes(Webb & Hughes, 1981; Wilson & Carlini, 1987), the foveal cone mosaic was well resolved at all wavelengths (840, 680 and 543 nm). The benefits of reduced diffraction with shorter wavelengths was readily visible but images at 680 nm and 543 nm were similar in quality indicating that the effects of higher order aberrations of the eye may begin to play a small role for shorter wavelengths.

2.3 Methods

2.3.1 System overview and optical design

The schematic and optical design of the multi-spectral AOSLO system is shown in Fig. 2.1 with a specification of components in Table 2.1. Light from a supercontinuum light source was separated into three imaging channels spanning different wavelength ranges (543 ±11 nm, 680±11 nm, and 840±6 nm, respectively) and one near-infrared wavefront sensing channel (940 ±5 nm). All spectral channels were aligned to be collinear using pairs of mirrors for each color channel and 3 dichroic mirrors. A 10:90 (R:T) wedge plate beam splitter was placed after the dichroic mirrors to separate the illumination and collection paths and was followed by four sets of spherical mirror-based telescopes arranged in a non-planar off-axis manner that relayed an image of the system's entrance pupil onto the resonant scanner, galvanometer scanner, deformable mirror and, finally, the pupil of the eye. The positions and angles of all optics after the beam splitter in the illumination path (see Table 2.2) were optimized to minimize aberrations, mainly astigmatism, using optical design software (Zemax, LLC, Kirkland, WA) and the technique described by Dubra et al.(Dubra & Sulai, 2011). Diffraction-limited illumination spots were achieved for a 1° field of view (FOV) across all AOSLO spectral channels, as indicated by the spot diagrams and Strehl ratios at the bottom of Fig. 2.1.

To minimize aberrations in the collection path, we simulated a point source emitting from the retina and fixed all optical components in the illumination path while we ran an optimization for the collection optic's location and angles following the wedge plate beamsplitter in transmission (including the wedge plate beamsplitter itself). From our initial analysis, we determined that the wedge plate beamsplitter had the largest contribution to the collection path aberrations. To minimize aberrations induced by this beamsplitter, we optimized for the wedge angle and incident beam size (constrained by beam splitters that were commercially available as well as optomechanical limitations) to produce a minimum spot size across all spectral channels while correcting for the lower order aberrations including defocus and allowing a sufficient wedge angle to reject the ghost artifact from the back surface of the beamsplitter (see analysis in Figs. 2.2–2.4). Based on the simulation results, we chose to use a 0.5° wedge plate beamsplitter

(BSN10, 10:90 (R:T) UVFS Plate Beamsplitter, Thorlabs Inc, Newton, NJ) positioned along the optical path such that the incident illumination/collection beam size for all spectral channels was minimized given optomechanical constraints.

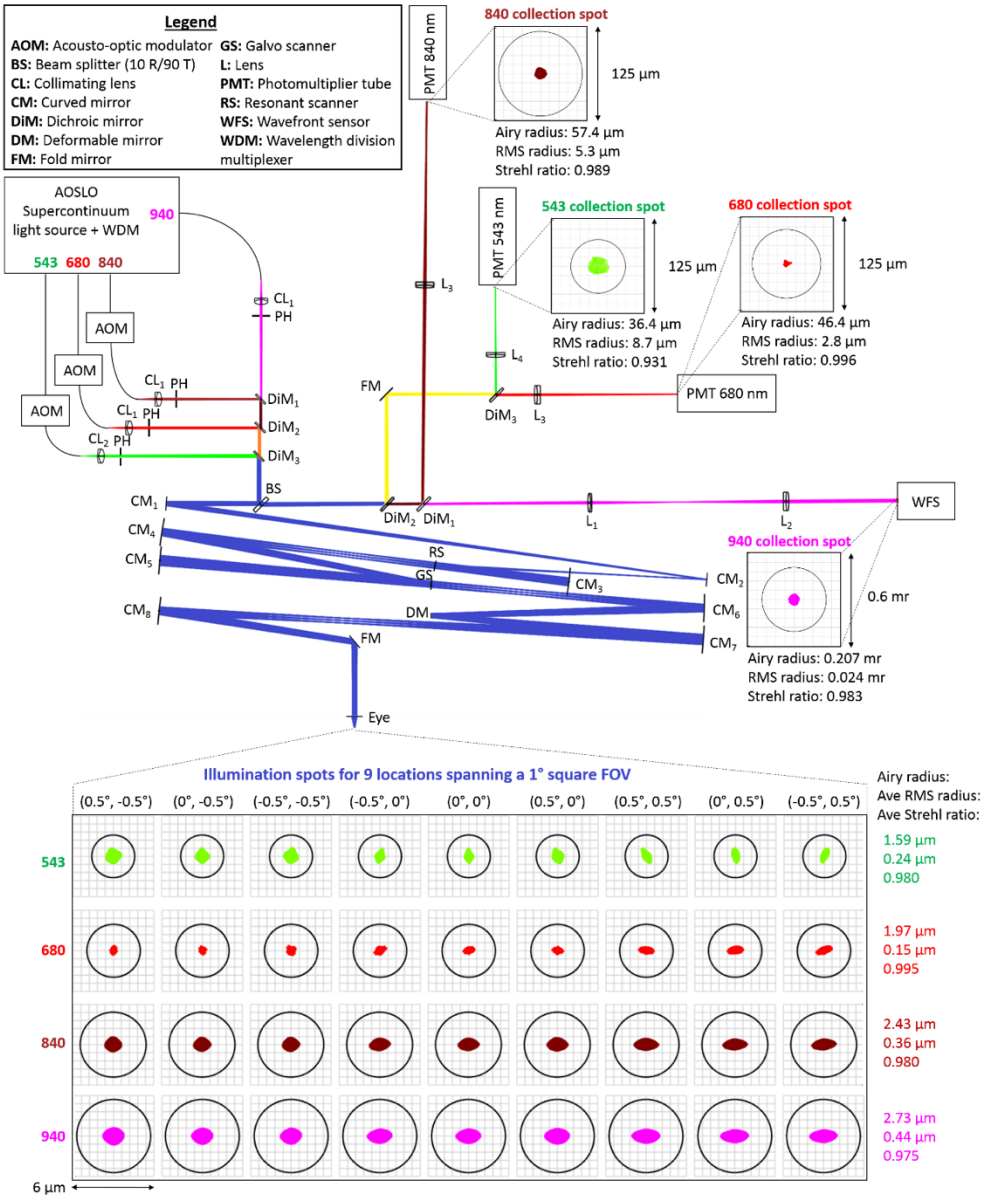

Fig. 2.1. Multi-spectral AOSLO optical design and schematic. All optical components are labeled and described in the legend. Green, red, maroon, and magenta paths correspond to the optical paths of the 543 nm, 680 nm, 840 nm, and 940 nm channels, respectively. Paths with combined channels are blue (all wavelengths), orange (680nm+840nm+940nm), brown (840nm+940nm), and yellow (543nm+680nm). Spot diagrams for all illumination spots spanning a 1° field of view (FOV) are shown below the schematic while those for specific collection channels are placed adjacent to the corresponding collection PMT or WFS as insets. Beneath each spot diagram are the Airy radius, root-mean-square (RMS) spot radius, and Strehl ratio. The model eye consists of a paraxial lens with a 16.7 mm focal length in air.

Table 2.1. System components and hardware

System components	Specifications	Part no./manufacturer
Light source	400-2400 nm supercontinuum laser	SuperK Extreme EXR-15 (NKT Photonics A/S, Birkerød, Denmark)
Spectral splitting unit	543±11, 680±11, 840±6, 940±5 nm	Custom
Horizontal scanner	15.785 kHz, Ø4.5 mm resonant scanner	SC30-4x5-6-16000 (Electro-Optical Products Corp, Glendale, NY)
Vertical scanner	Ø9.5 mm galvanometer scanner	6210H/6mm (Cambridge Technology Inc, Bedford, MA)
AOM	0-50 MHz, fiber-coupled	TEM210-50-10-543/680/840-2FP (Brimrose Corp, Sparks, MD)
Photodetector	1 ns rise time, high gain, GaAs(P) PMT	H7422-40/50 (Hamamatsu, Shizuoka-ken, Japan)
Photodetector amplifier	0-50 MHz, 25 mV/μA gain	C6438-01 (Hamamatsu, Shizuoka-ken, Japan)
SLO frame rate	30 Hz	-
SLO pixel dimensions	512 x 512 pixels	-
Acquisition software	ICANDI	Custom
WFS lenslet array	188 μm pitch, f = 8 mm, Ø25.4 mm	0188-8.0-S (Northrop Grumman AOA Xinetics Inc, Devens, MA)
WFS camera	45 fps, 1384 x 1032 pixel, 2/3" CCD	GS3-U3-15S5M-C (FLIR Systems Inc, Wilsonville, Oregon)
DM	1.5 ms rise time, 97 actuators, Ø7.2 mm	DM97-08 (ALPAO, Montbonnot, France)
AO closed-loop frequency	33 Hz	-
AO control software	AOSACA	Custom
Pupil diameter (eye)	7.2 mm	-
FOV (retina)	Up to 1° x 1° by design (max at 3° x 3°)	-

Table 2.2. Focal length, diameter, and angles of incidence on reflective optical elements of the AOSLO

Optical element	Focal length (mm)	Diameter (mm)	I_x (deg)	I_y (deg)
Spherical mirror # 1	500	25.4	4.00	-1.00
Spherical mirror # 2	500	25.4	2.50	0.00
Horizontal scanner	-	4.5	2.00	4.60
Spherical mirror # 3	250	50.8	0.00	3.30
Spherical mirror # 4	500	50.8	2.00	0.00
Vertical scanner	-	9.5	3.00	-3.30
Spherical mirror # 5	500	50.8	0.00	-3.30
Spherical mirror # 6	500	50.8	3.30	0.00
Deformable mirror	-	7.2	3.30	0.00
Spherical mirror # 7	500	50.8	1.00	2.50
Spherical mirror # 8	500	50.8	3.00	0.00

After minimizing the aberrations caused by the wedge plate beamsplitter, the resolution of the AOSLO's collection path was shown to be diffraction-limited (Strehl ratios > 0.8) for all imaging channels and for the WFS channel (see spot diagrams of collection path in Fig. 2.1). To further improve resolution via confocal gating(Webb & Hughes, 1981; Wilson & Carlini, 1987), approximately ~0.5 of the Airy disk diameter (ADD - which refers to the diameter of the first dark ring in the Airy diffraction pattern) pinholes were placed at retinal conjugates prior to the photomultiplier tubes (PMT) imaging channels. The 840 nm imaging channel was slightly more confocal with a pinhole equating to 0.44 ADD, while the 680 nm channel and the 543 nm channel were both collecting 0.54 ADD. For imaging channels with low SNR (e.g. the 543 nm imaging channel), a longer acquisition period was used to allow for robust image registration. To visualize the aberrations at the pupil planes in the system, and therefore at the WFS, we show footprint diagrams illustrating the real ray coordinates throughout the pupil for all scan configurations of the AOSLO (see Fig. 2.5). Due to the system aberrations a beam wobble manifests as shifts in the pupil for different scan positions. The simulation shows that the deviations in real ray coordinates for all scan positions at the eye and WFS in this AOSLO design (even in the worst case) lie well within the extent of a single lenslet indicating that the wavefront measurements are sampling-limited rather than aberration-limited.

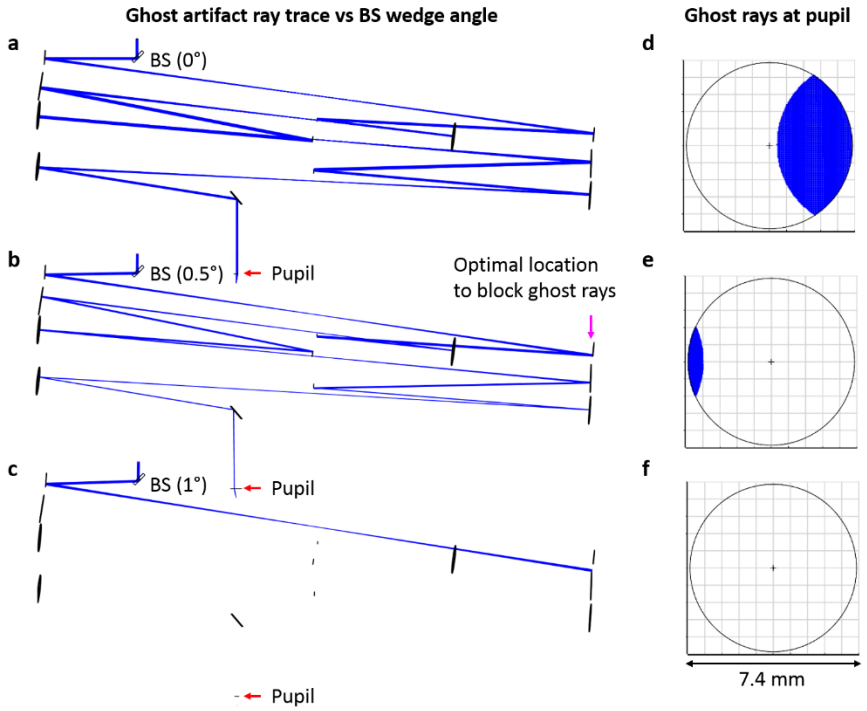

Fig. 2.2. Ghost reflection ray trace analysis for wedge plate beam splitters (BS) of different wedge angles. Ray traces for the light reflecting from the back surface of the wedge beam splitter are shown for wedge angles of 0°, 0.5°, and 1° for (a-c), respectively. The corresponding footprint diagrams for beam profiles at the pupil plane of a model eye are given in (d-f), demonstrating decreasing amounts of the ghost reflection with increases in wedge angle. The magenta arrow in b) indicates a location in the non-scanning portion of the AOSLO system for which an iris can be placed to completely block the ghost artifact without affecting the imaging optical path of the AOSLO.

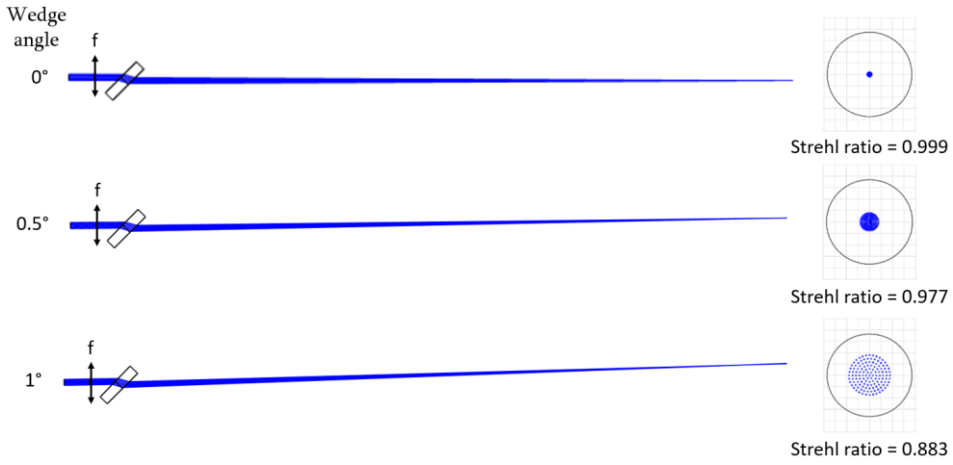

Fig. 2.3. Wedge angle's effect on aberrations of a converging beam. Schematics on the left each start with a 3.6 mm diameter incident beam of 550 nm light that transmits through a paraxial lens with f = 400 mm (corresponding to a vergence of 0.625 D if preceded by a transverse magnification of ½). Light after the lens focuses through 6 mm thick wedge plate beam splitter made of fused silica and tilted at 45°. The wedge angle is varied from 0° to 1° (from top row to bottom row) and the corresponding spot diagrams at the focal plane are shown at the right.

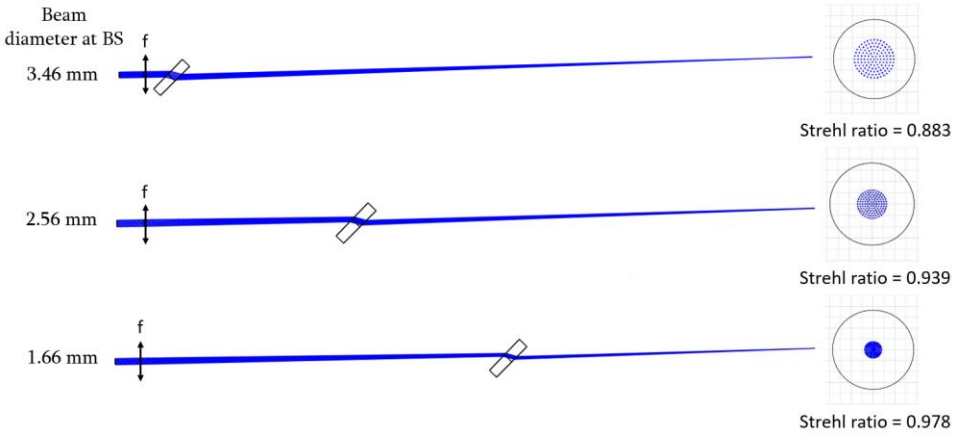

Fig. 2.4. Beamsplitter position's effect on aberrations of a converging beam. Simulation setups are identical to those in Fig. 2.3 except that the wedge angle of the beamsplitter is fixed at 1° and the beamsplitter position is altered instead. The schematic shown in the second row has a beamsplitter placed 100 mm closer to the focal plane than that of the schematic in the first row while the beamsplitter in the schematic of the third row is placed 200 mm closer. The beam diameter at the plane of the beam splitter is given to the left of the schematics while the corresponding spot diagrams are shown at the right.

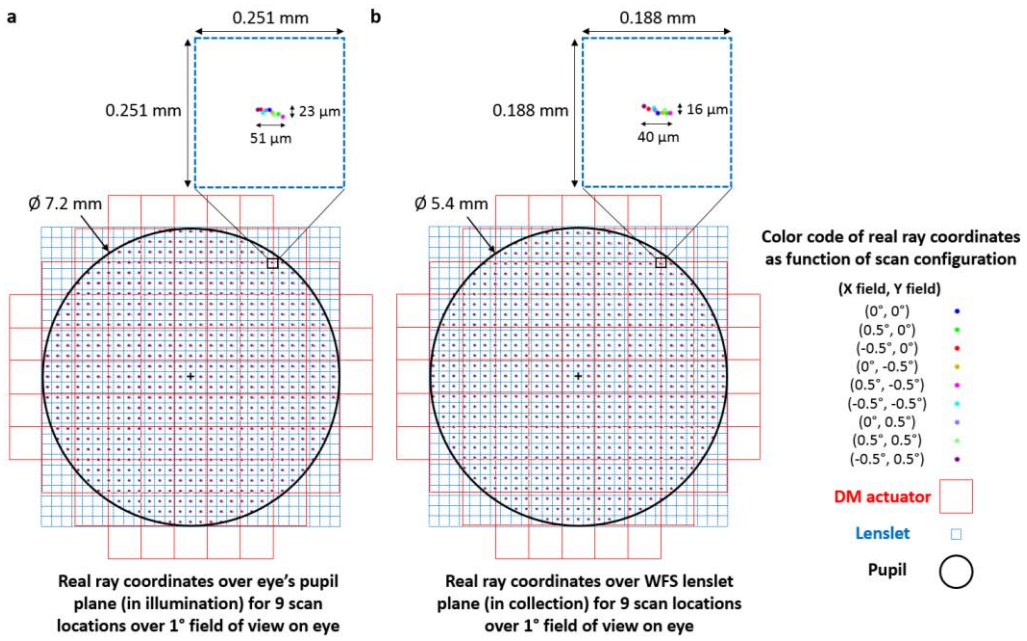

Fig. 2.5. Footprint diagrams show the real ray coordinates over the eye's pupil (a) and WFS lenslet plane (b) for 9 scan locations spanning a 1° square FOV on the eye. A magnification-corrected image of the system's pupil, lenslet array, and DM actuator array are overlaid on top of the footprint diagrams revealing that the wavefront measurement is mainly limited by the sampling density dictated by the WFS's lenslet array rather than the combination of other effects such as pupil aberrations, distortion, and wobble in the illumination and collection paths. The sampling density of the real ray coordinates for the footprint diagrams was chosen to roughly correspond to the magnification-corrected lenslet spacing at the conjugate planes shown in a-b). Magnified insets of a lenslet to the top right of the pupil (where the optical aberrations are worst) are shown at the top right of (a) and (b).

2.3.2 Mechanical design and system construction

The optomechanical design of the AOSLO was designed to prevent vignetting of the optical path, avoid overlapping of optomechanics, and facilitate the optical alignment. The optical path was exported from Zemax optical design software as a solid model to a computer aided design software, Solidworks (Dassault Systemes Solidworks Corp, Waltham, MA), in which the optomechanics were assembled to fit the optical path. In order to aid the alignment, the optical path was oriented such that the entry beam at the beamsplitter and the exiting beam at the eye were both orthonormal to the table. With this implementation, the threaded holes of the optical table could be utilized to perform accurate and repeatable alignment checks. Each optomechanical component was created or imported (if available from the vendor) into the AOSLO solid model assembly. Kinematic stages and mounts within the AOSLO assembly were designed as sub-assemblies that could be adjusted within its mechanical constraints. Accurate modeling of the kinematic stages allowed the AOSLO solid model to be directly referenced for accurate alignment of optomechanics and aided in the selection of kinematic components to ensure they had sufficient degrees of freedom and range of adjustment to support the optical design.

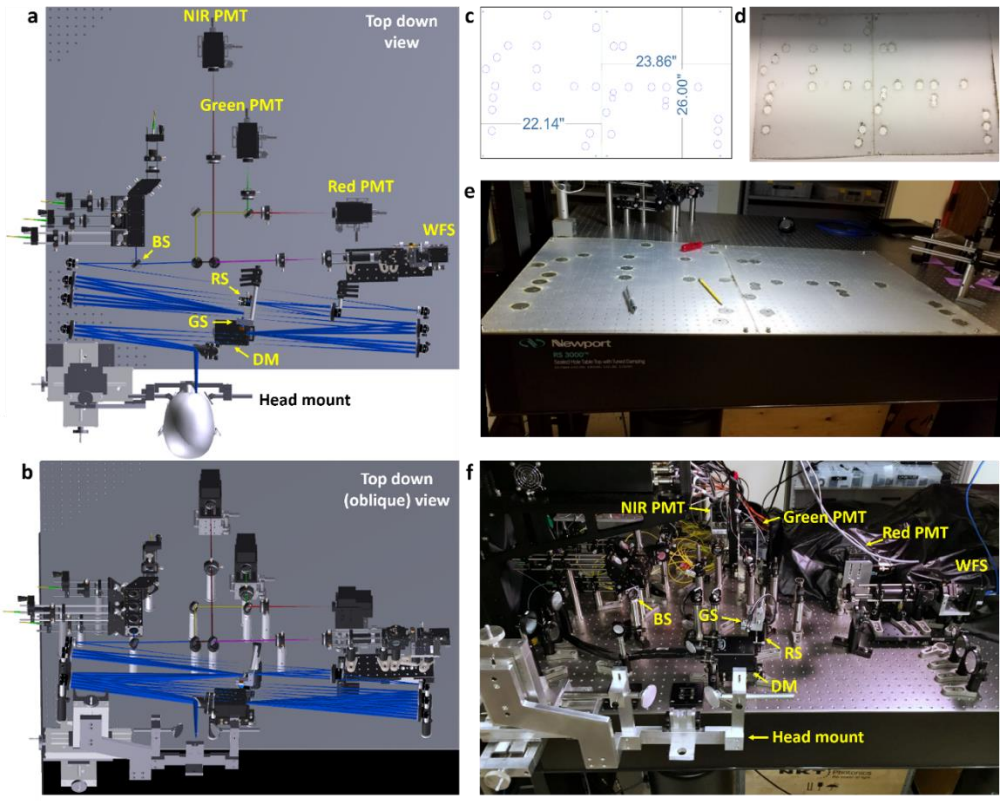

Fig. 2.6. Mechanical design and fabrication of the multi-color AOSLO system. a) Top down view of the optomechanical model of the system within Solidworks. b) Oblique view of the optomechanical model. c) Stencil design indicating the post placement as dictated by the solidmodel shown in a-b). d) Fabricated stencil. e) Stencil applied to optical table. f) Fully-fabricated and aligned multi-color AOSLO system.

The WFS optomechanics were custom-built to align a lenslet array and camera (specified in Table 2.1) with sufficient degrees of freedom for external calibration without sacrificing stability. The WFS camera was anchored to a custom-built adapter plate resting on a tip-tilt kinematic mount which was used to ensure the camera's sensor was perpendicular to the lenslet array. The lenslet array was held by a high precision rotation mount and attached to a flexure XY translation stage for small, stable adjustments to align the lenslet array to the desired axes of the camera. The WFS module was integrated into the AOSLO with two post holders mounted on a linear translation stage to facilitate system integration and alignment.

In order to accurately construct and align the multi-spectral AOSLO system, we used the optomechanical design to create a stencil for the placement of each optomechanical component on the optical table. As shown in Fig. 2.6(a-b), the spatial coordinates of each post's location was exported into an Adobe Illustrator drawing shown in Fig. 2.6(c). To assure the correct component placement relative to the optical table, multiple reference holes (corresponding to several threaded holes on the optical table) were added to the drawing. The drawing was then laser cut onto a polycarbonate sheet shown in Fig. 2.6(d) and applied as a stencil to trace each component's location onto the optical table using a pencil depicted in Fig. 2.6(e). For posts in the design that could be held at a variable height via post holders, their alignment was determined using virtual calipers from the solid model and implemented with sub-millimeter precision using digital calipers. To reduce ambiguity in the optical path length between optics held by kinematic

positioners (especially those that allow for a large amount of piston), the pegs for each kinematic mount in the system were coarsely set to the position dictated by the solid model before the final optical alignment.

2.3.3 Alignment procedure for the AOLSO light delivery and collection

In order to take full advantage of AO correction, the optical path for each imaging channel must be coincident with that of the wavefront sensing spectral channel. Spectral channels were coaligned by making image and pupil planes coincident across all channels. To allow for the alignment of an image plane without misaligning the corresponding pupil plane, we placed the collimating lens for each spectral channel on an XY translation stage and aligned it to be centered with respect to the single mode fiber adapter. Then we placed a fixed iris in the front focal plane, which is a pupil-conjugate plane. By using a fixed iris in the pupil plane, only the image plane (retinal conjugate) for any spectral channel would need to be fine-tuned for spectral coalignment by adjusting the collimator laterally less than 100 microns, inducing negligible off-axis aberrations.

To bring all spectral channels into focus at the same plane as the retina, the AOSLO requires optical pre-compensation of the eye's longitudinal chromatic aberration (LCA). We implemented compensation by adjusting the input vergences of each spectral channel. In this AOSLO design, we chose the 680 nm spectral channel as the reference channel with 0 D vergence making this path collimated prior to the wedge plate beam splitter and at the eye. With 680 nm as a reference, the LCA of the eye was calculated to have a vergence difference of -0.607 D at 543 nm, 0 D at 680 nm, +0.392 D at 840 nm, and+ 0.5516 D at 940 nm(Atchison & Smith, 2005; Thibos et al., 1990). This vergence shift was implemented for each spectral channel by shifting the axial position of the channel's input fiber such that the image plane for a model eye with a focal length of 100 mm would be 106.46 mm at 543 nm, 100 mm at 680 nm, 96.22 mm at 840 nm, and 94.77 mm at 940 nm. To aid in alignment, a camera was precisely aligned on the order of hundreds of microns with a micrometer at the calculated image plane of the model eye for each spectral channel and the fiber was precisely positioned to minimize the spot size seen on the camera.

2.3.4 Wavefront sensorless adaptive optics to correct static system aberrations

To improve the imaging performance of the AOSLO system and make it robust to minor system aberrations, we utilized wavefront sensorless adaptive optics to determine the optimal wavefront shape that maximizes detected light. Our implementation of sensorless adaptive optics is similar to that described by Hofer et al.(Hofer et al., 2011) and applies random perturbations to the deformable mirror shape to optimize for the AOSLO image's mean intensity rather than the wavefront sensor readings. By using a small confocal pinhole (with a sub-Airy disk diameter), aberrated and out-of-focus light is rejected by the confocal pinhole and the wavefront shape that optimizes for mean intensity also corresponds to the wavefront with minimal aberrations.

The wavefront sensorless adaptive optics optimization was performed for all wavelengths and each spectral static correction was compared against the others to find a static correction suitable for all of them. The static correction for 543 nm resulted in a slight decrease in signal intensity for the 840 nm spectral image and the static correction for 840 nm also showed a slight decrease in signal intensity for the 543 nm spectral image. This discrepancy in the static system aberration correction between 543 nm and 840 nm is due to the large vergence difference between the two channels imposed to compensate for the eye's longitudinal chromatic

aberration. Therefore the 680 nm static system aberration was used in the system as it was optimal for all spectral channels. Once the deformable mirror shape was optimized based on the detected image's mean intensity, the residual wavefront reading on the WFS was recorded and was assigned as the target shape for subsequent WFS-based AO correction.

2.3.5 Image processing and human subject protocol

The system components and hardware customized for this system are listed in Table 2.1. The custom image acquisition software and AO software are same as that of our previous AOSLO system and have been previously described in(Arathorn et al., 2007; Yang et al., 2010). The image registration techniques used for stabilizing eye motion was a strip-based cross correlation method previously described in(Stevenson et al., 2010; Stevenson & Roorda, 2005).

The University of California Berkeley Institutional Review Board approved this research, and subjects signed an informed consent form before participation. All experimental procedures adhered to the tenets of the Declaration of Helsinki. Mydriasis and cycloplegia were achieved with 1% tropicamide and 2.5% phenylephrine ophthalmic solutions before each experimental session. Subjects bit into a dental impression mount affixed to an XYZ translation stage to align and stabilize the eye and head position. Both subjects (20112L and 20076R) were healthy young adult volunteers. Structural imaging was performed on both subjects using the 543 nm, 680 nm, and 840 nm imaging channels and the 940 nm WFS channel for AO correction.

2.4 Results

After constructing and aligning the multi-spectral AOSLO system, the optical resolution for each spectral channel was measured by collecting a through-focus stack of intensity images of the PSF over a 5 mm depth range in exponential steps around the focus. The illumination PSF was collected with a camera at front end of the imaging system at the image plane of a 100 mm focal length achromatic doublet. The collection PSF was collected by replicating a point source with single mode fiber at the front end of the system and placing a camera at the image plane after the collection lenses, in place of the PMT. The optical resolution was then quantified by using phase retrieval technique(Guizar-Sicairos et al., 2008; Waller & Tian, 2015) to extract the resultant wavefront of each spectral channel. The phase retrieval algorithm utilized through-focus intensity images to iteratively solve for the complex PSF using the Gerchberg-Saxton algorithm(Saxton, 1972). A Fourier transform of the complex PSF was then used to reconstruct the wavefront and determine optical quality metrics like Strehl Ratio, which we used to evaluate resolution for each spectral channel (see Table 2.3).

Table 2.3. Strehl Ratio measurements for the AOSLO's illumination and collection paths per spectral channel

Spectral channel	Illumination	Collection
543 nm	0.95	0.94
680 nm	0.93	0.99
840 nm	0.99	0.96
940 nm	0.97	0.98

The optical design and system alignment were further validated after measuring the system's collection efficiency per spectral channel as a function of confocal pinhole size (see Fig. 2.7). In

this experiment, the sample was a model eye with paper as the retina and the illumination profile at the pupil plane was a top hat with a circular aperture. In the absence of scattering effects, the spatial profile of the light incident on the confocal pinhole is expected to follow that of the double-pass point spread function's encircled energy(Venkateswaran et al., 2004), which follows the black curve on Fig. 2.7. However, scattering within paper is expected to further broaden the light distribution at the confocal pinhole with its own point spread function, which has been shown to approximately follow a Lorentzian function(Modrić et al., 2014) (see dashed lines in Fig. 2.7). To measure the paper's scattering point spread function, a separate simplified setup with the same illumination profile and model eye from the AOSLO was used to measure the collection efficiency per imaging channel vs confocal pinhole size (see dense dotted lines in Fig. 2.7). Comparing the encircled energy for the multi-spectral AOSLO with the measured encircled energy of the simplified setup, we see that our results match quite closely indicating the multi-spectral AOSLO's near-theoretical collection efficiency across all imaging channels. As reference, we also plot related work from Sredar et al.(Sredar et al., 2018) and an encircled energy curve resulting from the convolution between the theoretical double-pass point spread function (without scattering) and a 2 μm FWHM Lorentzian for each imaging channel. This latter plot matches closely to the encircled energy measurements of our simplified setup indicating that the paper of our model eye has a PSF that approximately equals to a 2 μm FWHM Lorentzian function.

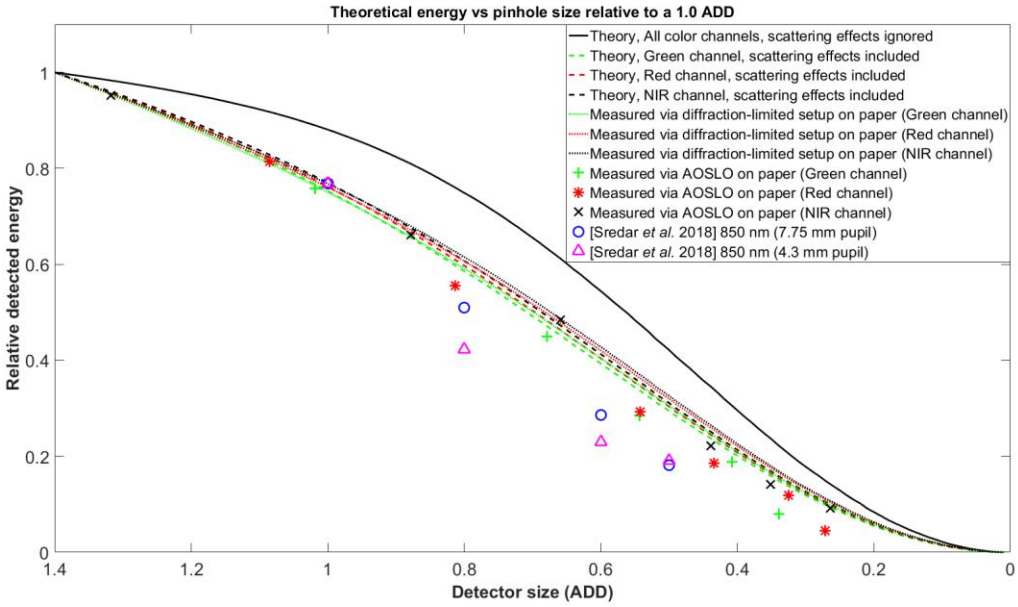

Fig. 2.7. Theoretical and experimental energy at the confocal pinhole for the AOSLO and a separate diffraction-limited setup when imaging the same model eye and spectral imaging channels. Theoretical estimates without scattering were calculated by integrating the double-pass point spread function at the plane of the confocal pinhole for different pinhole sizes. Theoretical estimates incorporating scattering were calculated by convolving the double-pass point spread functions by a 2 μm FWHM Lorentzian function and integrating the result for different pinhole sizes. All curves were normalized to unity for a confocal pinhole size of 1.4 ADD. The detected energy of the largest pinhole size for each spectral channel was normalized to the value of the curve generated from measurements using the diffraction-limited setup on paper for the corresponding spectral channel and pinhole size.

To test the performance of our multi-spectral AOSLO system for imaging the human eye, we obtained preliminary imaging results from two emmetropic, healthy human adult volunteers at the fovea after artificial dilation. Videos of the foveal cone mosaic were acquired in all imaging channels at 30 Hz with a 0.83° FOV and averaged for 10 seconds to produce the averaged images shown in Fig. 2.8. The illumination powers at the eye and ratio of the maximum permissible limit for a 0.75° FOV were 4.6 µW (0.42), 69 µW (0.16), 87 µW (0.08), and 94 µW (0.05) for the 543 nm, 680 nm, 840 nm, and 940 nm spectral channels, respectively. For all imaging sessions, only one imaging channel was utilized at a time together with the wavefront sensing channel, although simultaneous imaging with all channels could be permitted under the maximum permissible safety limits(ANSI, 2014; Delori et al., 2007).

For the spectral analysis, 100 frames were registered for motion using strip-wise cross correlation algorithm and averaged for the 680 nm and 840 nm spectral channels. To account for the low power used in the 543 nm imaging channel, a total of 300 frames were registered and averaged for the spectral analysis. The images were all cropped to the same region of interest and the histograms of the images were normalized across the full bit depth to replicate the same contrast. The foveal cones for each subject were spatially registered for all spectral channels to ensure the same spatial frequencies were present in all images. The discrepancies in the luminance profile was due to the different spectral channels and the different acquisition time points.

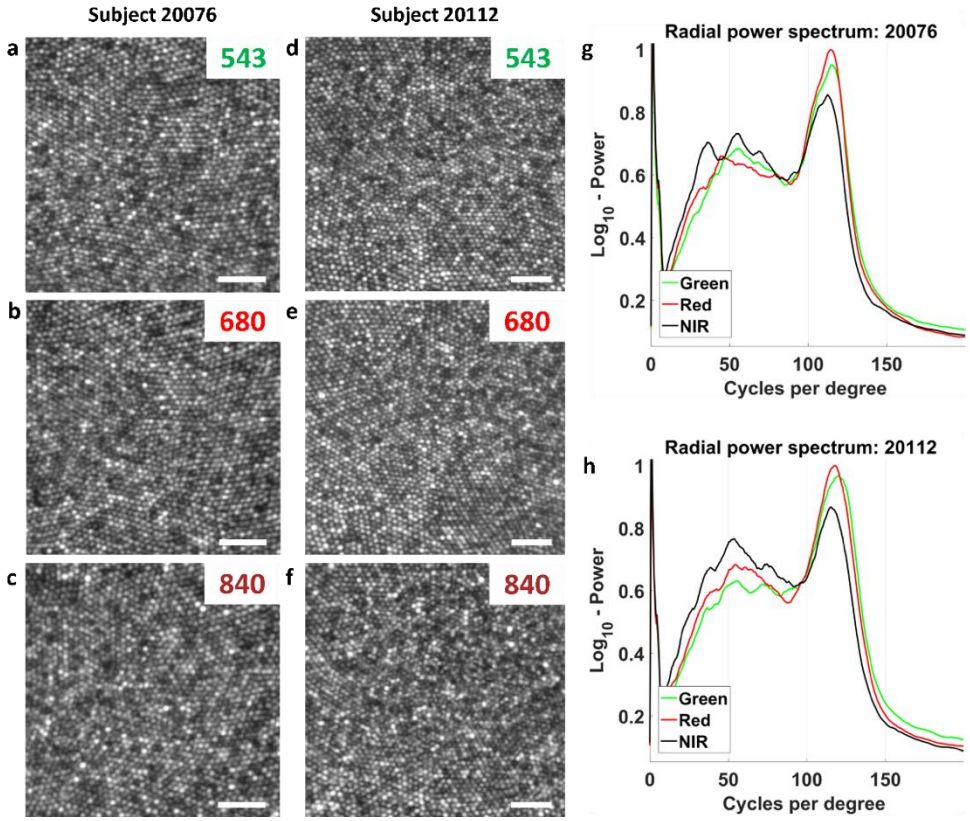

Fig. 2.8. Foveal imaging results across all spectral channels from healthy hyperopic (a-c, Subject 20076) and emmetropic (d-f, Subject 20112) volunteers after artificial dilation and ~0.5 ADD pinhole configuration. a,d) 543 nm channel image. b,e) 680 nm channel image. c,f) 840 nm channel

image. g,h) Radial power spectrums across all imaging channels for Subjects' 20076 and 20112, respectively. Scale bars, 20 μm.

The spatial frequency information from images of different spectral channels was quantitatively compared for both subjects using the radially-integrated power spectrum (Fig. 2.8(g), 2.8(h)). The power spectrum from each channel was normalized to the area within each curve such that the same amount of information is encapsulated in each distribution. As expected by diffraction-theory(Abbe, 1873), the 543 and 680 nm imaging channels demonstrated sharper images with higher resolution and their radial power spectrums exhibited a larger peak at the cone-packing density (~110-125 Cycles/degree) than that of the 840 nm imaging channel.

However, the benefits for the shortest wavelength, 543 nm, was not fully realized compared to 680 nm with a 0.5 ADD pinhole configuration. There are several possible reasons for this. The primary cause, put forth in the introduction, was that the different optical paths between 940 and 543 nm light might have resulted in just enough high order aberration differences to preclude an optimal correction. But other factors might also contribute: The lower power that was used for green light imaging might have resulted in slightly poorer eye motion correction and consequent image registration. Finally, the high PMT detector gain required for green light detection might have resulted in more high frequency noise (~150-200 cycles/degree) compared to the other channel. An increase in power in this part of the spectrum would affect the power spectrum normalization in a way to reduce the relative height of its peak. Nevertheless, the images remain very good at short wavelengths despite all possible reasons for it not to be.

Overall, the main practical implications are the systematic validation of the theoretical design of the AOSLO system and in experimentally quantifying the resolution with foveal cones in both 543 nm and 680 nm spectral channel while imposing a 1.2 Diopter vergence shift between the imaging wavelengths and the wavefront sensing wavelength at 940 nm. This study shows the practical limits of the different spectral channels and that both 680 nm and 543 nm imaging can be used for structural foveal imaging, psychophysical experiments in the fovea(Tuten et al., 2012, 2019) and measuring and correcting for TCA(Boehm et al., 2018; Fernández et al., 2006; Harmening et al., 2012).

2.5 Conclusion

We have demonstrated a multi-spectral AOSLO design with diffraction-limited illumination and collection to achieve high-resolution, high-throughput retinal imaging. After constructing and validating the AOSLO performance, images were acquired at the foveal center from two healthy subjects to demonstrate the system's capability to visualize foveal photoreceptors in all imaging channels with wavefront correction based on a separate spectral channel. The use of this methodology and system design may provide increased collection efficiencies in other SLO or AOSLO designs that employ large vergence ranges over multiple spectral channels.

Funding

National Institutes of Health (National Eye Institute) (T32EY007043, R01EY023591, U01EY025501, P30-EY003176), Alcon Research Investigator Award, Minnie Flaura Turner Memorial Fund for Impaired Vision Research, Soroptimist International Founders Region Fellowship.

Disclosures

AR:USPTO #7,118,216, "Method and apparatus for using AO in a scanning laser ophthalmoscope" and USPTO #6,890,076, "Method and apparatus for using AO in a scanning laser ophthalmoscope". These patents are assigned to both the University of Rochester and the University of Houston and are currently licensed to Boston Micromachines Corporation in Cambridge, Massachusetts. Both AR and the company may benefit financially from the publication of this research.

Citation for this Paper: Mozaffari, S., LaRocca, F., Jaedicke, V., Tiruveedhula, P. & Roorda, A. Wide-vergence, multi-spectral adaptive optics scanning laser ophthalmoscope with diffraction-limited illumination and collection. *Biomed. Opt. Express* 11, 1617 (2020).

This paper was published in 2020. The modeling in this paper was done by Francesco LaRocca and Volker Jaedicke; the electronic implementation and testing was supported by Pavan Tiruveedhula and Austin Roorda. The building, aligning, experimental optical testing of the AOSLO, and the writing of the paper was done by Sanam Mozaffari.

3 Versatile multi-detector scheme for adaptive optics scanning laser ophthalmoscopy

3.1 Abstract

Adaptive optics scanning laser ophthalmoscopy (AOSLO) is a powerful tool for imaging the retina at high spatial and temporal resolution. In this chapter, we present a multi-detector scheme for AOSLO which has two main configurations: pixel reassignment and offset aperture imaging. In this detection scheme, the single element detector of the standard AOSLO is replaced by a fiber bundle which couples the detected light into multiple detectors. The pixel reassignment configuration enables high resolution imaging with an increased light collection. The increase in signal-to-noise ratio (SNR) from this configuration can improve the accuracy of motion registration techniques. The offset aperture imaging configuration enhances the detection of multiply scattered light, which improves the contrast of retinal vasculature and inner retinal layers similar to methods such as nonconfocal split-detector imaging and multi-offset aperture imaging.

3.2 Introduction

Adaptive Optics Scanning Laser Ophthalmoscopy (AOSLO) is a powerful retinal imaging tool with high spatial and temporal resolution(Roorda et al., 2002). It allows for the imaging of retinal structures at a cellular scale, such as cone photoreceptors, at localized positions within retinal tissue. An AOSLO is a confocal scanning laser microscope that incorporates adaptive optics and utilizes the eye's optics as the microscope objective(Webb et al., 2011). Just as in confocal microscopy, a focused spot is scanned across the sample (the human retina) and a single element integrating detector captures the backscattered light at every scan position. A pinhole is placed in front of the detector at a plane conjugate to the focused spot on the sample to reject out-of-focus light. The diameter of this pinhole is one of the key elements that governs the resolution of the microscope(Wilson & Carlini, 1987). The lateral resolution is improved by a factor of root 2 over a widefield flood illumination instrument when a infinitesimally small pinhole is introduced. Increasing the pinhole size allows for more light throughput at the cost of decreasing the resolution. Due to this trade off between signal and resolution, the common pinhole size for AOSLO is generally designed to fall between 0.5 ADD and 1 ADD(Dubra & Sulai, 2011; Sredar et al., 2018), where ADD refers to the Airy Disc Diameter, determined by ADD = 2.44 * lambda f /D, where f is the focal length of the collector lens, lambda is the wavelength of light and D is the beam diameter.

In this chapter, the single element integrating detector is replaced by a multi-detector consisting of a bundle of 7 multi-mode fibers in the form of a hexagonal array. Each fiber is directly coupled to a photomultiplier tube enabling 7 simultaneous image acquisition channels. Multi-detection schemes offer the ability to extend imaging of scanning systems beyond the traditional confocal mode.

One way to employ multi-detector imaging is pixel reassignment, in which images from individual detectors are registered and added(Sheppard, 1988). The resolution of the final image is governed by the size of one detector element as in a standard confocal microscope(Defrise & De Mol, 1992; Sheppard, 1988), but by combining the signal from multiple detectors, the system throughput is increased. Pixel reassignment methods have been successfully applied to improve resolution and SNR in confocal fluorescence microscopy using detector arrays(Castello et al.,

2015; Huff, 2015; Roider et al., 2016; Zhu et al., 2017) or cameras (Azuma & Kei, 2015; De Luca et al., 2013; Müller & Enderlein, 2010; Roth et al., 2013). In order to improve the acquisition speed, camera-based methods have also been combined with multi-spot excitation(York et al., 2012). Alternatives to this digital post-processing approach that employ a camera with analog, all-optical processing have also been demonstrated(Azuma & Kei, 2015; De Luca et al., 2013; Roth et al., 2013; Schulz et al., 2013; York et al., 2013) and recently implemented for a scanning laser ophthalmoscope without adaptive optics(DuBose et al., 2019). However, the reduced system complexity for this all-optical processing comes with the price of less flexibility in terms of data post-processing.

A multi-detector scheme can also be reconfigured to facilitate the collection of multiply scattered, and refracted light, which has proven to have great utility for retinal imaging. Detection of non-confocal, multiply-scattered light has been used to reveal subretinal structures(Elsner et al., 1996) and retinal pigmented epithelium cells in the human retina(Scoles et al., 2013). Asymmetric, or offset aperture detection schemes (i.e collecting and/or comparing multiply-scattered light from different directions relative to the confocal aperture) have revealed transparent and/or refracting structures in the retina including photoreceptor inner segments(Scoles et al., 2014), blood vessels(Chui et al., 2012), blood cells(Guevara-Torres et al., 2016), horizontal cells(Guevara-Torres et al., 2015) and ganglion cells(Rossi et al., 2017).

The parallel nature of multi-detector schemes offer increased efficiency, flexibility and fidelity over single acquisition(Chui et al., 2012), or multiple serial acquisition(Rossi et al., 2017) techniques for offset aperture detector imaging. In the earliest implementation, simultaneous collection of two spatially offset channels was achieved by using a reflective mask to separate nonconfocal and confocal light; the light on either side outside a central area being transmitted through a mask and collected by two nonconfocal detectors, while the light reflected off the center of the mask was directed to a confocal detector(Scoles et al., 2014). More recently, this approach with a static mask has been further modified using a programmable, pixelated reflector to direct the light outside the confocal aperture into two detectors(Sapoznik et al., 2018) which allowed for the use of arbitrary aperture shapes and orientations for vessel imaging. In the past year, the use of fiber bundles have been demonstrated as a more convenient and robust way to detect spatially offset, nonconfocal light in AOSLO(Ferguson et al., 2018; Jaedicke et al., 2018; Mozaffari et al., 2018).

The multi-detector scheme described in this chapter can be configured to offer both pixel reassignment and offset aperture imaging modalities. In the results section, we describe how the system is set up, then we show imaging results from healthy human volunteers. Finally, we discuss further applications and improvements in the discussion section.

3.3 Methods

3.3.1 AOSLO system with multi-detector

The specific multi-wavelength AOSLO system is described in more detail in previous publications(Grieve et al., 2006) and so only the details that are most pertinent to this chapter are described here. Only the 680 nm imaging channel was modified in the multi-wavelength AOSLO for the multi-detector scheme. A system schematic is shown on the left of Fig. 3.1.

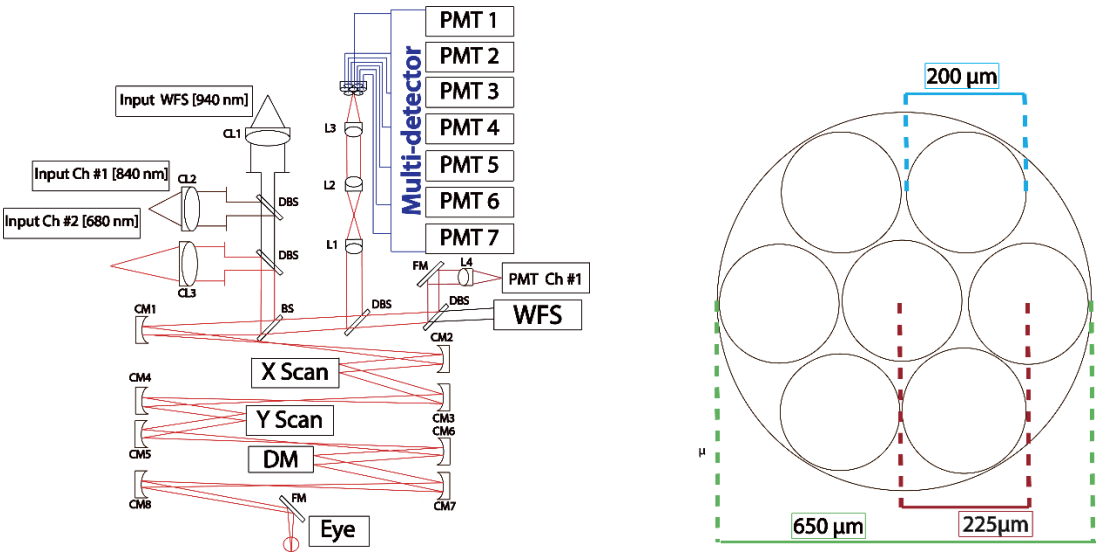

Fig. 3.1. Schematic of the AOSLO system with a red beam indicating the 680nm imaging multi-detector channel, maroon beam for the 840nm imaging channel, and a black beam for the 940 nm wavefront sensor channel. The key component in the multi-detector setup is the 4f telescope (L2-L3) which relays the image of the focused spot on the retina to the fiber core. The geometry of the multi-detector's fiber bundle is shown on the right. (BS: Beamsplitter, CL: Collimating Lens, CM: Curved Mirror, L: Lens, DBS: Dichroic Beamsplitter, DM: Deformable Mirror, PMT: Photomultiplier Tube, WFS: Wavefront Sensor)

The system's optical design was modeled after the AOSLO design described by Dubra et al.(Dubra & Sulai, 2011). The front end (double-pass part of the system comprised of the optics between the first beam splitter (BS) and the eye) consists of afocal telescopes, formed by pairs of off-axis spherical mirrors in a non-planar arrangement. The eye's pupil plane is imaged onto a deformable mirror (DM97-08, ALPAO, Montbonnot-Saint-Martin, France), a galvo scanner (6210h, Cambridge Technology, Bedford, USA) and a resonant scanner (SC-30, EOPC, Ridgewood, USA). The deformable mirror is the pupil stop with a diameter of 7.2 mm. Light from a supercontinuum laser (SuperK Extreme, NKT Photonics, Birkerod, Denmark) is bandpass filtered such that it has a central wavelength of 680 nm (22 nm bandwidth) and 840 nm (22 nm bandwidth) for imaging and 940 nm (10 nm bandwidth) for wavefront sensing. All wavelength bands are combined using a dichroic beamsplitter (DBS) and reflected off a 0.5 degree wedge 10/90 (R:T) beam splitter (BS). After passing through the front end, light backscattered from the retina is descanned and transmitted through the beam splitter into the collection optics. In the case of the multi-detector, the retinal conjugate spot formed by Lens 1 is relayed by a 4f telescope (Lens 2 and Lens 3) onto a multi-mode fiber bundle (BF72HS01, Thorlabs, Newton, USA) in which the fibers are arranged in a closely packed hexagonal array and then split into seven individual fibers. The geometry of the common end of the fiber bundle is given on the right side of Fig. 3.1. The diameter of each individual fiber is 200 µm, while the fiber pitch is 225µm. The overall diameter of the fiber bundle tip is 650 µm, which corresponds to a fill factor of 66%.

3.3.2 Multi-detector telescope

In the original configuration, Lens 1 was the collector lens that focused the 680 nm light to a single confocal pinhole. With a beam size of 3.6 mm and a focal length of 200 mm, the ADD of the focused spot was 92 µm.

A 4f telescope was added to the system to relay an image of that spot onto the fiber bundle. The focal lengths of the lenses in the telescope determine the imaging configuration of the multi-detector since they control the size of the focused spot relative to the fiber bundle core. For pixel reassignment mode, Lens 2 and Lens 3 were set to f = 30mm and f = 200mm (AC254B, Thorlabs, Newton, USA), respectively, to provide a magnification factor of 7, a collection spot size of 614 µm, and a ratio of the fiber core to PSF diameter of 0.33ADD. The entire collection diameter of the fiber bundle was 1.07ADD as shown in Fig. 3.3.

Configuration	Lens 1 Focal Length	Lens 2 Focal Length	Magnification	Point Spread 'ADD'
Pixel Reassignment	30 mm	200 mm	7	614 µm
Offset Aperture	200 mm	30 mm	0.15	13.8 µm

Fig. 3.2. Summary of the optical configuration for the desired point spread for each multidetector configuration.

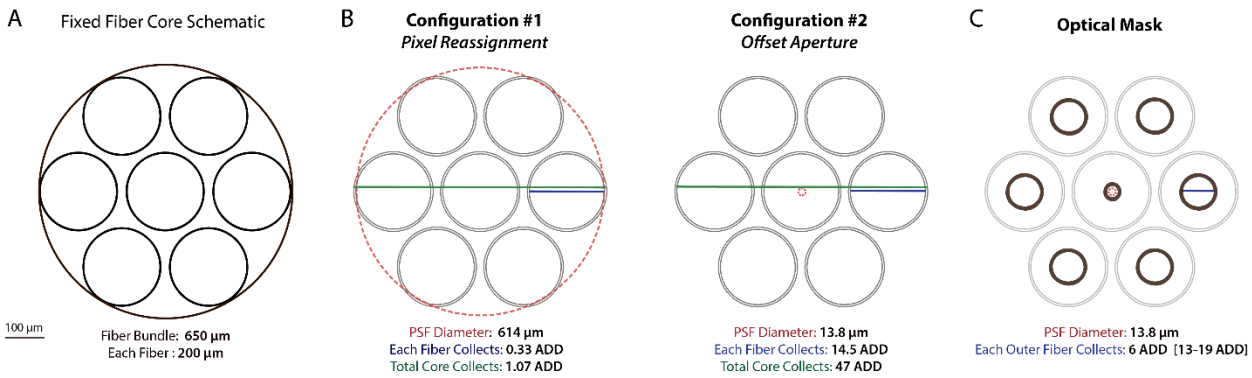

Fig. 3.3. A. Geometry of fiber bundle. B. For pixel reassignment, the collection PSF is magnified by 7 to be the same size of the fiber core, 614 µm. For offset aperture imaging, the collection PSF is magnified by 0.15 to be smaller than the fiber core, 13.8 µm. C. Optical Mask for offset aperture imaging to limit the light collection from 13 to 19 ADD with 6 ADD apertures for each fiber.

For offset aperture imaging, the two lenses in the telescope were merely flipped such that the first lens of the telescope was f = 200 mm, while the second was f = 30 mm for a magnification of 0.15 resulting in a PSF diameter of 13.8 µm and a fiber core-to-PSF diameter ratio of 14.5 ADD. The entire collection area of the fiber bundle was 47ADD in this mode. Additionally, an optical mask was used to collect over a 6ADD diameter aperture for the outer fibers and provide a 2 ADD confocal pinhole for the central fiber. The optical mask was inserted one focal length away from Lens 1 and mounted on a three axis kinematic stage with additional rotation adjustment.

3.3.3 Acquisition and data processing

The common end of the fiber bundle was mounted on a linear kinematic stage (PI 403.8DG, Physik Instrumente, Karlsruhe, Germany), which enabled movement of the detector along the optical axis. Each individual fiber was connected to a PMT (Photo Multiplier Tube). Since 7 identical PMTs were not available, different PMT models (7422-20, 7422-40 and 7422-

50, Hamamatsu, Hamamatsu, Japan) which had similar performance at 680 nm were fiber coupled to the multi-detector. Each of the PMT modules was equipped with an individual gain control to adjust for small differences in performance and light levels at different detection positions. Each channel's signal was further amplified using identical amplifiers (C6438-01, Hamamatsu, Hamamatsu, Japan) for each PMT. Custom electronics were used to correct the black level of the signal, apply a temporal apodization window, and low-pass filter the signal with a cutoff frequency of 10 MHz. Two identical 4-channel framegrabbers (Helios, Matrox Imaging, Dorval, Canada) were used for digitization of the signal and were triggered by a sync signal from the fast scanner. Custom acquisition software allowed for the simultaneous display of up to 8 channels. Frames were acquired at 30 frames per second with pixel dimensions of 512x512 pixels at a 0.8 field of view. The scanners were driven with custom electronics and custom software. Adaptive optics correction was based on a custom Shack-Hartman wavefront sensor and controlled using custom software.

All data processing was done in MATLAB (Mathworks Inc, Natick, USA) and ImageJ(Rueden et al., 2017). Raw videos from all seven channels were first corrected for non-linear sampling due to the sinusoidal waveform of the resonant scanner using calibration data obtained from a grid target. A strip-based stabilization software was used to estimate and correct for eye motion(Stevenson et al., 2010). Frames that contained distortion from motion or blinks were removed and the average image intensity across all frames of the video was taken to form an image. Eye motion data obtained from the central detector was used to register all other acquired videos.

In pixel reassignment mode, images were registered with respect to the image acquired by the central detector. Individual images of the detector elements were displaced d/2, where d is the geometrical distance with respect to the central detector element(Cox et al., 1982). To account for small misalignment errors and the unknown rotation of the fiber bundle, shifts between different imaging channels were computed using a sub-pixel Fourier transform-based algorithm(Guizar-Sicairos et al., 2008) instead of using theoretically determined values. The shifts for each imaging session were calculated from the best quality image set and subsequently applied to all images of the same data set.

For offset aperture imaging, the raw data was contrast enhanced to adjust for the different PMT response characteristics, histogram-matched to account for different PMT amplifier gains, and filtered with wavelet-based denoising to decrease image degradation due to noise. The differences of individual fiber images were taken according to the opposing positions and normalized with respect to their sum. Although the multi-dete○ctor was limited in the number of offset angles, different image processing techniques mentioned in previous literature were applied, but the opposing fiber difference images appeared to provide the strongest contrast(Ferguson et al., 2018; Rossi et al., 2017).

Due to the weak reflective signal within the inner retinal layers, neither the 840 nm nor the 680nm imaging channel had enough SNR to register eye motion. In order to take a complete dataset through depth, the axial focal position of the 680 nm beam and the conjugate multi-detector channel was offset to be anterior to the 840 nm imaging channel by about 200 μm in the retina. In this way, the 840 nm beam was focused on the photoreceptors which offered rich structure for optimal eye motion registration while the offset imaging channel was located just under the nerve fiber layer. By utilizing the 840 nm video to register all of the 680nm multi-

detector videos we are assuming a bulk tissue movement for the lateral translation and the axial movement was considered negligible.

3.4 Results

Subjects: The University of California Berkeley Institutional Review Board approved this research, and subjects signed an informed consent before participation. All experimental procedures adhered to the tenets of the Declaration of Helsinki. Mydriasis and cycloplegia were achieved with 1% tropicamide and 2.5% phenylephrine ophthalmic solutions before each experimental session. Subjects bit into a dental impression mount affixed to an XYZ stage to hold the eye and head still. Both subjects were healthy young adult volunteers, 20112L and 20076R.

3.4.1 Pixel reassignment

The multi-detector telescope was set up to magnify the focused spot by a factor of 7 to form a collection spot size of 614 μm in front of the detector with a fiber core-to-PSF diameter ratio of 0.33 ADD. The optical power output of the imaging system prior to the eye was measured to be 108.6 μW for 940nm and 73.6 μW for 680 nm. First, 10-second videos (300 frames) from each individual detector were recorded and corrected for intra-frame eye motion and an average image was calculated.

In Fig. 3.4 images of the foveal center are shown. Each of the individual fiber images were collected with a 0.33 ADD pinhole. The Averaged Image from Fig. 3.4 was obtained by summing the images obtained from all detectors without applying the pixel reassignment process. In this case, the resolution and contrast was effectively equivalent in resolution and throughput to that obtained through a 1 ADD pinhole, aside from light losses due to the smaller fill factor of the fiber bundle (see discussion).

The Reassigned Image shown in Fig. 3.4 is the sum of all 7 fibers after subpixel registration. The individual multi-detector images are almost indistinguishable in resolution from the Reassigned Image. The radial power spectrum in Fig. 3.4 shows that the high spatial frequencies in the single detector is preserved within the Reassigned Image unlike that of the Averaged Image. In other words, amongst high resolution imaging schemes which are limited in signal throughput, reassigned images collected through the multi-detector system allow for an increase in light collection without compromising image quality.

The benefits of increased light collection in pixel reassignment are illustrated in Fig. 3.5, where the superior performance of pixel reassignment is clearly visible. In panel A, an average of 5 frames from the multi-detector scheme was enough to virtually remove noise and motion artifacts, while the 5 frame average using the single detector scheme still visibly suffered from both. In other words, the use of a multi-detector with the pixel reassignment scheme allowed the acquisition of high SNR images in a shorter period of time.

The importance of SNR improvement within the acquisition time of a single frame becomes more evident in panel B of Fig. 3.5. These images were taken from a location in the retina 71.4 μm superficial to the photoreceptor layer, where the retinal backscattered signal was weak. The SNR of the central channel alone was insufficient for strip-based frame registration, as can be seen in the upper image, which is blurred from uncorrected intra-frame image distortions. In the lower image, a higher SNR video using pixel reassignment was produced prior

to applying the intra-frame eye movement correction algorithm. The resulting image has much higher frequency content and contrast due to the improved image registration accuracy.

The SNR was determined using the radial power spectrum information. The signal was quantified as the power spectrum value at the peak of the cone photoreceptor spatial frequency (~125 cycles per degree) and the noise was quantified as the average signal above 140 cycles per degree, which is just beyond the peak signal expected from the photoreceptor mosaic. The plot on Fig. 3.6 shows that it takes about 3 times longer to reach the same level of SNR as the multi-detector scheme when imaging with a single detector.

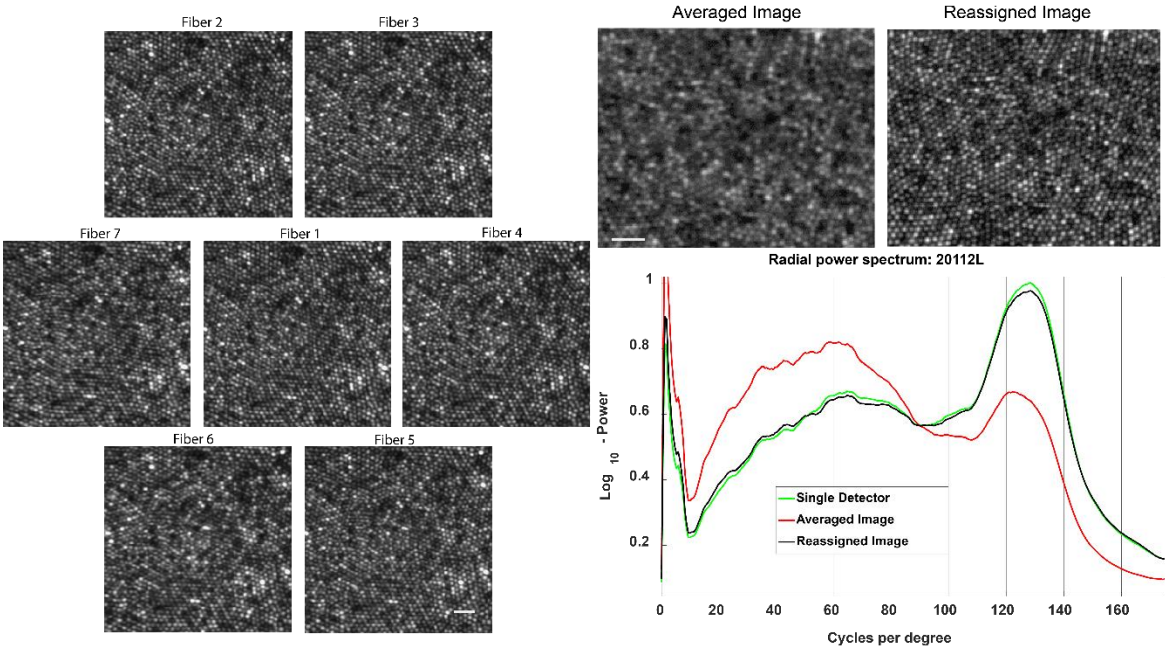

Fig. 3.4. The hexagonal array of images (from Subject 20112) displays the images acquired with each fiber which collects approximately a 0.3 ADD of the collection PSF. The Averaged Image is a simple average of all 7 images from the hexagonal array of images shown on the left. In the Reassigned Image, the 6 outer images are registered to the central image prior to summation. The radial power spectrum quantifies the higher spatial frequency components in the image. The peak at about 125 cycles per degree corresponds to the signal from the periodic cone mosaic. The power at the peak is similar to that of the image obtained via a single detector and the Reassigned Image, but is reduced in the power spectrum obtained from the Averaged Image. Scale bar: 10 µm

3.4.2 Offset aperture imaging

In this configuration, the multi-detector telescope was set up to magnify the spot size by 0.15 to provide a collection PSF diameter of 13.8 µm, which made the fiber core size become 14.5 ADD for offset imaging. The optical power output of the imaging system prior to the eye was measured to be 108.6 µW for 940nm and 73.6 µW for 680nm. For the perfusion analysis the 840nm imaging channel was used for eye motion registration with an optical power output of 52.3 µW. First, three 10-second videos (900 frames) were collected for each individual detector and corrected for intra-frame eye motion.

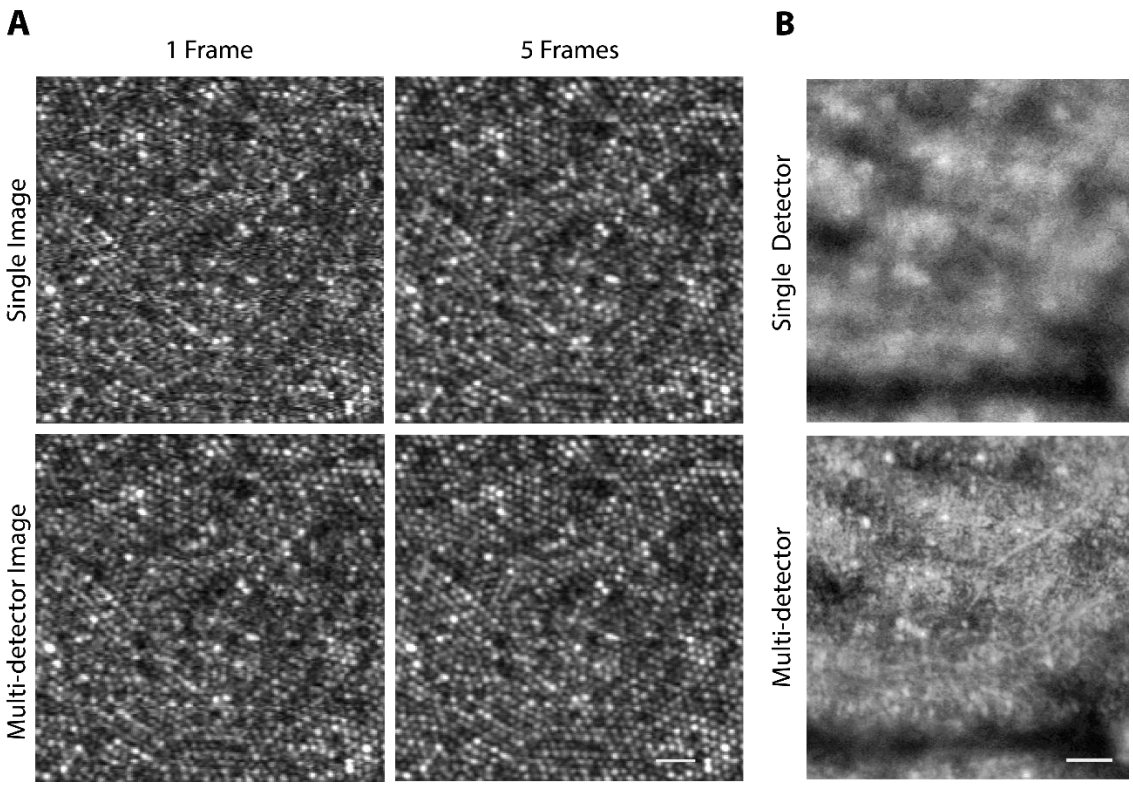

Fig. 3.5. A. SNR analysis of a single channel on top row and the multi-detector on bottom row. B. When the focus is shifted to the inner retina, the top image shows the final image after correcting for eye movements using the video from the single central channel alone. The bottom image shows the final image after correcting for eye movements using a higher SNR, pixel-reassigned video. A. Subject 20112 Scale bar: 10m B. Subject 20076 Scale bar: 20 µm

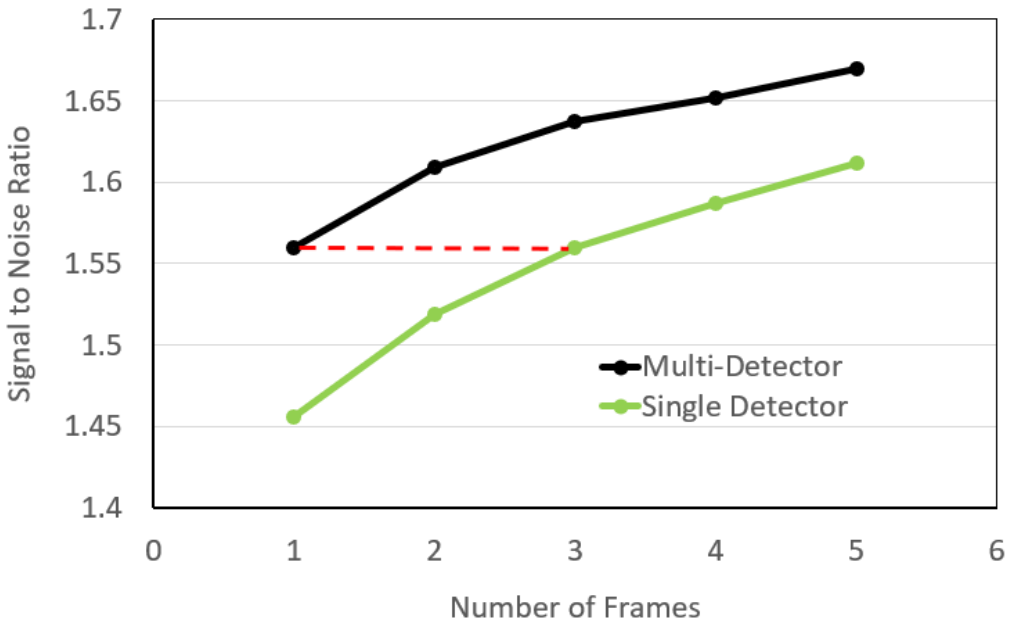

Fig. 3.6. SNR analysis showing that one multi-detector frame is equivalent in SNR to that of a three frame-average single-detector frame.

Offset aperture imaging was able to reveal individual vascular layers and provide depth sectioning throughout the retina. Shown in Fig. 3.7 are the individual fiber images in which the center image is the confocal image and the outer images are from light collected from 13 to 19 ADD away from the center fiber via the outer fibers. To enhance the visualization of the refracted light by retinal structures, the differences of the opposing fibers were calculated and normalized by their sum. Here we can appreciate the different spatial orientations captured from each individual fiber. For example: fiber 2 shows the striations of the nerve fiber layer whereas fiber 6 shows horizontal processes emerging from the purported cell in the center of the image. In effect, each of the images from each fiber is tuned to retinal features of different orientations.

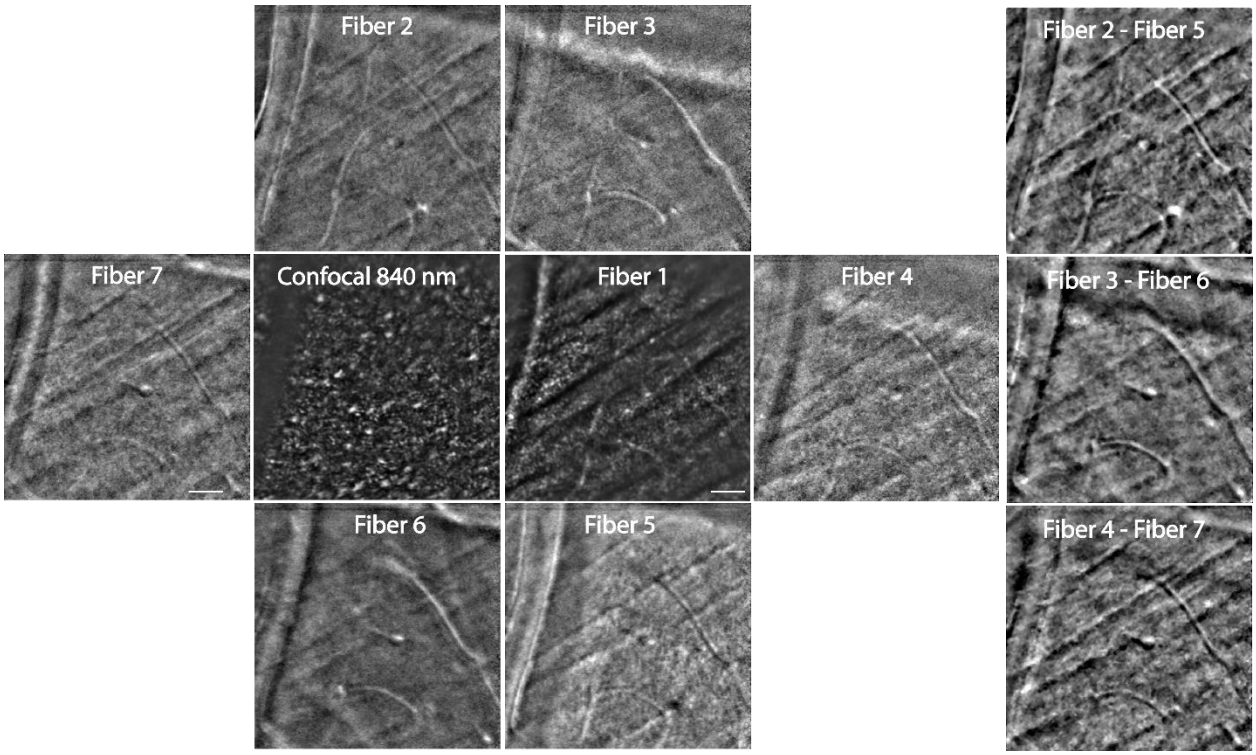

Fig. 3.7. Left: The center images are the confocal images of the axially offset 840 nm channel and the multi-detector. The outer images are from light collected from areas between 13-19 ADD away from the confocal aperture. Right: Difference images from opposing fibers (normalized by their sum). Images were from Subject 20076. Scale bar: 30 μm

In the process of testing the multi-detector scheme for offset aperture imaging, we frequently observed what appear to be cells on the inner surface of the retina that have been reported previously(Burns et al., 2019). Figure 3.8 presents a closer examination of two of these cells in subject 20076. To confirm that these structures were not cross-sections of blood vessels running through the tissue, two analyses were performed. First, we did a perfusion analysis. The perfusion images, shown in the right column of Fig. 3.8, were generated by computing motion-contrast within stabilized videos(Tam et al., 2010). In perfusion images, stable features appear dark while moving features (in this case, blood flow) appear white. The features indicated by green arrows are not apparent in the perfusion images, indicating that these structures are not

likely to be blood vessels. Second, we did a through-focus analysis to rule out that the observed features were optical sections of longer,

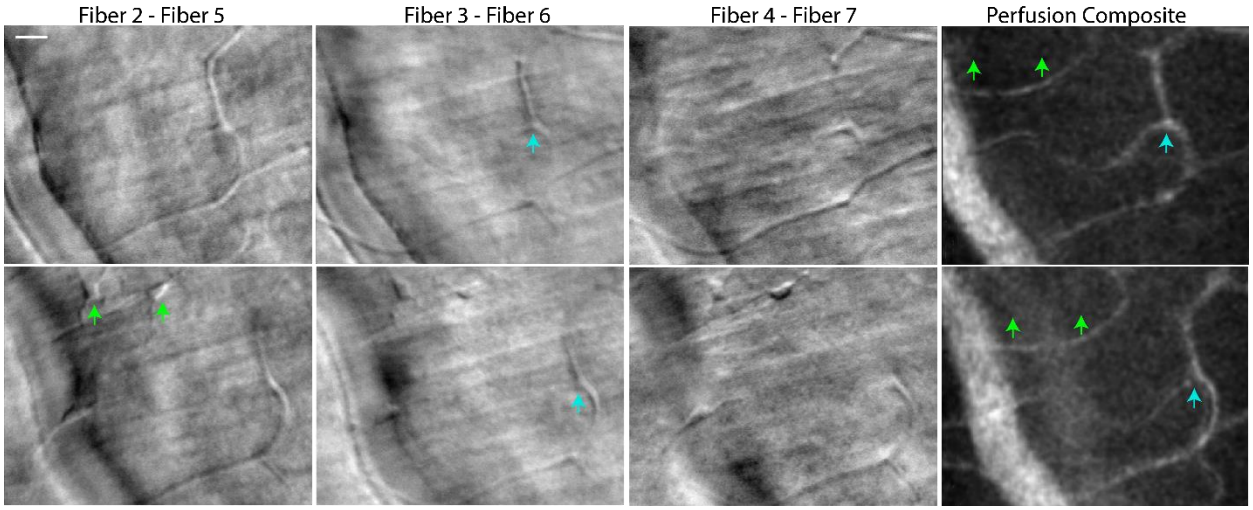

Fig. 3.8. All images are taken at a depth location near the surface of the nerve fiber layer, the bottom row is at 15m anterior (toward the vitreous) of the top row. The first three columns display difference images between opposing fibers. The last column shows perfusion maps of these areas to confirm that the structures indicated by the green arrows are not likely to be blood vessels. The blue arrow indicates a blood vessel for comparison. Images were acquired from subject 20076. Scale bar: 20μm

vessel-like structures. Two depth sections, separated by only 15 μm suggest that the features are isolated to a single layer in the retina. Similar cells residing within the retinal tissue might have a more similar refractive index to the surrounding tissue giving rise to a much smaller offset aperture signal.

3.5 Discussion

We have demonstrated a versatile multi-detector system that uses a fixed fiber bundle detector array and enables either pixel reassignment or multi-offset aperture imaging. To our knowledge, this is the first ever report of pixel reassignment in an AOSLO system. We believe that this detection modality, which offers high resolution and an increase in SNR, can be very useful in some imaging situations. Here is a short list of potential benefits for pixel-reassignment imaging.

1. Minimized phototoxicity: The maximum permissible exposures for visible wavelengths are very low, primarily to prevent photochemical damage to the retina(Morgan et al., 2008). However, the use of these wavelengths for imaging are useful for oximetry(Li et al., 2011), fluorescence imaging (eg. fundus autofluorescence, fluorescein angiography) and other applications. Minimizing exposures without compromise to SNR or resolution will reduce the chances for incidental photo-toxic light exposures.

2. Better characterization of photopigments. Reduced powers at visible wavelengths will slow the bleaching rate of photoreceptors, improving the ability to measure photopigment

absorption properties of individual cone photoreceptors, thereby making measurements of photopigment kinetics and AOSLO cone classing more efficient(Sabesan et al., 2015).

3. Reduced visibility of imaging beams. The scanning beam in current AOSLO systems are always visible. The visibility of the scanning raster can confound certain applications of functional testing in AOSLO systems, including microperimetry(Tuten et al., 2012) and visual psychophysics(Domdei et al., 2018; Sabesan et al., 2016). The ability to reduce light exposure and therefore visibility will be an important step towards invisible imaging.

4. Imaging weakly-reflective layers: Increased SNR will improve imaging and image registration from less reflective layers of the retina, eg. inner and outer nuclear layers. Low backreflected signal makes these retinal structures difficult to analyze. Pixel reassignment both increases the signal throughput and enhances motion registration enabling a structural analysis of these inner retinal layers.

Our particular implementation of the multi-detector AOSLO scheme does come at a cost, which is lost light due to the void space between closely-packed fibers. Gaps between fibers (17% loss) and the cladding of the individual fibers (additional 17% loss) result in a total light loss of 34% compared to a circular aperture with the dimensions of the fiber bundle. The acceptance aperture of the multi-mode fiber is relatively large at 0.39 incurring only minimal losses. Nevertheless, the increase in signal with this scheme is still superior to that of a single detector that achieves the same level of resolution.

An attractive feature of the multi-detector scheme presented here is that it can be quickly reconfigured to different imaging modes by rearranging the same optical components to predetermined locations. This offers versatility to the system, especially for a clinical system in which one might wish to acquire the highest possible resolution images at a specific location with high SNR and then utilize offset aperture imaging to probe the structural health of the transparent layers of the retina in the same patient. In this manuscript, we switched between two modes, which limited the range of offset aperture positions that could be explored. Images taken with the available offsets (13 - 19 ADD) images revealed intricate vascular information, and what appear to be transparent cells lying on the inner retinal surface(Burns et al., 2019). In future implementations, we intend to (i) add a zoom lens to replace lenses 1, 2 and 3 which will enable continuous control of detector offset positions, (ii) explore the use of different optical masks to fine-tune the size and shape of the offset detectors, and (iii) incorporate either an analog difference signal or use balanced detectors to minimize the noise floor and reduce the number of acquisition channels.

3.6 Conclusion

The multi-detector scheme is a versatile detection scheme enabling two different imaging configurations. The pixel reassignment configuration allows for more efficient light collection while preserving high spatial resolution, resulting in improved registration of natural eye movements in post-processing. The multi-offset imaging configuration reveals hidden phase structures such as blood vessels and individual cells.

Funding

National Institutes of Health (National Eye Institute) (T32EY007043, R01EY023591, U01EY025501, P30-EY003176), Alcon Research Investigator Award, Minnie Flaura Turner Memorial Fund for Impaired Vision Research, Soroptimist International Founders Region Fellowship.

Disclosures

AR:USPTO #7,118,216, "Method and apparatus for using AO in a scanning laser ophthalmoscope" and USPTO #6,890,076, "Method and apparatus for using AO in a scanning laser ophthalmoscope". These patents are assigned to both the University of Rochester and the University of Houston and are currently licensed to Boston Micromachines Corporation in Cambridge, Massachusetts. Both AR and the company may benefit financially from the publication of this research.

Citation for this Paper: Mozaffari, S., Jaedicke, V., Larocca, F., Tiruveedhula, P. & Roorda, A. Versatile multi-detector scheme for adaptive optics scanning laser ophthalmoscopy. Biomed. Opt. Express 9, 5477 (2018).

This paper was published in 2018. Half of the theoretical modeling, image analysis and writing of this paper was done by Francesco LaRocca and Volker Jaedicke. The electronic implementation and testing was supported by Pavan Tiruveedhula and Austin Roorda. The building, aligning, AOSLO implementation, image analysis, and the writing of the paper was done by Sanam Mozaffari.

Chapter 4. Adaptive optics optical coherence tomography with fast and accurate real-time tracking

4.1 Abstract

One of the main obstacles in high-resolution 3-D retinal imaging is eye motion which causes blur and distortion artifacts that require extensive post-processing to correct. Here we have implemented real-time, active eye motion corrected adaptive optics optical coherence tomography (AOOCT) by using adaptive optics scanning laser ophthalmoscope (AOSLO) for adaptive optics correction and eye motion tracking. We describe the system design and quantify the performance of an active stabilization for a AOOCT system using an AOSLO for image-based eye tracking. We have implemented a focus adjustment for the AOOCT independently while maintaining high fidelity photoreceptor mosaic for active motion correction. This system enables spatially targeted retinal imaging which as well as volume averaging over entire imaging sessions with minimal processing.

4.2 Introduction

Optical coherence tomography (OCT) is a non-invasive interferometric imaging technique which can record images in 3 dimensions. Many methods of OCT have been developed ranging from ophthalmic techniques of swept source and spectral domain(Choma et al., 2003; de Boer et al., 2003) to new methods of high resolution (Drexler, 2001; Maciej Wojtkowski et al., 2004) and additionally incorporating adaptive optics (AO) for further resolution improvement (Hermann et al., 2004; Miller et al., 2003; Zawadzki et al., 2005; Zhang et al., 2005). OCT has been valuable clinically for its functional imaging techniques to evaluate the vasculature via angiography (Choi et al., 2013; Jia et al., 2012; Migacz et al., 2019) and functional cellular changes in the retina (Azimipour, Migacz, et al., 2019; Bizheva et al., 2006; Jonnal et al., 2007, 2012; Kocaoglu et al., 2016; Srinivasan et al., 2009). Due to OCT's high volumetric resolution and rapid acquisition speeds, it has become a standard ophthalmic instrument for diagnostics (Shaipanich et al., 2017; Swanson & Fujimoto, 2017).

However even during fixation, OCT images are subject to motion artifacts caused by ever-present ocular movements. Most modern commercial systems now employ some form of active tracking to mitigate these artifacts, but these trackers are relatively slow and have limited accuracy so that most clinical data, upon close inspection, still contain artifacts caused by motion (Brea et al., 2019; Zawadzki et al., 2014). For commercial OCT systems and many clinical applications, this is generally acceptable; however, for high resolution and/or research-application OCT systems, these errors remain problematic. Attempts to acquire a sequence of B-scans from a fixed location over any length of time in a human eye, for example, is all but impossible. In such systems, with a few exceptions (Braaf et al., 2013; Vienola et al., 2012) all efforts to track any structure over time has required imaging an entire volume sequence to ensure that the structures of interest are captured in every frame (volume). Careful post-processing is then required to accurately register each volume prior to making any quantitative measures of that structure(Pandiyan et al., 2020). This has resulted in a new sub-field of research that develops algorithms and methods dedicated to motion correction (Azimipour, Zawadzki, et al., 2018; Kraus et al., 2012; Ricco et al., 2009) and volumetric motion correction(Liu et al., 2017; Zhenghan et al., 2020) . There have been additional attempts at mitigating eye movements mainly by increasing temporal acquisition rates

by using MHz-rate swept sources (Choi et al., 2013), implementing cylindrical lenses for line field system (Pandiyan et al., 2020) and multiplexing cameras to quadruple the acquisition rate (Kocaoglu et al., 2014), full field implementation (Hillmann et al., 2016; Spahr et al., 2015) and bidirectional scanning (Blatter et al., 2013; Potsaid et al., 2012). Although the point acquisition rate for these imaging systems is in the MHz to kHz range, the resultant SNR and temporal resolution during functional recording is limited by the volume acquisition rate.

An alternate method to mitigate eye movements is to measure the eye's movement and actively correct for the eye motion for a retina-stable OCT. There are many ways to measuring eye movements the most common include using magnetic search coils (Hageman et al., 2021; Li et al., 2021; Robinson, 1963), dual-Purkinje tracking(Cornsweet & Crane, 1973), and systems that estimate motion based on pupil position and/or lens reflections relative to reflections from the cornea (Martinez-Conde, 2006; Morimoto & Mimica, 2005; Świrski et al., 2012; Zhu & Yang, 2002). Although these methods are still used, they lack the spatial precision necessary to accurately mitigate eye motion for imaging since the eye is not a rigid body resulting in a disparity between motion of the elements in the anterior portions of the eye and retinal motion(Bowers et al., 2019). The tracking methods with the best accuracy for estimating retinal motion are those that image the retina directly. Retinal-image-based methods were first demonstrated using camera-based methods (Fonda et al., 1983; Pomerantzeff et al., 1979) and eventually using lasers via a scanning laser ophthalmoscope (SLO) (Mainster et al., 1982; Webb & Hughes, 1981). An SLO utilizes the ocular optics as an objective to image a single point source on the retina and records the intensity of the light scattered back from this single point, improving the spatial resolution; this point source was scanned in a raster pattern to image patch of the retina and replicate an enface image. The further development of the confocal SLO (Webb et al., 2011) utilized a pinhole in the detection plane to reject multiply scattered light from different focal depths improving both lateral resolution and depth sectioning.

The SLO was suggested as a candidate technology for tracking eye motion because of its high frequency imaging and high spatial resolution (Mainster et al., 1982). It was initially implemented using frame-rate measures of eye motion for psychophysical tasks (Timberlake et al., 1986; Wornson et al., 1987) and vision tests (Wornson et al., 1987). Further developments in SLO-based eye tracking leveraged the 'rolling shutter' feature of SLO for higher-frequency eye motion analysis to track saccades (Stetter et al., 1996) and enable overall improvements in eye tracking accuracy and speed (Mulligan, 1997). Improvements in SLO resolution using adaptive optics (AO) (Roorda et al., 2002) and development of specialized FPGA based hardware and software has enabled SLO-based system to track the eye in real time approaching kHz rates with accuracies better than 1 minute of arc and 2.5 millisecond latency based on the stimulus position within the raster(Arathorn et al., 2007, 2013; Sheehy et al., 2012; Stevenson et al., 2010; Stevenson & Roorda, 2005; Yang et al., 2010).

The active tracking and targeted stimulation platform developed for AOSLO (Tuten et al., 2012; Yang et al., 2010) has facilitated multiple fields including the clinical sciences from vision tests in acuity (Anderson et al., 2020, 2017; Ratnam et al., 2017) to diagnostics via microperimetry (Foote et al., 2020; Tu et al., 2017; Tuten et al., 2012, 2017, 2019) and basic sciences from probing the photoreceptors to the neurons downstream to characterize spatial, temporal and color vision pathways (Arathorn et al., 2013; Bruce et al., 2015; Harmening et al., 2012, 2014; Sabesan et al., 2016; Schmidt et al., 2018, 2019; Sincich et al., 2009; Yao & Wang, 2015). Active tracking was also implemented using a tracking SLO (with no adaptive optics)(Sheehy et al., 2015) to actively

guide an OCT (Braaf et al., 2013; Vienola et al., 2012). In this chapter, we further develop this technology to an adaptive optics platform with an AOSLO tracking and guiding the eye motion correction of an AOOCT.

4.3 Materials and Methods

An AOSLO is utilized to track the eye motion and actively drive a scanner to stabilize an AOOCT in real-time on a fixed location in the human retina. An OCT system was integrated into an AOSLO system with a dichroic mirror just before the deformable mirror such that OCT would take advantage of the adaptive optics correction of the aberrations of the eye. The AOSLO has a tracking accuracy of less than 0.1 arcmin(Sheehy et al., 2012, 2015) and reports an eye motion traces in real time to actively drive the OCT scanner(Braaf et al., 2013; Vienola et al., 2012) resulting in a stabilized AOOCT fixed on the retina. The AOSLO and AOOCT videos were recorded in sync such that each frame of the AOSLO video corresponds to 4 B-scan AOOCT frames at 120 Hz. The motion correction accuracy was experimentally quantified with a moving model eye with a driven galvo scanner. To show the stabilization capabilities of the system, retinal images were taken with the AOSLO-AOOCT for two healthy subjects.

4.3.1 AOSLO System Design

This multi-spectral AOSLO system is described in more detail in Chapter 2 and Chapter 3(Mozaffari et al., 2018, 2020), and so only the details that are most pertinent to this chapter are described here. The optical schematic is shown below in Figure 4.1. Red rays indicate the AOSLO path, blue rays indicate the AOOCT path, and purple rays indicate where the beams from the two systems become coaligned with a dichroic mirror.

The AOSLO uses a supercontinuum light source from which 4 wavelengths are separated out and coupled into single-mode fibers. The wavelengths are 543 ± 11 nm, 680 ± 11 nm, and 840 ± 6 nm for imaging and/or projecting a stimulus, and 940 ± 5 nm for wavefront sensing. The beams are collimated and coaligned as they enter the system with the initial beam splitter, then scanned into a 512 line raster pattern with a 16 kHz resonant fast scanner (SC-30, EOPC, Ridgewood, USA) to scan lines and a galvanometer slow scanner (6210h, Cambridge Technology, Bedford, USA) to scan each frame covering a field size of ~1 degree at 30 Hz frame rate. The light reflected by the retina is descanned and redirected according to wavelength. The light collected in the 940 nm channel is guided into a wavefront sensor to measure the ocular wavefront and drives the deformable mirror (DM97-08, ALPAO, Montbonnot-Saint-Martin, France) to correct for the measured aberrations. The imaging light is collected by individual photomultiplier tubes for each imaging channel and digitized with a field programmable gate array (FPGA). Each video frame is digitized into 512 X 512 pixels. Because the eye motion measurements are done on a strip based cross-correlation, and each frame is broken up into 32 strips, the computation to extract the real-time eye motion trace using the FPGA is reported at 960 Hz with a 2.5 millisecond latency till the AOOCT tip tilt mirror corrects from the eye motion (Sheehy et al., 2012; Stevenson et al., 2010; Stevenson & Roorda, 2005; Vienola et al., 2012).

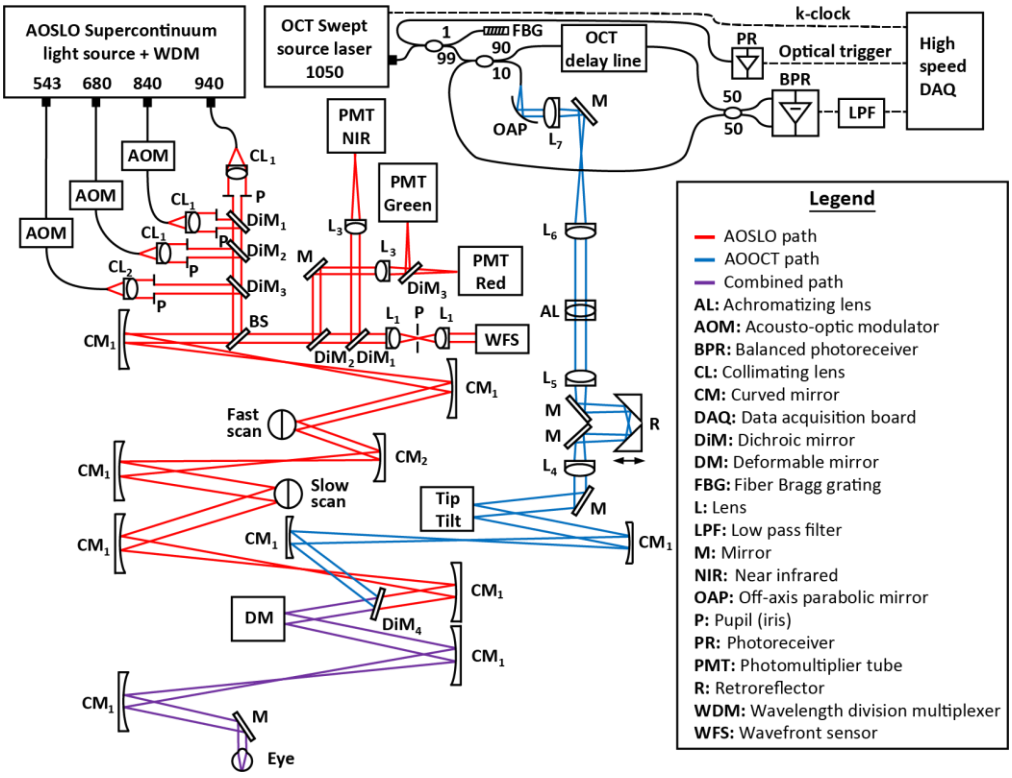

Figure 4.1: The system schematic is depicted here with the red path corresponding to the AOSLO, the blue path shows the AOOCT and green depicts where these two beams are combined with a dichroic mirror. Within the AOSLO path we can appreciate the three imaging channels and the WFS channel with the independent delivery and collection. In the AOOCT path the main components consist of the achromatizing lens, the focus adjustment, and the active scanning mirror.

4.3.2 AOOCT System Design

The AOOCT uses a 100 kHz swept source laser (Axsun Inc, Billerica Massachusetts, USA) with a center wavelength of 1040 nm and bandwidth of 106 nm resulting in an axial resolution of 6.5 um in air. The k-clock signal produced by the laser was used to acquire linear-in-wavenumber interferograms avoiding the need for post-processing linearization. A fiber Bragg grating was used to reflect a thin linewidth at the beginning of the sweep which was detected by a photodiode and used as an A-line trigger, enabling phase stable measurements. The beam diameter at the cornea is adjustable based on the light delivery telescope, for this study the beam diameter was set to 7.2 mm in the pupil plane resulting in lateral point spread function of 0.61 arcminutes (distance from the peak of the Airy pattern to the first dark ring) which corresponds to about 3 microns assuming that the retinal magnification factor is 300 microns per degree of visual angle.

The system optical schematic of the AOOCT is shown in Figure 4.1 as blue rays. The light source is coupled into the system with a single mode fiber to a 4 mm reflective collimator using an off axis parabolic mirror. Upon entering the system, the beam enters the light delivery telescope - Lens 7 and Lens 6 - which controls the AOOCT beam size on the achromatizing lens. The achromatizing lens is a custom optic which corrects for the longitudinal chromatic aberrations in the human eye across the wavelength range of the source to obtain a sharper point on the retina. The next telescope pair - Lens 5 and Lens 4 - controls both the focus adjustment and the beam size

on the 2 axis scanner. The distance between these two lenses allows for an independent focus control by adjusting the motorized stage in software to control the change in focus. The beam is then relayed onto a dual-axis MEMS bonded mirror (Mirrorcle, Richmond, CA) which is controlled with two superimposed driving signals, the line or volume scan and the eye motion stabilization signal for real time correction. Two curved mirrors are used to the relay the pupil of the AOOCT beam onto the deformable mirror and coaligned with the AOSLO optical path via a dichroic mirror. The OCT and SLO are both adaptive-optics corrected and coaligned in both the image and pupil plane to acquire from the same spatial location in the retina. The AOOCT beam is set to have a fixed offset in vergence to account for the longitudinal chromatic aberration of the eye with respect to the wavefront sensor wavelength. The according vergence is implemented to ensure the beams of both imaging systems focus at the same depth in the retina.

The reference arm length is designed to match the complete sample arm with a total length of 11.7 meters in free space, 104.8 mm of optical glass, and 5.4 m of fiber optic length. The reference arm consists of a series of 4-f telescopes which are optimized in length to avoid the coherence revival fringes and ensure the correct set of interference fringes are acquired by going through each set of fringes and measuring the phase stability in each coherence revival interference signal (Dhalla, Nankivil, & Izatt, 2012; Dhalla, Nankivil, Bustamante, et al., 2012). The reference arm power is aligned for maximum power throughput and an iris is used as a limiting aperture to decrease the reference arm power to avoid saturating the balanced detectors while still performing at the shot noise limit. The reference arm has a polarization controller which is used to optimally distribute the power in the two leads going to the balanced photodetector (BPD430c Thorlabs Inc).

To enable phase imaging, an optical trigger is implemented to sync with the Mach-Zehnder interferometer (MZI). A 99 to 1 fiber beam splitter is used to send 1 percent of the light into a Fiber Bragg grating (Center wavelength 992 nm and bandwidth of 0.1 nm) and send the reflection back into the opposing fiber beam splitter lead to be coupled into a photodetector. The signal from photodetector is amplified and used as the A-scan trigger optically synced to the MZI signal to the spectral sweep. The temporal delay between the interference signal and the MZI signal is matched by accounting for the fiber length, free space path length and the detector delay and the cable length delay to propagate the signal to the digitizer (ATS9350 AlazarTech, Pointe Claire, Canada).

4.3.3 Syncing AOSLO and AOOCT

The AOSLO has two main synchronizing signals, the horizontal-sync (H-sync) and the vertical-sync (V-sync) as depicted in Figure 4.2. The H-sync is a TTL signal at ~16 kHz generated by the resonant scanner driver and is the main clock of the AOSLO. The V-sync is generated based off the H-sync and sets each new frame at $1/512^{th}$ of the line scan rate.

The two fundamental timing signals in our system are the pulse from the 15.48 kHz resonant scanner in the AOSLO (H-sync) and the optical trigger generated by the FBG in the AOOCT. The H-sync is sampled every 512 pulses to create a V-sync (frequency 31.25 Hz) that determines the start of an AOSLO frame. The frame trigger for the AOOCT system is generated from a four-fold multiple of V-sync, equivalent to 121 Hz.

The AOOCT has three main electronic signals, the k-clock, the sweep trigger, and the frame trigger. The swept source laser has a 100 kHz sweep rate and is determined using an optical trigger. Since the laser does not sweep linearly in wavenumber, an MZI samples the sweep producing an interferometric signal whose zero-crossing are evenly spaced in wavenumber. This signal (k-clock) is fed to the digitizer to sample the AOOCT signal linearly in k-space. The k-clock frequency is set as such to provide an imaging depth of 5 mm. The AOSLO and AOOCT is synced with the AOSLO frame trigger at 30 Hz such that each AOSLO frame corresponds to 3300 A-scans of the AOOCT which can be distributed to a volume or line by the 2-D MEMS. The two main AOOCT protocols consist of (a) a volume acquisition which distributes the scan over a field size for an 8-second acquisition, oversampling in lateral directions to increase SNR and (b) continuous B-scan acquisition which spatially locks onto a line of cells to optimize for the temporal sampling rate to 121 Hz.

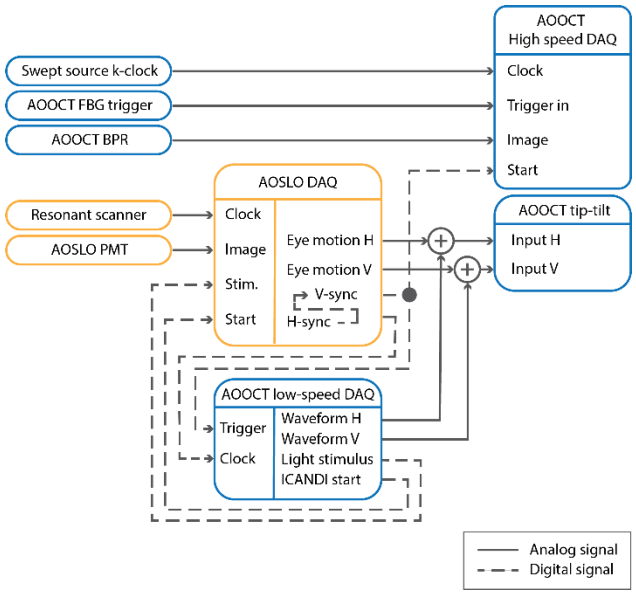

Figure 4.2: The schematic above displays how the sync signals are integrated between the AOSLO and AOOCT. The main clocks originate from the resonance frequency of the AOSLO resonant scanner (H-sync) and the start of the AOOCT laser sweep as detected by the fiber Bragg grating (AOOCT FBG trigger). DAQ data acquisition board, PMT photomultiplier tube, H horizontal, V vertical.

4.3.4 Active Motion Correction

The image stabilization software, Image Capture and Delivery Interface (ICANDI) is a custom program which can extract the eye motion from an AOSLO image for real-time correction implementation as previously described in Arathorn et al and Stevenson et al (Arathorn et al., 2007, 2013; Sheehy et al., 2015; Stevenson et al., 2010). Recent developments of this software enable loading a previously acquired AOSLO image as a reference frame to be used over multiple imaging session across weeks. The process begins by acquiring an AOSLO video of a particular retinal location, correcting each frame in the video for eye motion, and summing each frame for a high-signal-to-noise, relatively distortion-reduced AOSLO image, and loading into ICANDI as a reference frame. The incoming frames are then broken down into strips which are cross-correlated with respect to the reference frame strips. The horizontal and vertical displacements of each strip are then used as the correction signal. The eye motion is reported at 960 Hz, converted to appropriately-scaled analog signals (see next paragraph), and added to the AOOCT scanner signals

before sending them to the MEMS mirror. This methodology has been previously shown and characterized by Sheehy et al. and Vienola et al. (Sheehy et al., 2015; Vienola et al., 2012).

The eye motion trace output can be modified in gain and angle in the ICANDI software to account for the scanner variance in driver voltage and alignment in scan orientation. These gain and angle corrections were experimentally found using a moving model eye setup which consisted of a lens focusing onto a structured sample while traversing a galvo scanner in the path to simulate eye motion. The motion correction was activated to stabilize the moving model eye and the gain was systematically optimized to find minimal residual motion by visualizing the focus spot on a camera.

4.3.5 AOOCT Focus Adjustment

The focus of the AOOCT channel can be adjusted to focus on selected retinal layers while the AOSLO beam holds its focus on the high contrast textured photoreceptor mosaic which helps to maintain a high-quality motion correction. To achieve this, a set of fold mirrors are mounted to a motorized stage in the 4f telescope of the AOOCT path relaying the light from the achromatizing lens to the MEMS scanner. The focal plane is adjusted through adjustment of the distance between these lenses. A second motorized stage is added in the reference arm to simultaneously move with the sample arm to match the optical path.

4.3.6 AOOCT Data Processing

The standard OCT data processing pipeline consists of removing the background, removing the system interference artifacts, and shaping the spectrum. Additional ophthalmic OCT data processing includes applying a chromatic dispersion curve, axial alignment, flattening the image in depth, and linearizing the image along the fast axis. The dispersion correction is calibrated for each subject based on applying quadratic dispersion curves. The eye motion correction begins with the axial motion, a centroiding algorithm determines the centroid with respect to depth for the B-scan image and consecutive B-scans are shifted to align the signal axially. The images are then flattened to account for the curvature of the retina; the B-scan is segmented axially to determine the curvature based on the ISOS junction and the image is then warped to fit this line on a single plane in depth. The last processing step is linearizing the B-scan to account for the non-linear MEMS sweep. A linearization curve is obtained by imaging a calibration grid and it is used to resample the B-scans along the fast axis accordingly.

The main advantage in the active eye motion correction is that the volumes require no additional lateral registration to localize a series of photoreceptors, especially in comparison to standard ophthalmic AOOCT. As is shown in Figure 4.7 in the results, further lateral registration can be done using a cross correlation method on the images to improve the B-scan average image. Additionally, by using the same AOSLO reference to spatially target retinal locations over the entire imaging session, this enables the series of 20-30 volumes acquired within an imaging session to be averaged with no additional lateral registration necessary.

4.3.7 Human Subject Imaging

The University of California Berkeley Institutional Review Board approved this research, and subjects signed an informed consent before participation. All experimental procedures adhered to the tenets of the Declaration of Helsinki. Mydriasis and cycloplegia were achieved with 1% tropicamide and 2.5% phenylephrine ophthalmic solutions before each experimental session. The subject bit into a dental impression mount affixed to an XYZ stage to hold the eye and head still. The subject was a healthy young adult volunteer, 20112L.

4.4 Results

4.4.1 Quantifying residual motion of stabilization with a moving model eye

A moving model eye setup, consisting of a galvo scanner between a lens and a paper with two crosshairs of tape on the surface, was utilized in characterizing the stabilization precision. In order to account for the LCA offset between the AOSLO and AOOCT resulting in different focal positions, a dichroic mirror was inserted in the model eye to reflect the AOSLO wavelengths onto a separate sample of paper such that the AOSLO had a strong signal for tracking while the AOOCT had a sharp focus on the tape layers. Here, we quantified the active stabilization performance with different amplitudes and frequencies of motion. The moving model eye is driven to replicate the eye motion spectrum (Vienola et al., 2012) by stepping through frequencies while adjusting the amplitude accordingly to match the velocity. The residual motion is calculated by comparing the lateral pixel shifts in the AOOCT data with and without a motion-correction. Results are shown in Figure 4.3 and Figure 4.4.

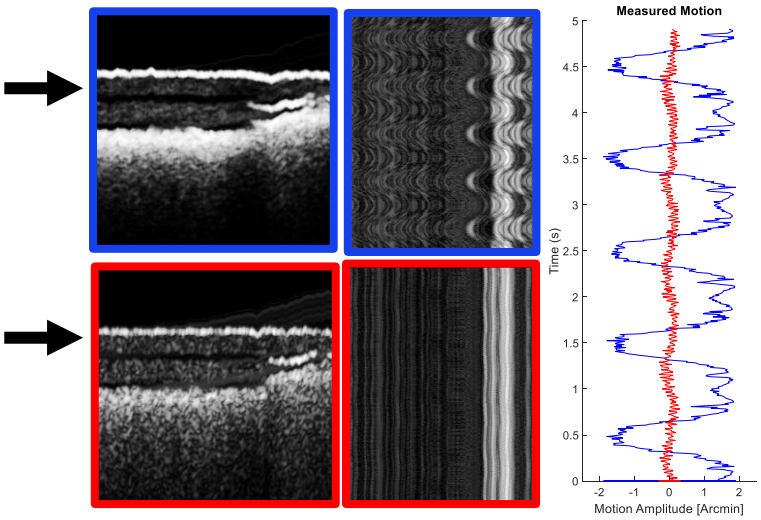

Figure 4.3: The images on the left show the average B-scan image over a 5 second acquisition; the right images are a time trace of the signal acquired from the depth depicted by the black arrow. The top panel and blue trace reveals the 1Hz sine wave with a 3.8 arcmin amplitude motion applied via the moving model eye. The lower panels and red trace show images and time sequences with active motion correction.

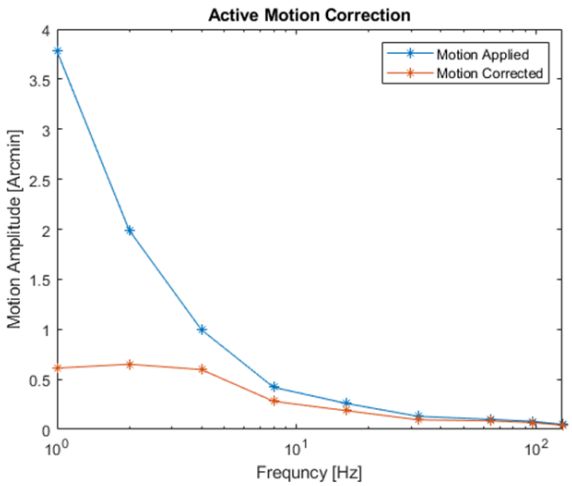

Figure 4.4: Motion reduction through active motion-correction. The amplitude of sinusoidal motion in a model eye without and with active correction are shown in blue and orange traces respectively.

For a better visual sense of the active eye motion correction, in Figure 4.3 we can appreciate the averaged B-scan image shows the accumulation of blur from the motion compared to the crisp image produced with the active motion correction. Figure 4.4 shows that active eye motion correction works for all frequencies and that we can therefore compensate for majority of the eye motion spectrum, particularly the larger amplitude motion at lower frequencies.

4.4.2 Human imaging with actively stabilized AOOCT

To get a spatial reference to the imaging location of interest, both a clinical fundus image and an AOSLO montage was acquired in the subject 20112 left eye as shown in Figure 4.5. The individual AOSLO images were stitched together from the fovea to the temporal 12 degree. A 1-degree field of view is shown at the fovea in the black border and at 12 degree in the white border. When the fundus and the montage are integrated together, we can appreciate the difference in scale and how the two compliment another especially as the vasculature of the fundus lines up with the AOSLO montage. The AOOCT photoreceptor images were collected at about 7 degrees while the superficial nerve fiber layer images were taken at 12 degrees.

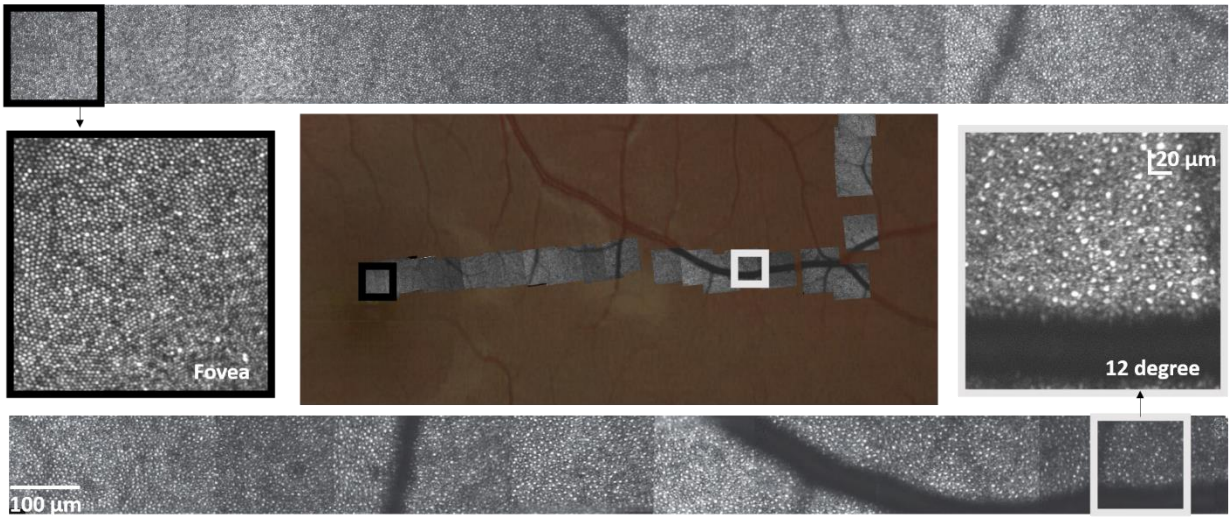

Figure 4.5: An AOSLO montage from the fovea to 12 degrees eccentricity was made as a reference to indicate the location the AOOCT results.

Figure 4.6 shows an enface images of a human photoreceptor mosaic (en face view of the inner segment outer segment (ISOS) junction) acquired over 8 seconds acquisition without and with active stabilization. Without motion correction, AOOCT volumes need to be post-processed, whereas raw actively stabilized AOOCT volumes can be directly projected to reveal a high fidelity image of the photoreceptor mosaic. Although the active-motion-corrected volume shows a few line artifacts from high velocity motion, the majority of the eye motion is actively corrected, and the photoreceptor mosaic can be easily distinguished. Our system, therefore, enables the raw acquisition of a photoreceptor mosaic within a single volume with only bulk axial registration and no need for prior reference OCT frame. To further increase the signal to noise ratio, repeated acquisitions can be easily averaged since no lateral registration is required.

Using the actively stabilized AOOCT, the motion correction no longer requires a volume for registration and a B-scan can be spatially locked on a series of photoreceptors. In Figure 4.6 we can see the challenge which AOOCT faces with eye motion while trying to maintain a fixed B-scan on the retina. The top panel shows an averaged B-scan in which the details wash out due to the motion, the time trace of the ISOS junction shows sections of minimal eye motion either in lateral drift or saccades, but due to the eye motion the retinal location of the B-scan is not maintained. In the lower panel of Figure 4.6 the active stabilization is activated, and the individual photoreceptors are clearly visible in the averaged B-scan over 1000 frames. The time trace of the ISOS is shown in the bottom right image of Figure 4.6, where we can appreciate that the majority of the motion is corrected; although two high velocity saccades are evident, the tracking does recover and return the B-scan onto the same retinal location.

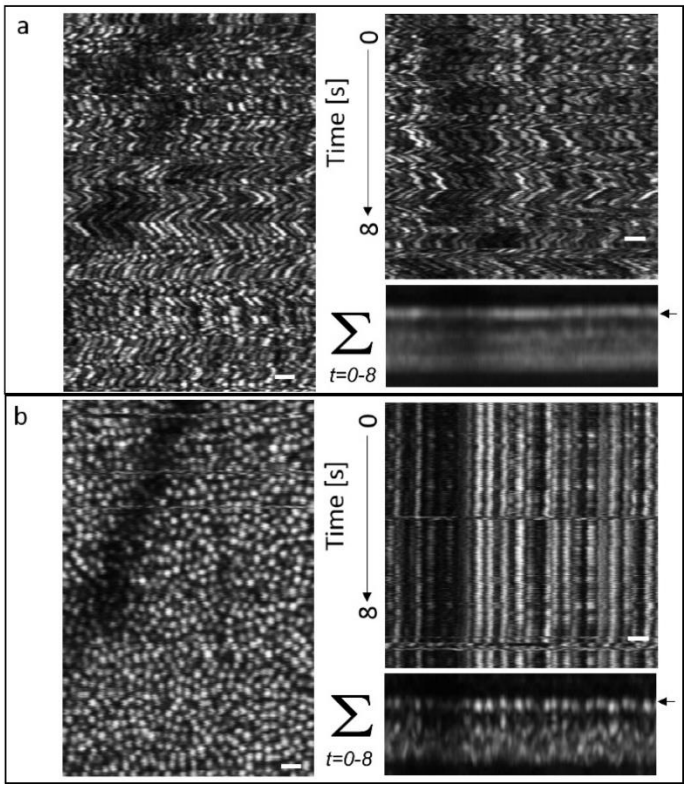

Figure 4.6: An 8-second AOOCT acquisitions without tracking (upper row) and with active tracking (lower row). The left column displays an en face view of the IS/OS junction from a C-scan, and the right column shows a time trace of B-scans of the IS/OS junction. A registered sum of the B-scan is shown below each time trace. Without tracking, the en face image is distorted and the B-scan continuously shifts to different locations. Active stabilization yields high fidelity en face views with no need for post-processing and consistent B-scans from a single location which, after averaging reveals a cross-section with resolved cones. Scale bar: 20 μm.

The main take away from Figure 4.7 is that the lateral registration is not necessary to localize photoreceptors. The B-scan average can be incrementally improved with post processing lateral registration, however the photoreceptors can be easily tracked through the B-scan revealing a high resolution B-scan average image. The averaged image from the axial and lateral are slightly enhanced, but both images are comparable.

The use of a single, high quality AOSLO retinal reference allows us to revisit and probe the same retinal location for multiple imaging sessions. Taking advantage of these developments, we look at different retinal planes by independently adjusting the AOOCT focus while maintaining a lock on the same series of photoreceptors as shown in Figure 4.8. In this series of images, the retinal location is fixed in the AOSLO while the focus changes in the AOOCT from the photoreceptors to the nerve fiber layer shown in both linear image scale to appreciate the photoreceptor signal and logarithmic image scale to the appreciate the weaker signals. Although the change in focus changes the image structure immensely, the blood vessel in the top right of all these images shows a clear shadow on the underlying layers and is evident in all these images.

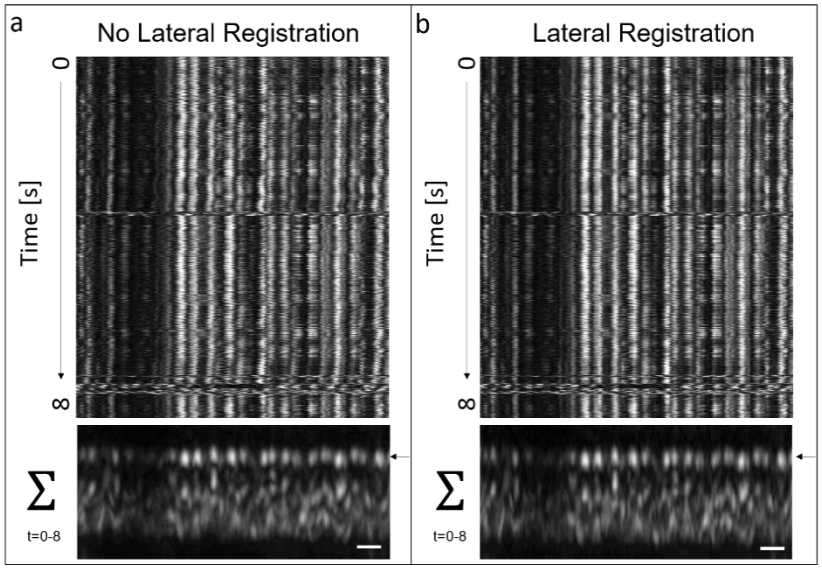

Figure 4.7: This figure compares only the active stabilization lateral registration to a post processed image with lateral registration. The top images show the time trace of the ISOS junction in a fixed B-scan protocol over an 8 second acquisition; the bottom images show an average of the B-scan over the 8 second acquisition. Scale bar: 20 μm

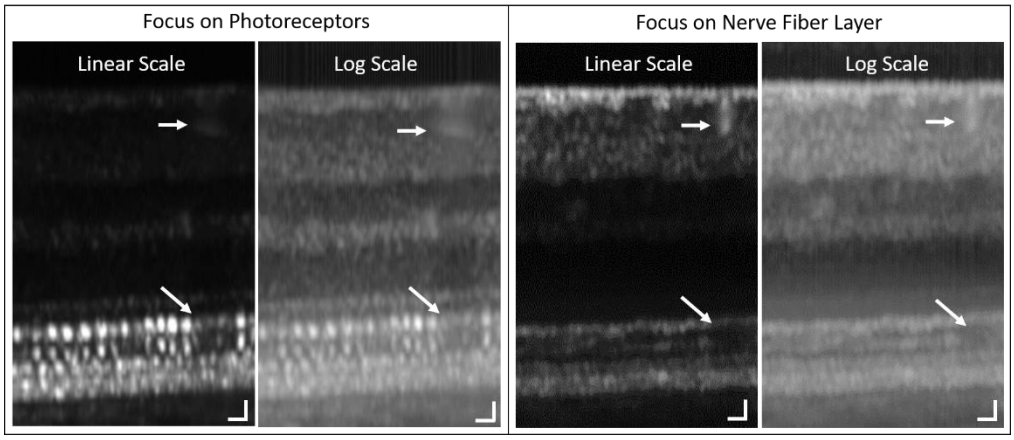

Figure 4.8: Actively stabilized B-scan images of the same retinal location. Left images are in linear scale and right images are in logarithmic scale. The left pair of images show an average B-scan with the AOOCT focus on the ISOS junction of the photoreceptors while the right pair of images show an average B-scan with the focus on the nerve fiber layer. Arrows point to a capillary vessel in the superficial retina and its shadow on the photoreceptors. Scale bar: 20 μm

When all the features in this system are combined, the active stabilized AOOCT can collect volumes of targeted structures in low reflective retinal regions and these volumes can be averaged in time without lateral registration. When these volumes are averaged and sliced in different depths, the high-fidelity volumes shed light on distinct features shown in Figure 4.9. The coarse depth sectioning of this volume shows the spatially distinct structures while the finer depth sectioning shows the smaller details. The different layers of vasculature can be appreciated in the

coarser depth sections along with the strong signal from the individual nerve fibers. Although a mosaic of ganglion cells is not distinctly apparent, the finer slices reveal similar structures in which a few cells can be spotted. Overall, the thicker structures can be followed through a series of the finer slices, while smaller structures disappear between the individual slices.

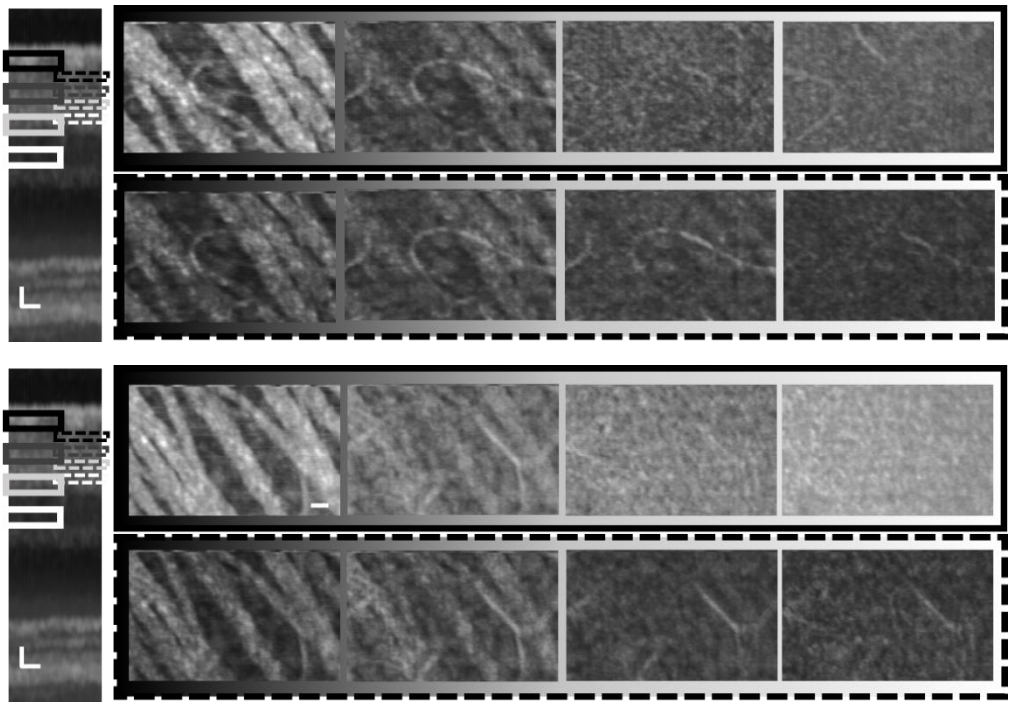

Figure 4.9: The top series is comprised of 18 volumes and the bottom series from 23 volumes, two spatially adjacent locations both at 12 degrees eccentricity. Within each data set, the top series (outlined with solid lines) shows coarse depth sectioning with 6 μm steps wherein each independent layer is integrated over 4 μm. The lower panel outlined with the dashed lines depicts the finer depth sectioning with 2.5 μm steps integrated over 1.2 μm with thicker structures overlapping through the frames. Scale bar: 20 μm

4.5 Discussion

In this chapter we demonstrate active eye motion correction for an AOOCT system that can reveal the photoreceptor mosaic without additional lateral motion registration, enabling fixed line imaging at a chosen retinal location. These characteristics facilitate a high throughput of high-quality data that need minimal postprocessing. The ability to change the AOOCT focus independently allowed acquiring high SNR AOOCT measurements from different retinal layers, while maintaining high fidelity AOSLO-based eye motion correction from the feature-rich en face video of the photoreceptors.

We were able to quantify the motion correction accuracy with a moving model eye setup in which a galvo scanner induced both horizontal and vertical motion. By measuring the residual motion after stabilization, we were able to calculate the accuracy of the motion correction as a percentage of the applied motion. Considering the eye motion frequency spectrum along with the amplitude of eye motion, we can confidently correct for most of the eye motion with limitations in high frequency and faster velocities correlating to large microsaccades.

Active tracking enables AOOCT recording to employ a fixed line acquisition protocol as it efficiently targets a particular spatial location reliably and does not require a volume for spatial

registration. The fixed line scan protocol with active tracking removes the need for large volume acquisitions and reduces the complexity in post processing. The spatially bound acquisition facilitates the probing of a particular series of cones by increasing the effective temporal sample rate of a particular region without a volume acquisition potentially increasing the effective frame rate to the line acquisition rate.

The fact that the AOOCT images show sharp images of photoreceptors and the nerve fiber layer give us confidence in the quality of the AO correction. However, we were not able to replicate retinal ganglion cell mosaics as clear as other groups have shown(Kurokawa et al., 2020; Liu et al., 2017, 2018). There are two likely reasons for this. First, the resolution is fundamentally worse because of increased diffraction from our AOOCT wavelength of 1050 nm compared to the 790 nm wavelength used in the other published reports(Liu et al., 2017). Second, the scattering and consequent intrinsic contrast of the ganglion cells is likely less for the longer wavelengths we chose to use.

The main limitation the system's current AOOCT framerate is the tip tilt mirror which serves two purposes, one to correct for eye motion in real time and the second to acquire a volume or line scan. To increase the effective frame rate, a galvanometer could be added in series with the current MEMs to increase the effective frame rate with the faster scan and the MEMs would only correct for the eye motion which is a lower frequency range.

Overall, we successfully implemented active eye motion correction for an AOOCT with 3-dimensional focus adjustment and spatial targeting as a platform for creating a more systematic approach from targeting a particular ensemble of cones for color vision experiments to clinical imaging for diagnostic purposes. This technology pushes the envelope of the high-resolution tracking with adaptive optics and real-time stabilization for an adaptive optics system; we successfully compensated for the eye motion and confidently probed targeted photoreceptors with a fixed B-scan acquisition protocol.

4.6 Conclusions

We were able to successfully enable active eye motion correction for AOOCT to stabilize the high amplitude and low frequency drifts of the eye. We showed the acquisition of an AOSLO video alongside a fixed location on the retina AOOCT video in the human retina with a 7.2 mm beam diameter. Although the motion compensation steadily decreased in the performance with the higher frequency movement, most of the eye motion was compensated in real time enabling high fidelity and stable AOOCT acquisition of specific spatial locations. Overall, this technology facilitates AOOCT imaging by creating a framework with a spatial retinal map to a location of interest and by mitigating eye movements to stabilize the functional probe on the targeted photoreceptors to compliment clinical microperimetry and psychophysical experiments.

Funding

National Institutes of Health (National Eye Institute) (T32EY007043, R01EY023591, U01EY025501, P30-EY003176), Alcon Research Investigator Award, Minnie Flaura Turner Memorial Fund for Impaired Vision Research, Soroptimist International Founders Region Fellowship.

Disclosures

AR:USPTO #7,118,216, "Method and apparatus for using AO in a scanning laser ophthalmoscope" and USPTO #6,890,076, "Method and apparatus for using AO in a scanning laser ophthalmoscope". These patents are assigned to both the University of Rochester and the University of Houston and are currently licensed to Boston Micromachines Corporation in Cambridge, Massachusetts. Both AR and the company may benefit financially from the publication of this research.

This paper is a work in progress presented as a Poster at ARVO, but yet to be published. The theoretical optical design of the AOOCT paper was done by Francesco LaRocca. The OCT MZI and system computer and OCT infrastructure was supported by Patrick Gregory, Hyle Park and Fabio Feroldi. The software and the code for half of the analysis was written and developed by Fabio Feroldi. The electronic implementation and testing was supported by Pavan Tiruveedhula and Austin Roorda. The AOOCT and AOSLO building, aligning, implementation, image analysis, subject and the writing of the paper was done by Sanam Mozaffari.

Chapter 5. Optoretinography with actively stabilized AOOCT

5.1 Abstract: Optoretinography is a recently developed technique that uses light-based measurements to reveal neural activity. Adaptive optics optical coherence tomography (AOOCT) records an optoretinogram by resolving individual photoreceptors and recording their physical elongation in response to light stimuli. The main difficulty in recording these nanometer-scale changes in an optoretinogram is constant eye motion. Typically, fast volume acquisitions are required for spatial registration to compensate the effect of eye motion. Here, we present a solution whereby an adaptive optics scanning light ophthalmoscope (AOSLO) is used to measure the eye motion and actively stabilize the AOOCT beam to compensate for eye motion in real time.

5.2 Introduction

Studying the neural activity within the retina is foundational to understanding how the organ functions, both for basic science in research and for diagnostics from a clinical point of view. Electroretinography (ERG) is currently the main clinical tool used to study the activity of retinal neurons in vivo. ERG measures the electrical response by flashing a stimulus and recording the electrical potential with an electrode placed on the cornea. ERG has good sensitivity toneuronal function of an aggregate of neurons, but the signal is not spatially specific and therefore it is impossible to infer information about individual neurons. On the other hand, multielectrode arrays (MEA) allow to resolve the signals from individual neurons by triangulation of the electrical activity measured across the retina with tens or hundreds of electrodes. MEAs have good spatial resolution and sensitivity, but they are invasive as they must be installed directly on the retina and are therefore not applicable for humans. Fluorescent markers which include proteins which fluoresce during neural activity are common electrophysiology tools in animal studies; however, these fluorophores are invasive and potentially toxic and are therefore inapplicable (and not approved) for human studies. Optoretinography was proposed in the early 1990s as a non-invasive solution to the limitations of electromagnetic methods(Mulligan & Macleod, 1994). Instead of an electrode, an optical probe can be used to measure with high spatial and temporal accuracy physiological signals from the human retinal neurons, while maintaining minimal invasiveness.

Over the past few years, optical coherence tomography (OCT) has attracted interest as a modality that allows measuring the functional response of retinal neurons by measuring the change in path length that light experiences while propagating through the retina(Azimipour, Migacz, et al., 2019; Hillmann et al., 2016; Jonnal et al., 2007, 2012; Kocaoglu et al., 2014; Pandiyan et al., 2020). Since OCT is based on interferometry, it fundamentally measures the complex electrical field of the light wave. This characteristic allows to measure both the amplitude and the phase of the waves backscattered by the sample. The amplitude component is used to reconstruct the tomogram (also called the intensity image), while the phase component allows to obtain several other kinds of contrast, notably blood flow, birefringence and strain(Chen & Wang, 2017; de Boer et al., 2017; Larin & Sampson, 2017). Through phase measurements, OCT can track changes in path length in the order of nanometers, its sensitivity scaling with signal-to-noise ratio (SNR)(Park et al., 2005; Yazdanfar et al., 2005). When light stimulates the retina, the photoreceptors react by initiating a signal cascade that eventually reaches the visual cortex. The cells which are responsive to light, the cone photoreceptors are known to modify their conformation, in turn changing their reflectivity profile and their optical path length (OPL). The OPL change occurs between the inner segment outer segment (ISOS) junction and the cone outer segment tip (COST) effectively representing the cone outer segment length which has a time profile proportional to the relative

light dose and photoreceptor spectral sensitivity(Zawadzki et al., 2005; Zhang et al., 2019). It has been recently shown that there is a short time scale response in which the OPL contracts for a few milliseconds from the stimulus onset, followed by a second phase in which the OPL increases several hundreds of nanometers over a few seconds (Pandiyan et al., 2020). The magnitude of the OPL change in response to a light stimulus reveals the cone phenotype, in turn enabling mapping of the trichromatic mosaic(Miller et al., 2003; Zhang et al., 2019).

To this end, adaptive optics (AO) technology has been a popular choice because it compensates for the eye's aberrations allowing to obtain a near diffraction-limited point-spread-function and resolve individual photoreceptors in OCT (AOOCT)(Merino et al., 2006; Torti et al., 2009). AO for ophthalmic imaging was pioneered in the late '90s beginning with fundus imaging(Liang et al., 1997) and has since become the technology of choice for the study of the retina in high detail, mainly through adaptive optics scanning light ophthalmoscopy (AOSLO)(Roorda et al., 2002). AOOCT has been combined with AOSLO to exploit the peculiar characteristics of each technology in terms of contrast (Azimipour, Jonnal, et al., 2019; Azimipour, Migacz, et al., 2018; Merino et al., 2006; Zawadzki et al., 2011). Conventional scanning light ophthalmoscopy (SLO) has been used for tracking and compensating for retinal motion in real time by applying an angular shift to an OCT beam to obtain motion artifacts-devoid OCT tomograms and angiograms(Braaf et al., 2013; Vienola et al., 2012). Similar technology is now available in commercial ophthalmic OCT systems (e.g. Spectralis, Heidelberg Engineering GmbH) although a slower tracking rates.

In order to correct for the eye motion successfully, the tracking signal needs to be high resolution with good stability or else the motion correction will inherently introduce artifacts and increase the underlying phase noise floor (Sheehy et al., 2015). With this consideration, AOSLO becomes a particularly unique platform with real time tracking accuracy within 0.12 arcseconds AO retinal tracking(Sheehy et al., 2015) compared to the SLO at 0.33 arcseconds SLO tracking(Braaf et al., 2011, 2013; Sheehy et al., 2012; Vienola et al., 2012).Here, we propose the use of AOSLO as a highly accurate eye tracker to compensate the eye motion in real time, allowing to stabilize an AOOCT beam on the retina and obtain repeated measurements from a targeted retinal locations over a large time scale.

In this chapter, we show that by actively stabilizing an AOOCT probe using an AOSLO for high fidelity retinal tracking, we can measure optoretinograms from a targeted location repeatedly within imaging sessions and eliminate the need for volume registration in postprocessing. The motion stabilized interferograms yield a high throughput of valuable data, significantly reducing the complexity of post processing registration. We show that we can obtain phase resolved AOOCT scans and that we can follow the evolution of the cones path length at a rate of 121 Hz over 8 seconds.

5.3 Methods

5.3.1 AOOCT + AOSLO System design

The system is a combination of two independent setups that are optically combined with a dichroic mirror and electronically synchronized by mutually interlaced timing signals (see Figure 5.1). The AOSLO system was extensively in Chapters 2 and 3(Mozaffari et al., 2018, 2020) and thus only the related details will be described here. In brief, light from a supercontinuum source (NKT Photonics, Birkerød, Denmark) is split in two narrow band infrared channels that are used for imaging and wavefront detection. A 16 kHz resonant scanner (SC-30, EOPC, Ridgewood, USA) and a galvanometer scanner (6210h, Cambridge Technology, Bedford, USA) create a raster scan on the retina. The descanned light is detected by a photomultiplier tube (Hamamatsu, San Jose, USA) whose signal is digitized to make a 512x512 image over an area of 1°x1° at a frame rate of 30 Hz. The wavefront is obtained with a Shack-Hartmann wavefront sensor, which operates at 30 Hz. The measured wavefront is decomposed in Zernike polynomials in real time and a deformable mirror (DM97-08, ALPAO, Montbonnot-Saint-Martin, France) takes the shape of the distorted wavefront to correct for the eye's aberrations.

The AOOCT system is based on swept source OCT technology(Yun et al., 2003), where the eye is illuminated with a very narrow band of light rapidly scanned over a large range of wavelengths. The interference pattern that is obtained contains information over the depth and amplitude of the backscattering events in the eye, relative to a reference arm. The depth scan is obtained by a Fourier transform of the measured interferogram.

The core of the interferometer is fiber based but large parts of the arms are based on bulk components. A 99/1 coupler directs 1% of the light from a swept source engine (Axsun Inc, Billerica Massachusetts, USA) to a fiber Bragg grating (FBG, O/E Land, Canada) which reflects a narrow light band at the beginning of the sweep. An avalanche photodiode (APD10A2, Thorlabs Inc, Newton NJ) detects the reflection and the amplified rising edge of the voltage is used as an optical trigger for the data acquisition card. Since the FBG reflects a fixed linewidth, each interferogram will be synchronized in wavenumber space even in presence of inter-sweep variations. This scheme is a common solution to the phase-jitter problem caused by swept sources that run in open loop. The laser has a built-in Mach-Zehnder interferometer (MZI) with a fixed OPL difference which creates an oscillatory signal that is used as a k-clock to linearize the mapping of the acquired samples in wavenumber space. The laser has a central wavelength of 1040 nm, 100 nm of bandwidth and a sweep rate of 100 kHz.

The rest of the light is split by a 90/10 coupler where 10 % of the radiation is directed to the sample arm while 90% to the reference arm. Similar configurations are commonly used to maximize the collection efficiency of the sample arm while respecting the light dose exposure limit to the eye. An off-axis parabolic mirror (RC04APC-F01, Thorlabs Inc, Newton NJ) collimates the light exiting the fiber in the sample arm, which then passes through a 1:2 telescope to create an 8 mm diameter collimated beam. Given the large bandwidth of the OCT radiation, a custom achromatizing lens was designed to compensate for the eye's longitudinal chromatic aberration (LCA). A Badal telescope allows to change the beam vergence to adapt to the eye refractive error without changing the magnification of the beam. Moreover, the Badal optometer is used to compensate the LCA relative to the AOSLO beam, allowing to match the focal depth of all beams. The AOOCT light is directed to a 2D MEMS-based mirror (Mirrorcle, Richmond, CA,

USA), which has a diameter of 7.5 mm and a bandwidth of 500 Hz over a scanning angle of ±1°. The mirror is on a plane conjugate to the eye pupil and has two functions: creating a line or raster scanning pattern and steering the beam to counter the retinal motion. The AOOCT optical path is superimposed to the AOSLO path by a dichroic mirror. The joined beams reach the deformable mirror, which lies on a pupil's conjugate plane, to correct for the eye's aberrations.

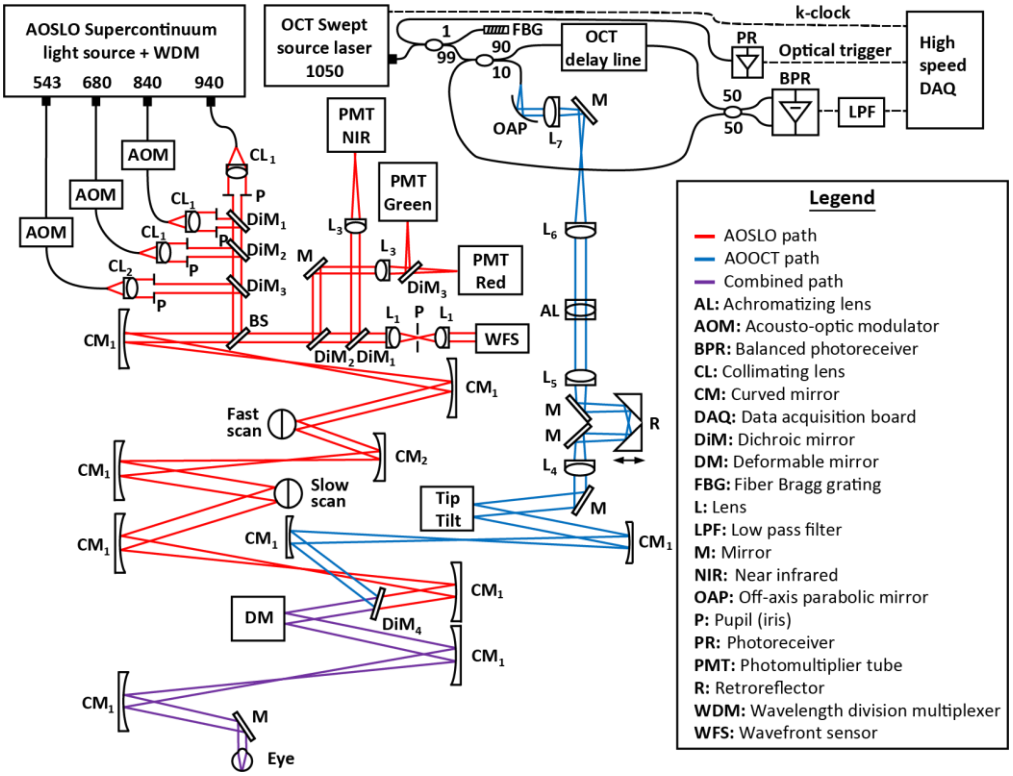

Figure 5.1: The system schematic of the combined AOSLO and AOOCT system with the red path indicating the AOSLO path, the blue referes to the AOOCT path, and purple refering to the combined beam path. The two beams are combined at the dichroic mirror before the deformable such that both systems benefit from the AO correction.

Several characteristics of the AOOCT system were measured by focusing the light on a mirror in lieu of the eye. A neutral density filter (measured attenuation factor $10^{2.7}$) was placed in the sample path to avoid saturating the photodetector. The polarization state of each arm was adjusted to maximize the SNR. Turning off the MEMS avoided the influence of motion on the mirror. We applied numerical dispersion compensation to the spectra to recover the maximal SNR and resolution(Cense et al., 2004). The axial resolution was measured as the FWHM of the point-spread-function of the interferometric measurement in linear scale. The sensitivity of the system was measured as the ratio between the peak of the interferometric signal and the average underlying noise floor as obtained with a background measurement. Using the formula for theoretical sensitivity of a swept source OCT system with known illumination power(Yun et al., 2003). The difference is expected to be caused by the non-ideal suppression of DC noise in the balanced detection scheme due to non-spectrally flat split ratio of the 50:50 fiber coupler.

The roll-off was measured by placing the model eye at several delays with uniform intervals. The obtained point spread functions were fitted using a second-degree polynomial and the curve was used to correct the intensity images. The phase sensitivity is a key feature of our system, so it had to be carefully determined. Following the work by Braaf et al.(Braaf et al., 2011, 2013), we separated the fundamental system phase noise from the contributions of the scanner. Given the considerable optical path length in air of our system (about 10 m), we used a coverslip as a sample to reference the phase measurement within the sample itself, reducing the influence of mechanical motion in the setup. For testing the influence of scanning we measured with two different conditions on the same scattering sample: a stationary beam and a scanning beam over different FOVs.

5.3.2 Phase Sensitivity with Active Motion Correction

We tested the ability of our eye tracker to compensate motion in real time by performing a set of experiments similar to those delineated by Braaf et al. (Braaf et al., 2012). We used a model eye that simulated motion using a galvo scanner actuated with a sinusoidal signal at different frequencies. First, we characterized the effective bandwidth of the MEMS scanner by driving one-dimensional sinusoidal motion over a large range of frequencies at constant amplitude. We determined the bandwidth as the frequency at which the scan amplitude falls by 3dB compared to the maximum.

5.3.3 Electronic Synchronization

The two systems run on two separate computers whose data acquisition cards (DAQ) are connected by timing signals that synchronize them, avoiding artifacts such as a rolling window on the images or the need of post-acquisition synchronization. The AOOCT system uses two DAQs: a high speed one (ATS9350, AlazarTech Inc. Pointe-Claire, Canada) that digitizes the OCT signal and a low speed one (National Instruments Inc, Austin, TX, USA) that creates the waveforms for the MEMS scanner and signals the start of an AOOCT acquisition. The AOSLO system uses a DAQ that digitizes the signal from the PMT and one that digitizes the SHWS signal.

The two fundamental timing signals in our system are the pulse from the 15.48 kHz resonant scanner in the AOSLO (H-sync) and the optical trigger generated by the FBG in the AOOCT. The H-sync is sampled every 512 pulses to create a V-sync (frequency 31.25 Hz) that determines the start of an AOSLO frame. The frame trigger for the AOOCT system is generated from a four-fold multiple of V-sync, equivalent to 121 Hz.

The high-speed DAQ in the AOOCT receives the k-clock needed to guarantee linear sampling in wavenumber space from an MZI installed in the swept source laser. The start of an AOOCT spectrum is signaled by the FBG optical trigger, while the voltage generated by the balanced receiver is low-pass filtered and digitized by one of the channels of the board.

The low-speed DAQ in the AOOCT uses the H-sync to generate two analog waveforms with the profiles needed to drive the 2D MEMS scanner and uses the V-sync to determine the start of a B-scan, effectively synchronizing the frames in the two systems. The waveforms for the scanner are combined with the eye motion correction signals retrieved by the AOSLO system using a summing amplifier. Finally, a single edge TTL pulse is generated by the board to signal the start of an AOOCT video acquisition to the AOSLO computer, which initiates logging of a sequence of AOSLO frames.

5.3.4 AOOCT Phase Data Processing

The standard OCT data processing pipeline was applied: background subtraction, chromatic dispersion compensation and zero padding. The axial bulk motion was compensated by registering all the frames to a reference frame. The main advantage of this system design is the elimination of complex lateral registration applied in postprocessing and guaranteed targeting of a particular location.

The OPL changes of each cone were obtained by multiplying the phasor at cone outer segment (COST) reflection with the complex conjugate of the phasor at the inner segment/outer segment junction (ISOS). The brightest reflection in the structural OCT intensity tomogram was selected to process the phase signal for both these indexes. The phase of these two pixels was monitored over time representing the OPL change in the cone outer segment thereby recording a physical elongation of the photoreceptor. During a control experiment, the OPL is constant for all photoreceptors while during a stimulus experiment the OPL expands a few hundred nanometers, proportionally to the stimulus intensity.

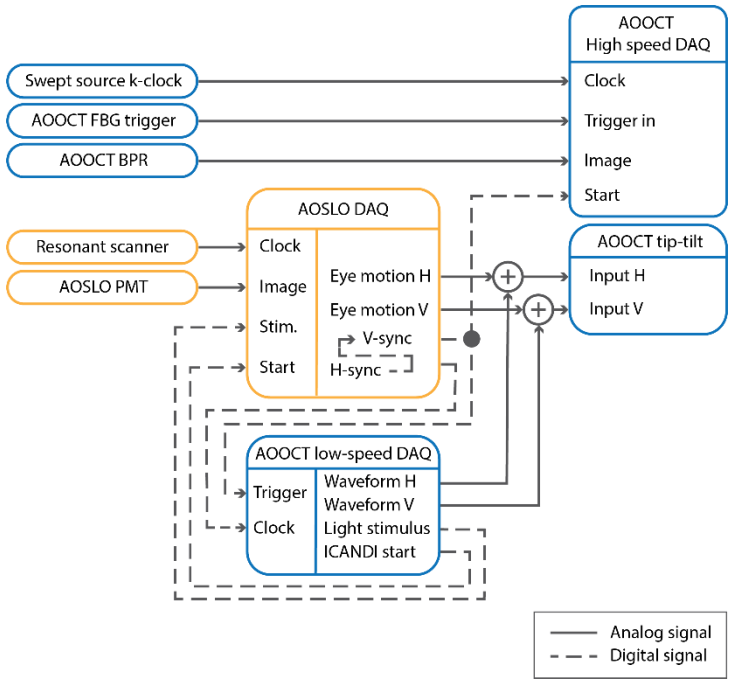

Figure 5.2 Wiring of the two systems. The blue boxes represent elements belonging to the AOOCT system while the yellow ones are the AOSLO items. The swept source laser sends the k-clock to the AOOCT high speed DAQ (AlazarTech). The reflection off the fiber Bragg grating (FBG) is used as a phase-stable A-line trigger. The AOOCT signal from the balanced photodetector (BPR) is registered by Image channel of the high speed DAQ. The optical sweep trigger obtained from the fiber Bragg grating is sent to the Trig In port of the DAQ, while the frame trigger is received by the Auxiliary port. The AOSLO DAQ uses the positioning signal from the resonant scanner to generate H-sync and frame trigger, while the signal from the PMT is used to create the image from which eye motion is extracted. The tip-tilt scanner of the AOOCT system receive the eye motion traces obtained by the AOSLO system combined with the scanning waveform generated by the low-speed DAQ. The low-speed AOOCT DAQ receives the H-sync and the frame trigger from the AOSLO system, which are used to create the waveforms, the ICANDI start, and light stimulus signal.

5.3.5 Imaging protocol

The University of California Berkeley Institutional Review Board approved this research, and subjects signed an informed consent form before participation. All experimental procedures adhered to the tenets of the Declaration of Helsinki. Mydriasis and cycloplegia were achieved with 1% tropicamide and 2.5% phenylephrine ophthalmic solutions before each experimental session. Subject bit into a dental impression mount affixed to an XYZ translation stage to align and stabilize the eye and head position. Both subjects (10003L, 20112L) were healthy adult volunteers. Structural imaging was implemented with the AOSLO using 543 nm and 680 nm for stimulus channels, 840 nm for structural imaging channel and 940 nm for WFS channel; and structural/functional imaging with the AOOCT at 1050 nm.

First, a reliable aberration correction was found and good image quality of the AOSLO images was obtained, then a series of frames was recorded. The frames were registered to remove motion and averaged, which resulted in a high-quality image that was used as a reference frame for eye tracking(Stevenson & Roorda, 2005). Then, the AOOCT beam was directed to the eye and the optical path length of the interferometer was matched by using the variable delay line in the reference arm. The interferometric artifacts in the AOOCT were minimized using a manual polarization controller placed in the reference arm. Once satisfactory image quality was found on both systems, eye tracking was turned on, using a previously acquired reference frame. Once stable motion correction was obtained, the user initiated the OCT acquisition which triggered the acquisition of an AOSLO sequence consisting of B-scans obtained from a single location. The stimulus had a duration of 100 ms and was presented after 1 second from the start of the AOOCT recording. The power level of the stimulus was varied according to the desired bleaching level. The total duration of each recording was 8 seconds, corresponding to 1000 AOOCT frames.

5.4 Results

The physiological response of the photoreceptors revealed an elongation of the cone outer segment in response to the stimulus. By quantifying the physiological changes, we were able to identify cones belonging to different spectral sub-classes, and we confirmed the result over datasets acquired repeatedly. In Figure 5.3 we compare a normal phase sensitive AOOCT where the eye motion needs to be corrected for in post processing and the time trace is showing considerable inconsistencies in the spatial location of the intensity and the phase image.

5.4.1 Retinal Phase imaging with an actively stabilized AOOCT

In Figure 5.3, we show both the intensity and corresponding phase image of a normal AOOCT in comparison to an actively stabilized AOOCT. The intensity images show time traces of the ISOS junction to confirm whether the same structure is imaged throughout the entire acquisition. The phase time trace shows the phase difference between the COST and the ISOS over time. The image reveals any changes in OPL during the 8-second acquisition and we can appreciate high consistency, while phase noise is evident in areas with lower signal intensity.

Conventional AOOCT B-scans need to be registered in post processing while the raw data from the stabilized AOOCT successfully recorded from the same series of cones over the entire 8-second acquisition. The phase images are very sensitive which clearly shows any stabilization

errors as horizontal streaks in the image. The spatial areas with low signal in the intensity image relayed noisy phase measurements since the fidelity is a proportional to the signal intensity.

For further comparison, both the signal intensity and phase were analyzed before and after lateral registration to see incremental improvements in both signals. In Figure 5.4 we can see improvement in the lateral registration most evident in the left side, where the dim structures show a crisp line of signal over time. Although these improvements are incremental, we can confidently locate a series of cone photoreceptors throughout the acquisition without any additional lateral registration. Although the registration seems to improve the contiguity of the traces, the gains are marginal, demonstrating the efficacy of active eye tracking.

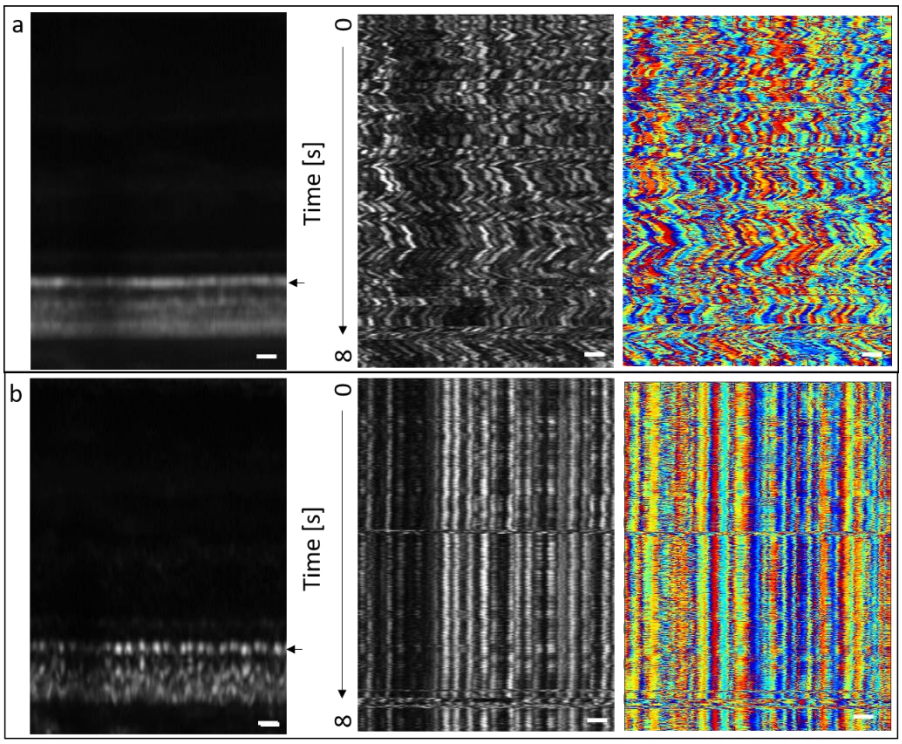

Figure 5.3: The top row shows raw data from a normal AOOCT with a fixed B-scan protocol in which the data needs to be registered in post processing; on the bottom row we see the raw data from an actively stabilized AOOCT in which a fixed B-scan can target a given spatial location with stable phase information throughout the 8 second acquisition.

5.4.2 Quantifying the Optoretinogram using an actively stabilized AOOCT

The active stabilization enabled the AOOCT to be fixed on a particular set of cones to repeatedly measure the functional activity. A particular series of cones was chosen from the AOSLO en face and a fixed B-scan protocol was implemented to record B-scans from a series of photoreceptors while a stimulus was flashed from an AOSLO imaging channel. The subject sat out and dark adapted for approximately 2 minutes and then sat back in for repeated acquisition of the same series of photoreceptors. Within a 20-minute time span, 5 series of functional experiments were collected from the same set of photoreceptors.

In Figure 5.5, the first panel of the average B-scan for 5 stimulus acquisitions shows the spatial targeting accuracy of the actively stabilized AOOCT as we visually confirm the same series of cones are apparent in each of the B-scan from the 8-second average. The middle column shows the structural signal from the ISOS junction over the 8-second acquisition. The last column shows the corresponding phase information of the OPL between the ISOS junction to the COST. We can track the same structures in all three columns and note the stronger signal intensity in the B-scan average and the structure of the ISOS over time, the cleaner the visual phase image looks with a distinct change in phase with the stimuli.

The lateral fluctuations have two main components, the large shifts from microsaccades of high velocity motion and the smaller lateral shifts which are comprised of scanner jitter and residual eye motion. The slight intensity variations result from the subject's tear film and eye motion stability to the AO loop fluctuations; these intensity variations result in phase noise variations across the different traces as the phase noise is inversely proportional on the signal intensity.

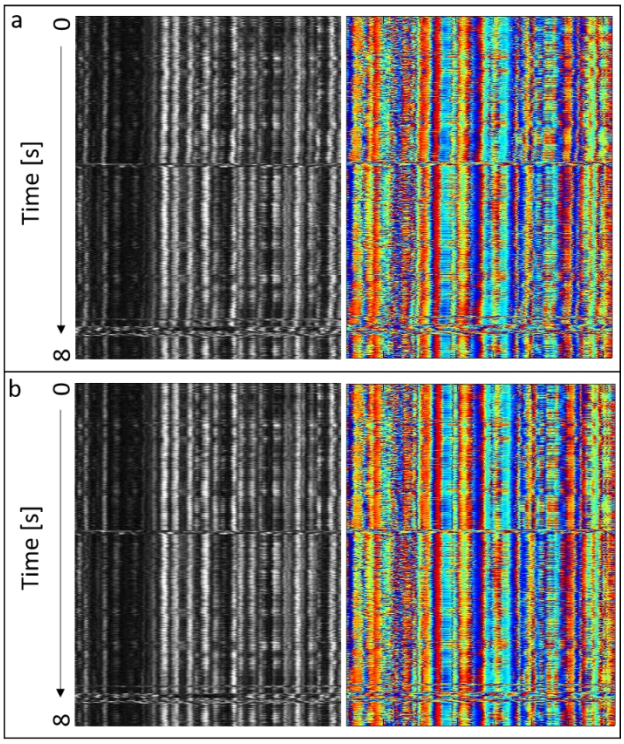

Figure 5.4: The images in this figure refer to a fixed line scan over an 8-second acquisition. The signal intensity of the ISOS junction is plotted in the intensity panels on the left and the phase images show the baseline OPL between the ISOS and COST. The top panel shows the raw data with only axial motion correction in post processing, while the bottom panel presents the same data with post hoc lateral registration.

The photoreceptors with the strongest ISOS and COST intensity were chosen to extract functional information throughout the series of acquisitions. The OPL between these two reflections was measured as a function of time over the 5 acquisitions and is annotated by color in

the plot. These time traces were filtered based on combination of structural and phase filters based on the average content. The structural filter was based on a cross correlation over time to filter the microsaccades and residual eye motion artifacts; the phase filter used a rolling phase average over 10 time points to filter large jumps in phase from the residual eye motion artifacts.

In the last panel of Figure 5.6, we see 25 individual traces are plotted over time and are annotated based on the spatial location; these traces are easily grouped into two main categories with a strong response to the stimuli on the order of 350 nanometers, and a weaker response to the stimuli on the order of 100 nanometers for a 15 percent bleach using 630 nanometer wavelength stimuli. These values correspond to the published literature in which the L cones exhibit the larger response to a red stimulus and the M cones show a response smaller by about 100 nanometer(Azimipour, Migacz, et al., 2019; Hillmann et al., 2016; Pandiyan et al., 2020; Zhang et al., 2019).

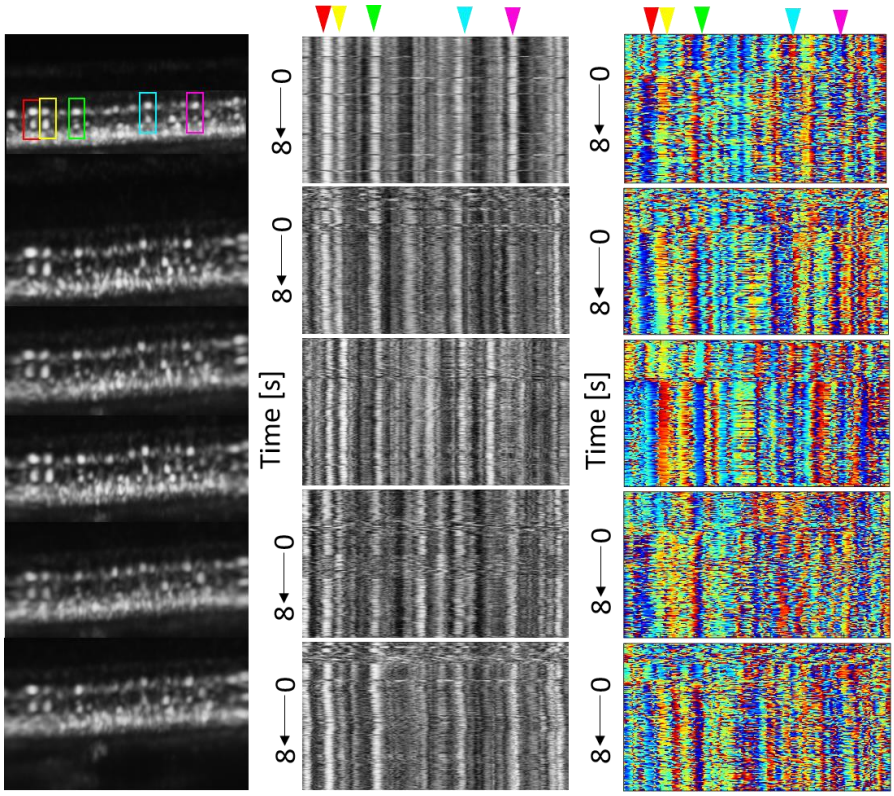

Figure 5.5: Visual comparison of the repeated stimulus series of scans from the same retinal location. a) Average B-scan from each dataset. b) Corrresponding time trace of the ISOS/COST phase difference for each dataset, obtained without post hoc lateral registration. Here, we see a distinct change in the OPL throughout the series of phase images at about 1 second in, correpsonding to when the stimulus is shown. Each phase plot corresponds to the full acquisition of an individual averaged B-scan shown on the left. We can appreciate the same structures indicated by the color boxes on the left refering to the colored carrots on the right series of images.

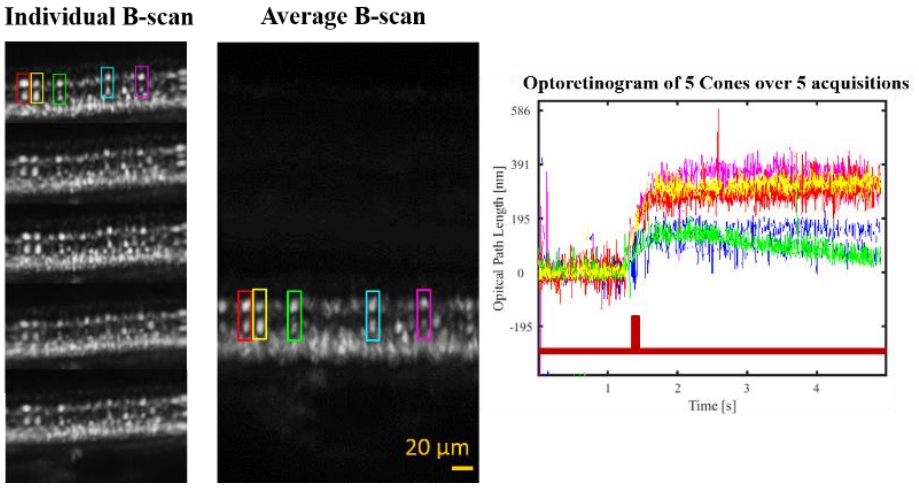

Figure 5.6: a,b,c Here we show repeated measurements of 5 distinct cone photoreceptors over 5 acquisitions. When the 25 traces are plotted against each other we see that the colored traces are tightly grouped and two distinct groups of responses are present. The traces were filtered for stabilization errors based on the intesity variations resulting in large sporadic phase jumps.

5.5 Discussion

In this chapter we successfully recorded an adaptive optics optoretinogram with active stabilization. This technology successfully records function of a targeted patch of photoreceptors with no additional lateral registration necessary. By using a spatial reference for the AOSLO tracking, the patch of retina can be repeatedly probed with stimuli and in Figure 5.5 and Figure 5.6 we can appreciate the repeated exposures of the same photoreceptors which are showing correlated responses over the series of experiments.

Firstly, we chose to image a small patch of photoreceptors to densely oversample in the scanning direction, such that each cone is imaged with multiple A-lines, so that we can compare the complex information from adjacent scans. We are able to sample each photoreceptor with over 5 to 20 A-lines to average these signals for strong correlations across datasets. We also see the lateral similarities in Figure 5.5 with a few pixels correlating spatially throughout the B-scan.

Eye tracking technology for obtaining the optoretinogram via AOOCT was demonstrated by presenting time traces of AOOCT data without post hoc lateral registration. We demonstrated the ability to extract high fidelity functional information by showing the baseline OPL between ISOS and COST from a selected set of photoreceptors over a time scale of several seconds. Active functional information was measured by stimulating the retina with a 100 ms long flash of 630 nm light. Our protocol allowed us to follow the OPL time-profile of individual photoreceptors over 8 seconds and over distinct acquisitions. In turn, the time profiles allowed to identify photoreceptors

belonging to different cone classes. These results show the potential of AOSLO-based active eye tracking technology to obtain targeted functional information from specific structures within the human retina.

Nevertheless, the technology has some limitations. First, stabilization errors create discontinuity in the phase information that complicate extraction of accurate functional time profiles. The errors can come from large microsaccades that exceed the registration capability, tracking failures, or limitations of the tip-tilt scanner module. Large discontinuities such as those caused by uncorrected microsaccades or tracking failures are cumbersome to correct and can cause degradation of the signal if they last for several frames. Smaller discontinuities such as those arising from the scanner jitter or high-frequency small-amplitude motion can be partially corrected in post processing using lateral registration as shown in Figure 5.4, unless they occur in the direction perpendicular to the scanning plane. If there is a distortion present in the spatial reference image for AOSLO tracking, the succeeding eye motion traces will have a small amplitude tracking error introduced corresponding to the reference distortion.

For a strong repeatable functional measurement of the OPL between the ISOS and the COST, the signal of both interfaces requires a strong signal intensity for reliable phase measurements; if either of these interfaces is a weak scatterer, the measured phase component will be noisy, resulting in OPL traces with high noise. Evidence of this effect can be visualized in phase time traces, which show more noise on the right half of the image which had lower signal intensity shown in the B-scan averaged image as shown in Figure 5.5.

A key feature of this system is that the obtained AOOCT data require minimal postprocessing, namely a usual OCT signal processing protocol and axial registration. The need of lateral registration, which normally requires to acquire spatial data densely sampled in time, is considerably reduced through active eye tracking. This property was demonstrated by presenting optoretinogram obtained without post hoc lateral registration. We found that post processing lateral registration, albeit effective, only provided marginal gains to the cost of increased processing time and complexity, so we decided to avoid it altogether.

Future experiments will involve the use of the system to target a single neuron and acquire extremely high-rate measurements to observe ultrafast dynamics. Future technical improvements will include using a galvo scanner to produce jitter-free B-scans while using the tip-tilt for slow axis scans and eye motion compensation. Moreover, our system is based on 1050 nm swept source technology by the desire to have an ‘invisible’ probe that would not interfere with physiological and psychophysical experiments. However, since longer wavelengths experience less scattering, the backscattering intensity and, therefore, phase information is affected too. Since all retinal neurons (such as retinal ganglion cells) and photoreceptors reside in more proximal structures, it could be considered to replace the AOOCT engine with one based on wavelength of ~800 nm, which would improve backscattering and possibly phase stability. However, these advantages would have to be weighed against the requirement for a careful system redesign as the current imaging wavelength for AOSLO is 840 nm, and to the fact that focused 800 nm light is visible to the human eye, which could potentially interfere with the experimental procedures.

Overall, we show the actively stabilized AOOCT can correct for eye motion in real time shifting the technical complexity from needing high-speed AOOCT and ad hoc post processing algorithms to the acquisition producing high fidelity optoretinogram within the relatively raw data. A drawback of the technology is the sensitivity to scanning jitter and residual motion artifacts. The main advantage of this system is the raw data is rich with high quality phase information obtained from a targeted location in the retina.

5.6 Conclusion

We successfully implemented an actively stabilized phase sensitive AOOCT system to measure the optoretinogram of a spatially targeted location repeatedly. We show that the AOOCT was able to lock onto a set of select cone photoreceptors and reliably record the optical path length of the cell reliably and repeatedly. We were able to successfully quantify the response of individual photoreceptors to light stimuli to obtain the optoretinogram repeatedly for confident classification of a set of cones within as single imaging session with minimal postprocessing.

Funding

National Institutes of Health (National Eye Institute) (T32EY007043, R01EY023591, U01EY025501, P30-EY003176), Alcon Research Investigator Award, Minnie Flaura Turner Memorial Fund for Impaired Vision Research, Soroptimist International Founders Region Fellowship.

Disclosures

AR:USPTO #7,118,216, "Method and apparatus for using AO in a scanning laser ophthalmoscope" and USPTO #6,890,076, "Method and apparatus for using AO in a scanning laser ophthalmoscope". These patents are assigned to both the University of Rochester and the University of Houston and are currently licensed to Boston Micromachines Corporation in Cambridge, Massachusetts. Both AR and the company may benefit financially from the publication of this research.

This paper is a work in progress presented as a Presentation at ARVO 2020 and ARVO 2021, but yet to be published. The theoretical optical design of the AOOCT paper was done by Francesco LaRocca. The OCT MZI, system computer and OCT infrastructure was supported by Patrick Gregory, Hyle Park and Fabio Feroldi. The software, the code for the analysis developed and half of the paper was written by Fabio Feroldi. The electronic implementation and testing was supported by Fabio Feroldi, Pavan Tiruveedhula and Austin Roorda. The AOOCT and AOSLO building, aligning, implementation, image analysis, subject and the writing of the paper was done by Sanam Mozaffari.

Bibliography

(BORG), B. O. R. G. (2011). *Biomedical Optics Research Group (BORG)*. University, Simon Fraser.

Abbe, E. (1873). Beiträge zur Theorie des Mikroskops und der mikroskopischen. *Archiv f. Mikrosk. Anatomie*, *9*(1), 413–468.

Abramoff, M. D., Kwon, Y. H., Tso, D., Soliz, P., Zimmerman, B., Pokorny, J., & Kardon, R. (2006). Visual stimulus induced changes in human near-infrared fundus reflectance. *Investigative Ophthalmology and Visual Science*, *47*(2), 715–721.

Akkin, T., Landowne, D., & Sivaprakasam, A. (2009). Optical coherence tomography phase measurement of transient changes in squid giant axons during activity. *Journal of Membrane Biology*, *231*(1), 35–46. https://doi.org/10.1007/s00232-009-9202-4

Anderson, A. G., Olshausen, B. A., Ratnam, K., & Roorda, A. (2017). A neural model of high-acuity vision in the presence of fixational eye movements. *Conference Record - Asilomar Conference on Signals, Systems and Computers*, 588–592. https://doi.org/10.1109/ACSSC.2016.7869110

Anderson, A. G., Ratnam, K., Roorda, A., & Olshausen, B. A. (2020). High-acuity vision from retinal image motion. *Journal of Vision*, *20*(7), 34–34. https://doi.org/10.1167/JOV.20.7.34

ANSI. (2014). American National Standard for safe use of lasers (ANSI 136.1). *The Laser Institute of America. ANSI*, *136*(1).

Arathorn, D. W., Stevenson, S. B., Yang, Q., Tiruveedhula, P., & Roorda, A. (2013). How the unstable eye sees a stable and moving world. *Journal of Vision*, *13*(10), 10. https://doi.org/10.1167/13.10.22

Arathorn, D. W., Yang, Q., Vogel, C. R., Zhang, Y., Tiruveedhula, P., & Roorda, A. (2007). Retinally stabilized cone-targeted stimulus delivery. *Optics Express*, *15*(21), 13731. https://doi.org/10.1364/oe.15.013731

Atchison, D. A., & Smith, G. (2005). Chromatic dispersions of the ocular media of human eyes. *Journal of the Optical Society of America*, *22*(1), 29. https://doi.org/10.1364/josaa.22.000029

Azimipour, M., Jonnal, R. S., Werner, J. S., & Zawadzki, R. J. (2019). Coextensive synchronized SLO-OCT with adaptive optics for human retinal imaging. *Optics Letters*, 44(17), 4219. https://doi.org/10.1364/ol.44.004219

Azimipour, M., Migacz, J. V., Zawadzki, R. J., Werner, J. S., & Jonnal, R. S. (2019). Functional retinal imaging using adaptive optics swept-source OCT at 1.6 MHz. *Optica*, *6*(3), 300. https://doi.org/10.1364/optica.6.000300

Azimipour, M., Zawadzki, R. J., Gorczynska, I., Migacz, J. V., Werner, J. S., & Jonnal, R. S. (2018). Intraframe motion correction for raster-scanned adaptive optics images using strip-based cross-correlation lag biases. *PLoS ONE*, *13*(10), 1–24. https://doi.org/10.1371/journal.pone.0206052

Azuma, T., & Kei, T. (2015). Super-resolution spinning-disk confocal microscopy using optical photon reassignment. *Optics Express, 23*(11), 15003. https://doi.org/10.1364/oe.23.015003

Bedford, R. E., & Wyszecki, G. (1957). Axial chromatic aberration of the human eye. *Journal of the Optical Society of America, 47*(6), 564–565. https://doi.org/10.1364/josa.47.0564_1

Bizheva, K., Pflug, R., Hermann, B., Považay, B., Sattmann, H., Qiu, P., Anger, E., Reitsamer, H., Popov, S., Taylor, J. R., Unterhuber, A., Ahnelt, P. K., & Drexler, W. (2006). Optophysiology: Depth-resolved probing of retinal physiology with functional ultrahigh-resolution optical tomography. *Proceedings of the National Academy of Sciences of the United States of America, 103*(13), 5066–5071. https://doi.org/10.1073/pnas.0506997103

Blatter, C., Grajciar, B., Schmetterer, L., & Leitgeb, R. A. (2013). Angle independent flow assessment with bidirectional Doppler optical coherence tomography. *Optics Letters, 38*(21), 4433. https://doi.org/10.1364/ol.38.004433

Boehm, A. E., Privitera, C. M., Schmidt, B. P., & Roorda, A. (2018). Transverse chromatic offsets with pupil displacements in the human eye: Sources of variability and methods for real-time correction. *Biomedical Optics Express, 10*(4), 1691–1706. https://doi.org/10.1101/484386

Bowers, N. R., Boehm, A. E., & Roorda, A. (2019). The effects of fixational tremor on the retinal image. *Journal of Vision, 19*(11), 8. https://doi.org/10.1101/403964

Boyle, K. C., Chen, Z. C., Ling, T., Pandiyan, V. P., Kuchenbecker, J., Sabesan, R., & Palanker, D. (2020). On mechanisms of light-induced deformations in photoreceptors. *Biophysical Journal, 119*(8), 1481–1488. https://doi.org/10.1101/2020.01.08.897728

Braaf, B., Vermeer, K. A., Sicam, V. A. D. P., van Zeeburg, E., van Meurs, J. C., & de Boer, J. F. (2011). Phase-stabilized optical frequency domain imaging at 1-μm for the measurement of blood flow in the human choroid. *Optics Express, 19*(21), 20886. https://doi.org/10.1364/oe.19.020886

Braaf, B., Vermeer, K. A., Vienola, K. V., & de Boer, J. F. (2012). Angiography of the retina and the choroid with phase-resolved OCT using interval-optimized backstitched B-scans. *Optics Express, 20*(18). https://doi.org/10.1364/OE.20.020516

Braaf, B., Vienola, K. V., Sheehy, C. K., Yang, Q., Vermeer, K. A., Tiruveedhula, P., Arathorn, D. W., Roorda, A., & de Boer, J. F. (2013). Real-time eye motion correction in phase-resolved OCT angiography with tracking SLO. *Biomedical Optics Express, 4*(1), 51. https://doi.org/10.1364/boe.4.000051

Brea, L. S., De Jesus, D. A., Shirazi, M. F., Pircher, M., van Walsum, T., & Klein, S. (2019). Review on retrospective procedures to correct retinal motion artefacts in OCT imaging. *Applied Sciences (Switzerland), 9*(13). https://doi.org/10.3390/app9132700

Brown, K. T. & Murakami, M. (1964). A New Receptor Potential of the Monkey Retina with no Detectable Latency. *Nature, 201*, 626–628.

Bruce, K. S., Harmening, W. M., Langston, B. R., Tuten, W. S., Roorda, A., & Sincich, L. C. (2015). Normal perceptual sensitivity arising from weakly reflective cone photoreceptors. *Investigative Ophthalmology and Visual Science, 56*(8), 4431–4438.

https://doi.org/10.1167/iovs.15-16547

Bryant, S. H., & Tobias, J. M. (1952). Changes in light scattering accompanying activity in nerve. *Journal of Cellular Physiology*, *40*(2), 199–219. https://doi.org/10.1002/jcp.1030400204

Bryant, S. H., & Tobias, J. M. (1955). Optical and mechanical concomitants of activity in Carcinus nerve. I. Effect of sodium azide on the optical response. II. Shortening of the nerve with activity. *Journal of Cellular Physiology*, *46*(1), 71–95. https://doi.org/10.1002/jcp.1030460105

Burns, S. A., Elsner, A. E., Sapoznik, K. A., Warner, R. L., & Gast, T. J. (2019). Adaptive optics imaging of the human retina. *Progress in Retinal and Eye Research*, *68*(June 2018), 1–30. https://doi.org/10.1016/j.preteyeres.2018.08.002

Carroll, J. (2008). Adaptive Optics Retinal Imaging. *Archives of Ophthalmology*, *126*(6), 857. https://doi.org/10.1001/archopht.126.6.857

Castello, M., Sheppard, C. J. R., Diaspro, A., & Vicidomini, G. (2015). Image scanning microscopy with a quadrant detector. *Optics Letters*, *40*(22), 5355. https://doi.org/10.1364/ol.40.005355

Cense, B., Nassif, N. A., Chen, T. C., Pierce, M. C., Yun, S.-H., Park, B. H., Bouma, B. E., Tearney, G. J., & de Boer, J. F. (2004). Ultrahigh-resolution high-speed retinal imaging using spectral-domain optical coherence tomography. *Optics Express*, *12*(11). https://doi.org/10.1364/opex.12.002435

Chen, C. L., & Wang, R. K. (2017). Optical coherence tomography based angiography [Invited] . *Biomedical Optics Express* (Vol. 8, Issue 2, pp. 1056–1082). https://doi.org/10.1364/BOE.8.001056

Chinn, S. R., & Swanson, E. A. (1997). Optical coherence tomography using a frequency-tunable optical source. *Optics Letters*, *22*(5), 340–342.

Choi, W., Mohler, K. J., Potsaid, B., Lu, C. D., Liu, J. J., Jayaraman, V., Cable, A. E., Duker, J. S., Huber, R., & Fujimoto, J. G. (2013). Choriocapillaris and choroidal microvasculature imaging with ultrahigh speed OCT angiography. *PLoS ONE*, *8*(12). https://doi.org/10.1371/journal.pone.0081499

Choma, M. A., Ellerbee, A. K., Yang, C., Creazzo, T. L., & Izatt, J. A. (2005). Spectral-domain phase microscopy. *Optics Letters*, *30*(10), 1162–1164.

Choma, M. A., Sarunic, M. V, Yang, C., & Izatt, J. A. (2003). Sensitivity advantage of swept source and Fourier domain optical coherence tomography. *Optics Express*, *11*(18), 2183. https://doi.org/10.1364/oe.11.002183

Chui, T. Y. P., VanNasdale, D. A., & Burns, S. A. (2012). The use of forward scatter to improve retinal vascular imaging with an adaptive optics scanning laser ophthalmoscope. *Biomedical Optics Express*, *3*(10), 2537. https://doi.org/10.1364/boe.3.002537

Claxton, N. S., Fellers, T. J., & Davidson, M. W. (2011). Laser Scanning Confocal Microscopy (LSCM). *Springer Reference*, *1979*(21). https://doi.org/10.1007/springerreference_67032

Cohen, L., & Keynes, R. (1971). Changes in light scattering associated with the action potential in crab nerves. *The Journal of Physiology*, *212*, 259–275.

Cohen, L., Keynes, R., & Hille, B. (1968). Light scattering and birefringence changes during nerve activity. *Nature*, *218*(5140), 438–441.

Cooper, R. F., Brainard, D. H., & Morgan, J. I. W. (2020). Optoretinography of individual human cone photoreceptors. *Optics Express*, *28*(26), 39326–39339.

Cordeiro, C., Abilez, O. J., Goetz, G., Gupta, T., Zhuge, Y., Solgaard, O., & Palanker, D. (2017). Optophysiology of cardiomyocytes: characterizing cellular motion with quantitative phase imaging. *Biomedical Optics Express*, *8*(10), 4652. https://doi.org/10.1364/BOE.8.004652

Cornsweet, T. N., & Crane, H. D. (1973). Accurate two-dimensional eye tracker using first and fourth Purkinje images. *Journal of the Optical Society of America*, *63*(8), 921–928. https://doi.org/10.1364/JOSA.63.000921

Cox, I. J., Sheppard, C. J. R., & Wilson, T. (1982). Improvement in resolution by nearly confocal microscopy. *Applied Optics*, *21*(5), 778. https://doi.org/10.1364/ao.21.000778

de Boer, J. F., Cense, B., Park, B. H., Pierce, M. C., Tearney, G. J., Bouma, B. E., Boer, J. F. De, Cense, B., Park, B. H., Pierce, M. C., Tearney, G. J., & Bouma, B. E. (2003). Improved signal-to-noise ratio in spectral-domain compared with time-domain optical coherence tomography. *Optics Letters*, *28*(21), 2067. https://doi.org/10.1364/ol.28.002067

de Boer, J. F., Hitzenberger, C. K., & Yasuno, Y. (2017). Polarization sensitive optical coherence tomography; a review [Invited]. *Biomedical Optics Express*, *8*(3), 1838–1873. https://doi.org/10.1364/BOE.8.001838

De Luca, G. M. R., Breedijk, R. M. P., Brandt, R. A. J., Zeelenberg, C. H. C., de Jong, B. E., Timmermans, W., Azar, L. N., Hoebe, R. A., Stallinga, S., & Manders, E. M. M. (2013). Re-scan confocal microscopy: scanning twice for better resolution. *Biomedical Optics Express*, *4*(11), 2644. https://doi.org/10.1364/boe.4.002644

Defrise, M., & De Mol, C. (1992). Super-resolution in confocal scanning microscopy: Generalized inversion formulae. *Inverse Problems*, *8*(2), 175–185. https://doi.org/10.1088/0266-5611/8/2/001

Delori, F. C., Webb, R. H., & Sliney, D. H. (2007). Maximum permissible exposures for ocular safety (ANSI 2000), with emphasis on ophthalmic devices. *Journal of the Optical Society of America*, *24*(5), 1250. https://doi.org/10.1364/josaa.24.001250

Dhalla, A.-H., Nankivil, D., Bustamante, T., Kuo, A., & Izatt, J. A. (2012). Simultaneous swept source optical coherence tomography of the anterior segment and retina. *Biomedical Optics*, *37*, 1883–1885. https://doi.org/10.1364/biomed.2012.btu2b.3

Dhalla, A.-H., Nankivil, D., & Izatt, J. A. (2012). Complex conjugate resolved heterodyne swept source optical coherence tomography using coherence revival. *Biomedical Optics Express*, *3*(3), 633. https://doi.org/10.1364/boe.3.000633

Domdei, N., Domdei, L., Reiniger, J. L., Linden, M., Holz, F. G., Roorda, A., & Harmening, W. M. (2018). Ultra-high contrast retinal display system for single photoreceptor

psychophysics. *Biomedical Optics Express*, *9*(1), 157. https://doi.org/10.1364/boe.9.000157

Drexler, W. (2001). Ultrahigh-resolution ophthalmic optical coherence tomography. *Nature Medicine*, *23*(1), 502–507. https://doi.org/10.1038/jid.2014.371

Drexler, W., & Fujimoto, J. G. (2006). Optical coherence tomography. *Bioengineering of the Skin: Skin Imaging and Analysis*, 127–136. https://doi.org/10.1016/s1522-1865(04)00002-2

DuBose, T. B., LaRocca, F., Farsiu, S., & Izatt, J. A. (2019). Super-resolution retinal imaging using optically reassigned scanning laser ophthalmoscopy. *Nature Photonics*, *13*(4), 257–262. https://doi.org/10.1038/s41566-019-0369-7

Dubra, A., Gómez-Vieyra, A., Malacara-Hernández, D., & Williams, D. R. (2009). First-order design of off-axis reflective ophthalmic adaptive optics systems using afocal telescopes. *Optics InfoBase Conference Papers*, *17*(21), 1268–1270. https://doi.org/10.1364/aopt.2009.jwf4

Dubra, A., & Sulai, Y. (2011). Reflective afocal broadband adaptive optics scanning ophthalmoscope. *Biomedical Optics Express*, *2*(6), 1757. https://doi.org/10.1364/boe.2.001757

El Hady, A., & Machta, B. B. (2015). Mechanical surface waves accompany action potential propagation. *Nature Communications*, *6*, 1–7. https://doi.org/10.1038/ncomms7697

Elsner, A. E., Burns, S. A., Weiter, J. J., & Delori, F. C. (1996). Infrared imaging of sub-retinal structures in the human ocular fundus. *Vision Research*, *36*(1), 191–205. https://doi.org/10.1016/0042-6989(95)00100-E

Encyclopaedia Britannica. (2012).

Felberer, F., Kroisamer, J.-S., Hitzenberger, C. K., & Pircher, M. (2012). Lens based adaptive optics scanning laser ophthalmoscope. *Optics Express*, *20*(16), 17297. https://doi.org/10.1364/oe.20.017297

Ferguson, R. D., Mujat, M., Maguluri, G., Lu, Y., & Iftimia, N. (2018). Multi-fiber simultaneous offset-aperture AOSLO imaging in the inner retina. *Investigative Ophthalmology and Visual Science*, *59*(9), Abstract #4640. http://dx.doi.org/

Fernández, E. J., Hermann, B., Považay, B., Unterhuber, A., Sattmann, H., Hofer, B., Ahnelt, P. K., & Drexler, W. (2008). Ultrahigh resolution optical coherence tomography and pancorrection for cellular imaging of the living human retina. *Optics Express*, *16*(15), 11083. https://doi.org/10.1364/oe.16.011083

Fernández, E. J., Unterhuber, A., Považay, B., Hermann, B., Artal, P., & Drexler, W. (2006). Chromatic aberration correction of the human eye for retinal imaging in the near infrared. *Optics Express*, *14*(13), 6213. https://doi.org/10.1364/oe.14.006213

Fernández, E. J., Unterhuber, A., Prieto, P. M., Hermann, B., Drexler, W., & Artal, P. (2005). Ocular aberrations as a function of wavelength in the near infrared measured with a femtosecond laser. *Optics Express*, *13*(2), 400. https://doi.org/10.1364/opex.13.000400

Fields, D. R. (2011). Signaling by neuronal swelling. *Science Signaling*, *4*(155), 1–3.

https://doi.org/10.1126/scisignal.4155tr1

Fields, D. R., Shneider, N., Mentis, G. Z., & O'Donovan, M. J. (2009). Imaging nervous system activity. *Current Protocols in Neuroscience*, *SUPPL.49*, 1–16. https://doi.org/10.1002/0471142301.ns0203s49

Fonda, S., Melli, M., Neroni, M., Sargentini, A., Torlai, F., & Peduzzi, M. (1983). Recent developments in eye fundus imaging for clinical application: Television fluoroangiography and new technologies. *Graefe's Archive for Clinical and Experimental Ophthalmology*, *220*(2), 66–70. https://doi.org/10.1007/BF02133872

Foote, K. G., Wong, J. J., Boehm, A. E., Bensinger, E., Porco, T. C., Roorda, A., & Duncan, J. L. (2020). Comparing cone structure and function in Rho- And RPGR-associated retinitis pigmentosa. *Investigative Ophthalmology and Visual Science*, *61*(4). https://doi.org/10.1167/iovs.61.4.42

Gardner, W. D., & Osburn, W. A. (1978). *Anatomy of the human body*. Saunders, W B CO. https://doi.org/10.1097/00007611-192506000-00042

Grieve, K., Tiruveedhula, P., Zhang, Y., & Roorda, A. (2006). Multi-wavelength imaging with the adaptive optics scanning laser Ophthalmoscope. *Optics Express*, *14*(25), 12230. https://doi.org/10.1364/oe.14.012230

Guevara-Torres, A., Joseph, A., & Schallek, J. B. (2016). Label free measurement of retinal blood cell flux, velocity, hematocrit and capillary width in the living mouse eye. *Biomedical Optics Express*, *7*(10), 4228. https://doi.org/10.1364/boe.7.004228

Guevara-Torres, A., Williams, D. R., & Schallek, J. B. (2015). Imaging translucent cell bodies in the living mouse retina without contrast agents. *Biomedical Optics Express*, *6*(6), 2106. https://doi.org/10.1364/boe.6.002106

Guizar-Sicairos, M., Thurman, S. T., & Fienup, J. R. (2008). Efficient subpixel image registration algorithms. *Optics Letters*, *33*(2), 156. https://doi.org/10.1364/ol.33.000156

Hageman, K. N., Chow, M. R., Roberts, D. C., & Santina, C. C. D. (2021). Low-Noise Magnetic Coil System for Recording 3-D Eye Movements. *IEEE Transactions on Instrumentation and Measurement*, *70*. https://doi.org/10.1109/TIM.2020.3020682

Harmening, W. M., Tiruveedhula, P., Roorda, A., & Sincich, L. C. (2012). Measurement and correction of transverse chromatic offsets for multi-wavelength retinal microscopy in the living eye. *Biomedical Optics Express*, *3*(9), 2066–2077.

Harmening, W. M., Tuten, W. S., Roorda, A., & Sincich, L. C. (2014). Mapping the perceptual grain of the human retina. *Journal of Neuroscience*, *34*(16), 5667–5677. https://doi.org/10.1523/JNEUROSCI.5191-13.2014

Heimburg, T., & Jackson, A. D. (2005). On soliton propagation in biomembranes and nerves. *Proceedings of the National Academy of Sciences*, *102*(28), 9790–9795. https://doi.org/10.1073/pnas.0503823102

Hermann, B., Fernández, E. J., Unterhuber, A., Sattmann, H., Fercher, A. F., Drexler, W., Prieto, P. M., & Artal, P. (2004). Adaptive-optics ultrahigh-resolution optical coherence

tomography. *Optics Letters*, *29*(18), 2142. https://doi.org/10.1364/ol.29.002142

Hestrin, S., & Korenbrot, J. I. (1990). Activation kinetics of retinal cones and rods: Response to intense flashes of light. *Journal of Neuroscience*, *10*(6), 1967–1973. https://doi.org/10.1523/jneurosci.10-06-01967.1990

Hill, D. K. (1950). The volume change resulting from stimulation of giant nerve fibre. *The Journal of Physiology*, *111*, 304–327.

Hillmann, D., Spahr, H., Pfäffle, C., Sudkamp, H., Franke, G., & Hüttmann, G. (2016). In vivo optical imaging of physiological responses to photostimulation in human photoreceptors. *Proceedings of the National Academy of Sciences of the United States of America*. https://doi.org/10.1073/pnas.1606428113

Hodgkin, A. L., Huxley, A. F., & Katz, B. (1952). Measurement of current-voltage relations in the membrane of the giant axon of Loligo. *The Journal of Physiology*, *116*(4), 424–448. https://doi.org/10.1113/jphysiol.1952.sp004716

Hodgkin, A. L., & Obryan, P. M. (1977). Internal recording of the early receptor potential in turtle cones. *The Journal of Physiology*, *267*(3), 737–766. https://doi.org/10.1113/jphysiol.1977.sp011836

Hofer, H., Sredar, N., Queener, H., Li, C., & Porter, J. (2011). Wavefront sensorless adaptive optics ophthalmoscopy in the human eye. *Optics Express*, *19*(15), 14160. https://doi.org/10.1364/oe.19.014160

Huang, D., Swanson, E. A., Lin, C. P., Schuman, J. S., Stinson, W. G., Chang, W., Hee, M. R., Flotte, T., Gregory, K., & Puliafito, C. A. (1991). Optical coherence tomography. *Science*, *254*(5035), 1178–1181. https://doi.org/10.1126/science.1957169

Huff, J. (2015). The Airyscan detector from ZEISS: confocal imaging with improved signal-to-noise ratio and super-resolution. *Nature Methods*, *12*(12), i–ii. https://doi.org/10.1038/nmeth.f.388

Hyle Park, B., Pierce, M. C., Cense, B., Yun, S.-H., Mujat, M., Tearney, G. J., Bouma, B. E., & Boer, J. F. de. (2005). Real-time fiber-based multi-functional spectral-domain optical coherence tomography at 13 µm. *Optics Express*. https://doi.org/10.1364/opex.13.003931

Iwasa, K., Tasaki, I., & Gibbons, R. C. (1980). Swelling of nerve fibers associated with action potentials. *Science*, *210*(4467), 338 LP – 339.

Jaedicke, V., Mozaffari, S., LaRocca, F., & Roorda, A. (2018). Multi-detector adaptive optics scanning laser ophthalmoscope. *Proc. SPIE 10474, 104740E*.

Jia, Y., Morrison, J. C., Tokayer, J., Tan, O., Lombardi, L., Baumann, B., Lu, C. D., Choi, W., Fujimoto, J. G., & Huang, D. (2012). Quantitative OCT angiography of optic nerve head blood flow. *Biomedical Optics Express*, *3*(12), 3127. https://doi.org/10.1364/boe.3.003127

Jiang, X., Kuchenbecker, J. A., Touch, P., & Sabesan, R. (2019). Measuring and compensating for ocular longitudinal chromatic aberration. *Optica*, *6*(8), 981. https://doi.org/10.1364/optica.6.000981

Jonnal, R. S., Kocaoglu, O. P., Wang, Q., Lee, S., & Miller, D. T. (2012). Phase-sensitive imaging of the outer retina using optical coherence tomography and adaptive optics. *Biomedical Optics Express*. https://doi.org/10.1364/boe.3.000104

Jonnal, R. S., Kocaoglu, O. P., Zawadzki, R. J., Liu, Z., Miller, D. T., & Werner, J. S. (2016). A review of adaptive optics optical coherence tomography: Technical advances, scientific applications, and the future. *Investigative Ophthalmology and Visual Science*. https://doi.org/10.1167/iovs.16-19103

Jonnal, R. S., Rha, J., Zhang, Y., Cense, B., Gao, W., & Miller, D. T. (2007). In vivo functional imaging of human cone photoreceptors. *Optics Express*, *15*(24), 16141. https://doi.org/10.1364/oe.15.016141

Kim, G. H., Kosterin, P., Obaid, A. L., & Salzberg, B. M. (2007). A mechanical spike accompanies the action potential in mammalian nerve terminals. *Biophysical Journal*, *92*(9), 3122–3129. https://doi.org/10.1529/biophysj.106.103754

Kocaoglu, O. P., Liu, Z., Zhang, F., Kurokawa, K., Jonnal, R. S., & Miller, D. T. (2016). Photoreceptor disc shedding in the living human eye. *Biomedical Optics Express*, *7*(11), 4554. https://doi.org/10.1364/boe.7.004554

Kocaoglu, O. P., Turner, T. L., Liu, Z., & Miller, D. T. (2014). Adaptive optics optical coherence tomography at 1 MHz. *Biomedical Optics Express*, *5*(12), 4186. https://doi.org/10.1364/boe.5.004186

Kraus, M. F., Potsaid, B., Mayer, M. A., Bock, R., Baumann, B., Liu, J. J., Hornegger, J., & Fujimoto, J. G. (2012). Motion correction in optical coherence tomography volumes on a per A-scan basis using orthogonal scan patterns. *Biomedical Optics Express*, *3*(6), 1182. https://doi.org/10.1364/boe.3.001182

Kurokawa, K., Crowell, J. A., Zhang, F., & Miller, D. T. (2020). Suite of methods for assessing inner retinal temporal dynamics across spatial and temporal scales in the living human eye. *Neurophotonics*, *7*(01), 1. https://doi.org/10.1117/1.nph.7.1.015013

Larin, K. V, & Sampson, D. D. (2017). Optical coherence elastography; OCT at work in tissue biomechanics [Invited]. *Biomedical Optics Express*, *8*(2), 1172–1202. https://doi.org/10.1364/BOE.8.001172

LaRocca, F., Nankivil, D., Farsiu, S., & Izatt, J. A. (2014). True color scanning laser ophthalmoscopy and optical coherence tomography handheld probe. *Biomedical Optics Express*, *5*(9), 3204. https://doi.org/10.1364/boe.5.003204

Leitgeb, R., Hitzenberger, C., & Fercher, A. (2003). Performance of fourier domain vs time domain optical coherence tomography. *Optics Express*, *11*(8), 889. https://doi.org/10.1364/oe.11.000889

Lewis, A. L., Katz, M., & Oehrlein, C. (1982). A modified achromatizing lens. *Optometry and Vision Science*, *59*(11), 909–911.

Li, H., Lu, J., Shi, G., & Zhang, Y. (2011). Measurement of oxygen saturation in small retinal vessels with adaptive optics confocal scanning laser ophthalmoscope. *Journal of Biomedical Optics*, *16*(11), 110504. https://doi.org/10.1117/1.3655354

Li, Y., Cheng, H., Alhalili, Z., Xu, G., & Gao, G. (2021). The progress of magnetic sensor applied in biomedicine: A review of non-invasive techniques and sensors. *Journal of the Chinese Chemical Society*, *68*(2), 216–227. https://doi.org/10.1002/jccs.202000353

Liang, J., Williams, D. R., & Miller, D. T. (1997). Supernormal vision and high-resolution retinal imaging through adaptive optics. *Journal of the Optical Society of America*, *14*(11), 2884. https://doi.org/10.1364/josaa.14.002884

Ling, T., Boyle, K. C., Goetz, G., Zhou, P., Quan, Y., Alfonso, F.S., Huang, T.W., & Palanker, D. (2018). *Light: Science and Applications,* 107(7) 2047. https://doi.org/ 10.1038/s41377-018-0107-9

Ling, T., Boyle, K. C., Zuckerman, V., Flores, T., Ramakrishnan, C., Deisseroth, K., & Palanker, D. (2020). High-speed interferometric imaging reveals dynamics of neuronal deformation during the action potential. *Proceedings of the National Academy of Sciences of the United States of America*, *117*(19), 10278–10285. https://doi.org/10.1073/pnas.1920039117

Litts, K. M., Cooper, R. F., Duncan, J. L., & Carroll, J. (2017). Photoreceptor-Based Biomarkers in AOSLO Retinal Imaging. *Investigative Ophthalmology and Visual Science*, *58*(6), 255–267. https://doi.org/10.1167/iovs.17-21868

Liu, Z., Kocaoglu, O. P., & Miller, D. T. (2013). In-the-plane design of an off-axis ophthalmic adaptive optics system using toroidal mirrors. *Biomedical Optics Express*. https://doi.org/10.1364/boe.4.003007

Liu, Z., Kurokawa, K., Hammer, D. X., & Miller, D. T. (2019). In vivo measurement of organelle motility in human retinal pigment epithelial cells. *Biomedical Optics Express*, *10*(8), 4142. https://doi.org/10.1364/boe.10.004142

Liu, Z., Kurokawa, K., Zhang, F., Lee, J. J., & Miller, D. T. (2017). Imaging and quantifying ganglion cells and other transparent neurons in the living human retina. *Proceedings of the National Academy of Sciences of the United States of America*, *114*(48), 12803–12808. https://doi.org/10.1073/pnas.1711734114

Liu, Z., Tam, J., Saeedi, O., & Hammer, D. X. (2018). Trans-retinal cellular imaging with multimodal adaptive optics. *Biomedical Optics Express*, *9*(9), 4246. https://doi.org/10.1364/boe.9.004246

Llorente, L., Diaz-Santana, L., Lara-Saucedo, D., & Marcos, S. (2003). Aberrations of the human eye in visible and near infrared illumination. *Optometry and Vision Science*, *80*(1), 26–35. https://doi.org/10.1097/00006324-200301000-00005

López-Gil, N., & Artal, P. (1997). Comparison of double-pass estimates of the retinal-image quality obtained with green and near-infrared light. *Journal of the Optical Society of America*, *14*(5), 961. https://doi.org/10.1364/josaa.14.000961

Mainster, M. A., Timberlake, G. T., Webb, R. H., & Hughes, G. W. (1982). Scanning Laser Ophthalmoscopy: Clinical Applications. *Ophthalmology*, *89*(7), 852–857. https://doi.org/10.1016/S0161-6420(82)34714-4

Manzanera, S., Canovas, C., Prieto, P. M., & Artal, P. (2008). A wavelength tunable wavefront sensor for the human eye. *Optics Express*, *16*(11), 7748.

https://doi.org/10.1364/oe.16.007748

Marcos, S., Burns, S. A., Moreno-Barriusop, E., & Navarro, R. (1999). A new approach to the study of ocular chromatic aberrations. *Vision Research*, *39*(26), 4309–4323. https://doi.org/10.1016/S0042-6989(99)00145-5

Martinez-Conde, S. (2006). Chapter 8 Fixational eye movements in normal and pathological vision. *Progress in Brain Research*, *154*(SUPPL. A), 151–176. https://doi.org/10.1016/S0079-6123(06)54008-7

Matsumoto, G., Ichikawa, M., Tasaki, A., Murofushi, H., & Sakai, H. (1983). Axonal microtubules necessary for generation of sodium current in squid giant axons. *Journal of Membrane Biology*, *77*(2), 77–91.

Max, C. (2014). Introduction to Adaptive Optics. *American Astronomical Society*, *197*(831), 1–7.

Merino, D., Dainty, C., Bradu, A., & Podoleanu, A. G. (2006). Adaptive optics enhanced simultaneous en-face optical coherence tomography and scanning laser ophthalmoscopy. *Optics Express*, *14*(8), 3345–3353. https://doi.org/10.1364/OE.14.003345

Merino, D., & Loza-Alvarez, P. (2016). Adaptive optics scanning laser ophthalmoscope imaging: Technology update. *Clinical Ophthalmology*, *10*, 743–755. https://doi.org/10.2147/OPTH.S64458

Migacz, J. V., Gorczynska, I., Azimipour, M., Jonnal, R. S., Zawadzki, R. J., & Werner, J. S. (2019). Megahertz-rate optical coherence tomography angiography improves the contrast of the choriocapillaris and choroid in human retinal imaging. *Biomedical Optics Express*, *10*(1), 50. https://doi.org/10.1364/boe.10.000050

Miller, D. T., Kocaoglu, O. P., Wang, Q., & Lee, S. (2011). Adaptive optics and the eye (super resolution OCT). *Eye*, *25*(3), 321–330. https://doi.org/10.1038/eye.2011.1

Miller, D. T., Qu, J., Jonnal, R. S., & Thorn, K. E. (2003). Coherence gating and adaptive optics in the eye. *Coherence Domain Optical Methods and Optical Coherence Tomography in Biomedicine VII*, *4956*(January), 65. https://doi.org/10.1117/12.477633

Modrić, D., Petric Maretić, K., & Hladnik, A. (2014). Determination of point-spread function of paper substrate based on light-scattering simulation. *Applied Optics*, *53*(33), 7854. https://doi.org/10.1364/ao.53.007854

Morgan, J. I. W., Dubra, A., Wolfe, R., Merigan, W. H., & Williams, D. R. (2009). In vivo autofluorescence imaging of the human and macaque retinal pigment epithelial cell mosaic. *Investigative Ophthalmology and Visual Science*, *50*(3), 1350–1359. https://doi.org/10.1167/iovs.08-2618

Morgan, J. I. W., Hunter, J. J., Masella, B., Wolfe, R., Gray, D. C., Merigan, W. H., Delori, F. C., & Williams, D. R. (2008). Light-induced retinal changes observed with high-resolution autofluorescence imaging of the retinal pigment epithelium. *Investigative Ophthalmology and Visual Science*, *49*(8), 3715–3729. https://doi.org/10.1167/iovs.07-1430

Morimoto, C. H., & Mimica, M. R. M. (2005). Eye gaze tracking techniques for interactive applications. *Computer Vision and Image Understanding*, *98*(1), 4–24.

https://doi.org/10.1016/j.cviu.2004.07.010

Mozaffari, S., Jaedicke, V., Larocca, F., Tiruveedhula, P., & Roorda, A. (2018). Versatile multi-detector scheme for adaptive optics scanning laser ophthalmoscopy. *Biomedical Optics Express*, *9*(11), 5477. https://doi.org/10.1364/boe.9.005477

Mozaffari, S., LaRocca, F., Jaedicke, V., Tiruveedhula, P., & Roorda, A. (2020). Wide-vergence, multi-spectral adaptive optics scanning laser ophthalmoscope with diffraction-limited illumination and collection. *Biomedical Optics Express*, *11*(3), 1617. https://doi.org/10.1364/boe.384229

Müller, C. B., & Enderlein, J. (2010). Image scanning microscopy. *Physical Review Letters*, *104*(19), 1–4. https://doi.org/10.1103/PhysRevLett.104.198101

Mulligan, J. B. (2019). The Optoretinogram at 38. *Journal of Vision*, *19*(8), 33. https://doi.org/10.1167/19.8.33

Mulligan, J. B. (1997). Recovery of motion parameters from distortions in scanned images. *Proceedings of the Image Registration Workshop*, 281–292.

Mulligan, J. B., & Macleod, D. I. A. (1994). In search of an optoretinogram. *NASA Ames Research Center*.

Ogboso, Y. U., & Bedell, H. E. (1987). Magnitude of lateral chromatic aberration across the retina of the human eye. *Journal of the Optical Society of America*, *4*(8), 1666. https://doi.org/10.1364/josaa.4.001666

Oh, S., Fang-Yen, C., Choi, W., Yaqoob, Z., Fu, D., Park, Y., Dassari, R. R., & Feld, M. S. (2012). Label-free imaging of membrane potential using membrane electromotility. *Biophysical Journal*, *103*(1), 11–18. https://doi.org/10.1016/j.bpj.2012.05.020

Pandiyan, V. P., Jiang, X., Bertelli, A. M., Kuchenbecker, J. A., Sabesan, R., & Sharma, U. (2020). High-speed adaptive optics line-scan OCT for cellular-resolution optoretinography. *Biomedical Optics Express*, *11*(9), 5274–5296. https://doi.org/10.1101/2020.05.20.105478

Pandiyan, V. P., Maloney-Bertelli, A., Kuchenbecker, J. A., Boyle, K. C., Ling, T., Chen, Z. C., Hyle Park, B., Roorda, A., Palanker, D., & Sabesan, R. (2020). The optoretinogram reveals the primary steps of phototransduction in the living human eye. *Science Advances*, *6*(37), eabc1124. https://doi.org/10.1126/sciadv.abc1124

Pomerantzeff, O., Webb, R. H., & Delori, F. C. (1979). Image formation in fundus cameras. *Investigative Ophthalmology and Visual Science*, *18*(6), 630–637.

Potsaid, B., Jayaraman, V., Fujimoto, J. G., Jiang, J., Heim, P. J. S., & Cable, A. E. (2012). MEMS tunable VCSEL light source for ultrahigh speed 60kHz - 1MHz axial scan rate and long range centimeter class OCT imaging. *Optical Coherence Tomography and Coherence Domain Optical Methods in Biomedicine XVI*, *8213*(February 2012), 82130M. https://doi.org/10.1117/12.911098

Powell, I. (1981). Lenses for correcting chromatic aberration of the eye. *Applied Optics*, *20*(24), 4152–4155.

Qiu, Y., Yang, Y., Liu, Y., Yue, X., & Zhang, Y. (2020). A method to correct longitudinal chromatic aberration between imaging and beacon beams of ocular adaptive optics imaging system. *Journal of Optics (United Kingdom)*, *22*(2). https://doi.org/10.1088/2040-8986/ab6041

Ratnam, K., Domdei, N., Harmening, W. M., & Roorda, A. (2017). Benefits of retinal image motion at the limits of spatial vision. *Journal of Vision*, *17*(1), 30. https://doi.org/10.1167/17.1.30

Ricco, S., Chen, M., Ishikawa, H., Wollstein, G., & Schuman, J. (2009). Correcting motion artifacts in retinal spectral domain optical coherence tomography via image registration. *Lecture Notes in Computer Science (Including Subseries Lecture Notes in Artificial Intelligence and Lecture Notes in Bioinformatics)*, *5761 LNCS*(PART 1), 100–107. https://doi.org/10.1007/978-3-642-04268-3_13

Robinson, N. A. (1963). A method of measuring eye movement using a scleral search coil in a magnetic field. *IEEE Trans. Biomed. Eng.*, *10*, 137–145.

Roider, C., Ritsch-Marte, M., & Jesacher, A. (2016). High-resolution confocal Raman microscopy using pixel reassignment. *Optics Letters*, *41*(16), 3825. https://doi.org/10.1364/ol.41.003825

Roorda, A., Romero-Borja, F., Donnelly III, W. J., Queener, H., Hebert, T. J., & Campbell, M. C. W. (2002). Adaptive optics scanning laser ophthalmoscopy (AOSLO). *Optics Express*, *10*(9), 405–412. https://doi.org/10.1364/oe.10.000405

Roorda, A., & Williams, D. R. (1999). Roorda, A., & Williams, D. R. (1999). The arrangement of the three cone classes in the living human eye. Nature, 397(6719), 520. *Nature*, *397*, 520–522.

Rossi, E. A., Granger, C. E., Sharma, R., Yang, Q., Saito, K., Schwarz, C., Walters, S., Nozato, K., Zhang, J., Kawakami, T., Fischer, W., Latchney, L. R., Hunter, J. J., Chung, M. M., & Williams, D. R. (2017). Imaging individual neurons in the retinal ganglion cell layer of the living eye. *Proceedings of the National Academy of Sciences of the United States of America*, *114*(3), 586–591. https://doi.org/10.1073/pnas.1613445114

Roth, S., Sheppard, C. J. R., Wicker, K., & Heintzmann, R. (2013). Optical photon reassignment microscopy (OPRA). *Optical Nanoscopy*, *2*(1), 1–6. https://doi.org/10.1186/2192-2853-2-5

Rueden, C. T., Schindelin, J., Hiner, M. C., DeZonia, B. E., Walter, A. E., Arena, E. T., & Eliceiri, K. W. (2017). ImageJ2: ImageJ for the next generation of scientific image data. *ArXiv*, *18*, 1–26.

Sabesan, R., Hofer, H., & Roorda, A. (2015). Characterizing the human cone photoreceptor mosaic via dynamic photopigment densitometry. *PLoS ONE*, *10*(12), 1–12. https://doi.org/10.1371/journal.pone.0144891

Sabesan, R., Schmidt, B. P., Tuten, W. S., & Roorda, A. (2016). The elementary representation of spatial and color vision in the human retina. *Science Advances*, *2*(9). https://doi.org/10.1126/sciadv.1600797

Salzberg, B. M., Obaid, A. L., & Gainer, H. (1985). Large and rapid changes in light scattering

accompany secretion by nerve terminals in the mammalian neurohypophysis. *The Journal of General Physiology*, *86*(3), 395–411. https://doi.org/10.1085/jgp.86.3.395

Sapoznik, K. A., Luo, T., de Castro, A., Sawides, L., Warner, R. L., & Burns, S. A. (2018). Enhanced retinal vasculature imaging with a rapidly configurable aperture. *Biomedical Optics Express*, *9*(3), 1323. https://doi.org/10.1364/boe.9.001323

Sasaki, S., Yazawa, I., Miyakawa, N., Mochida, H., Shinomiya, K., Kamino, K., Momose-Sato, Y., & Sato, K. (2002). Optical imaging of intrinsic signals induced by peripheral nerve stimulation in the in vivo rat spinal cord. *NeuroImage*, *17*(3), 1240–1255. https://doi.org/10.1006/nimg.2002.1286

Saxton, R. W. G. and W. O. (1972). A practical algorithm for the determination of the phase from image and diffraction plane pictures. *Optik*, *35*(237).

Schallek, J., Geng, Y., Nguyen, H. V., & Williams, D. R. (2013). Morphology and topography of retinal pericytes in the living mouse retina using in vivo adaptive optics imaging and ex vivo characterization. *Investigative Ophthalmology & Visual Science*, *54*(13), 8237–8250. https://doi.org/10.1167/iovs.13-12581

Schallek, J., Li, H., Kardon, R., Kwon, Y., Abramoff, M., Soliz, P., & Ts'o, D. (2009). Stimulus-evoked intrinsic optical signals in the retina: Spatial and temporal characteristics. *Investigative Ophthalmology and Visual Science*, *50*(10), 4865–4872. https://doi.org/10.1167/iovs.08-3290

Schmidt, B. P., Boehm, A. E., Tuten, W. S., & Roorda, A. (2019). Spatial summation of individual cones in human color vision. *PLoS ONE*, *14*(7). https://doi.org/10.1101/521492

Schmidt, B. P., Sabesan, R., Tuten, W. S., Neitz, J., & Roorda, A. (2018). Sensations from a single M-cone depend on the activity of surrounding S-cones. *Scientific Reports*, *8*(1), 8561. https://doi.org/10.1101/260653

Schulz, O., Pieper, C., Clever, M., Pfaff, J., Ruhlandt, A., Kehlenbach, R. H., Wouters, F. S., Großhans, J., Bunt, G., & Enderlein, J. (2013). Resolution doubling in fluorescence microscopy with confocal spinning-disk image scanning microscopy. *Proceedings of the National Academy of Sciences of the United States of America*, *110*(52), 21000–21005. https://doi.org/10.1073/pnas.1315858110

Scoles, D., Sulai, Y. N., & Dubra, A. (2013). In vivo dark-field imaging of the retinal pigment epithelium cell mosaic. *Biomedical Optics Express*, *4*(9), 1710. https://doi.org/10.1364/boe.4.001710

Scoles, D., Sulai, Y. N., Langlo, C. S., Fishman, G. A., Curcio, C. A., Carroll, J., & Dubra, A. (2014). In Vivo Imaging of Human Cone Photoreceptor Inner Segments. *Investigative Ophthalmology and Visual Science*, *55*(7), 4244–4251. https://doi.org/10.1167/iovs.14-14542

Shaipanich, T., Pahlevaninezhad, H., & Lam, S. (2017). Optical Coherence Tomography: A Review. *Interventions in Pulmonary Medicine*, *5*(4), 267–279. https://doi.org/10.1007/978-3-319-58036-4_16

Sheehy, C. K., Tiruveedhula, P., Sabesan, R., & Roorda, A. (2015). Active eye-tracking for an

adaptive optics scanning laser ophthalmoscope. *Biomedical Optics Express*, *6*(7), 2412. https://doi.org/10.1364/boe.6.002412

Sheehy, C. K., Yang, Q., Arathorn, D. W., Tiruveedhula, P., de Boer, J. F., & Roorda, A. (2012). High-speed, image-based eye tracking with a scanning laser ophthalmoscope. *Biomedical Optics Express*, *3*(10), 2611. https://doi.org/10.1364/boe.3.002611

Sheppard, C. J. R. (1988). Super-resolution in confocal imaging. *Optik (Jena)*, *80*(2), 53–54. https://doi.org/10.1117/12.967201

Simonet, P., & Campbell, M. C. W. (1990). The optical transverse chromatic aberration on the fovea of the human eye. *Vision Research*, *30*(2), 187–206. https://doi.org/10.1016/0042-6989(90)90035-J

Sincich, L. C., Zhang, Y., Tiruveedhula, P., Horton, J. C., & Roorda, A. (2009). Resolving single cone inputs to visual receptive fields. *Nature Neuroscience*, *12*(8), 967–969. https://doi.org/10.1038/nn.2352

Smirnov, M. S. (1961). Measurement of the wave aberration of the human eye. *Biophysics*, *6*(5–6), 776–795.

Spahr, H., Hillmann, D., Hain, C., Pfäffle, C., Sudkamp, H., Franke, G., & Hüttmann, G. (2015). Imaging pulse wave propagation in human retinal vessels using full-field swept-source optical coherence tomography. *Optics Letters*, *40*(20), 4771. https://doi.org/10.1364/ol.40.004771

Sredar, N., Fagbemi, O. E., & Dubra, A. (2018). Sub-airy confocal adaptive optics scanning ophthalmoscopy. *Translational Vision Science and Technology*, *7*(2). https://doi.org/10.1167/tvst.7.2.17

Srinivasan, V. J., Chen, Y., Duker, J. S., & Fujimoto, J. G. (2009). In vivo functional imaging of intrinsic scattering changes in the human retina with high-speed ultrahigh resolution OCT. *Optics Express*, *17*(5), 3861. https://doi.org/10.1364/oe.17.003861

Srinivasan, V. J., Wojtkowski, M., Fujimoto, J. G., & Duker, J. S. (2006). In vivo measurement of retinal physiology with high-speed ultrahigh-resolution optical coherence tomography. *Optics Letters*, *31*(15), 2308. https://doi.org/10.1364/ol.31.002308

Stepnoski, R. A., LaPorta, A., Raccuia-Behling, F., Blonder, G. E., Slusher, R. E., & Kleinfeld, D. (1991). Noninvasive detection of changes in membrane potential in cultured neurons by light scattering. *Proc National Acadamey Science U S A*, *88*(21), 9382–9386. https://doi.org/10.1073/pnas.88.21.9382

Stetter, M., Sendtner, R. A., & Timberlake, G. T. (1996). A novel method for measuring saccade profiles using the scanning laser ophthalmoscope. *Vision Research*, *36*(13), 1987–1994. https://doi.org/10.1016/0042-6989(95)00276-6

Stevenson, S. B., & Roorda, A. (2005). Correcting for miniature eye movements in high-resolution scanning laser ophthalmoscopy. *In F. Manns, P. Soderberg, & A. Ho (Eds.), Ophthalmic Technologies XI Bellingham, WA: SPIE.*, *5688*, 12. https://doi.org/10.1117/12.591190

Stevenson, S. B., Roorda, A., & Kumar, G. (2010). Eye tracking with the adaptive optics scanning laser ophthalmoscope. *Eye Tracking Research and Applications Symposium (ETRA)*, 195–198. https://doi.org/10.1145/1743666.1743714

Swanson, E. A. (1992). High-speed optical coherence domain reflectometry. *Optics Letters. 17*(2), 151–153. https://doi.org/10.1364/OL.17.000151

Swanson, E. A., & Fujimoto, J. G. (2017). The ecosystem that powered the translation of OCT from fundamental research to clinical and commercial impact [Invited]. *Biomedical Optics Express*, *8*(3), 1638. https://doi.org/10.1364/boe.8.001638

Świrski, L., Bulling, A., & Dodgson, N. (2012). Robust real-time pupil tracking in highly off-axis images. *Eye Tracking Research and Applications Symposium (ETRA)*, 173–176. https://doi.org/10.1145/2168556.2168585

Tam, J., Liu, J., Dubra, A., & Fariss, R. (2016). In vivo imaging of the human retinal pigment epithelial mosaic using adaptive optics enhanced indocyanine green ophthalmoscopy. *Investigative Ophthalmology and Visual Science*, *57*(10), 4376–4384. https://doi.org/10.1167/iovs.16-19503

Tam, J., Martin, J. A., & Roorda, A. (2010). Noninvasive visualization and analysis of parafoveal capillaries in humans. *Investigative Ophthalmology and Visual Science*, *51*(3), 1691–1698. https://doi.org/10.1167/iovs.09-4483

Tasaki, I., & Byrne, P. M. (1984). Mechanical changes in the amphibian spinal cord produced by afferent volleys of nerve impulses. *Brain Research*, *301*(2), 265–272. https://doi.org/10.1016/0006-8993(84)91095-3

Tasaki, I., & Byrne, P. M. (1987). Rapid mechanical changes in the amphibian retina evoked by brief light pulses. *Biochemical and Biophysical Research Communications*, *143*(1), 93–97. https://doi.org/10.1016/0006-291X(87)90634-6

Tasaki, I., & Byrne, P. M. (1988). Large mechanical changes in the bullfrog olfactory bulb evoked by afferent fiber stimulation. *Brain Research*, *475*(1), 173–176. https://doi.org/10.1016/0006-8993(88)90214-4

Tasaki, I., Kusano, K., & Byrne, P. M. (1989). Rapid mechanical and thermal changes in the garfish olfactory nerve associated with a propagated impulse. *Biophysical Journal*, *55*(6), 1033–1040. https://doi.org/10.1016/S0006-3495(89)82902-9

Terakawa, S. (1983). Changes in intracellular pressure in sqiud giant axons associated with production of action potentials. *Biochemistry Biophysical Res. Communication*, *114*(3), 1006–1010. https://doi.org/10.1016/0006-291X(83)90661-7

Thibos, L. N., Bradley, A., Still, D. L., Zhang, X., & Howarth, P. A. (1990). Theory and measurement of ocular chromatic aberration. *Vision Research*, *30*(1), 33–49. https://doi.org/10.1016/0042-6989(90)90126-6

Timberlake, G. T., Mainster, M. A., Peli, E., Augliere, R. A., Essock, E. A., & Arend, L. E. (1986). Reading with a macular scotoma. I. Retinal location of scotoma and fixation area. *Investigative Ophthalmology and Visual Science*, *27*(7), 1137–1147.

Torti, C., Považay, B., Hofer, B., Unterhuber, A., Carroll, J., Ahnelt, P. K., & Drexler, W. (2009). Adaptive optics optical coherence tomography at 120,000 depth scans/s for non-invasive cellular phenotyping of the living human retina. *Optics Express*, *17*(22), 19382–19400. https://doi.org/10.1364/OE.17.019382

Ts'o, D., Schallek, J., Kwon, Y., Kardon, R., Abramoff, M., & Soliz, P. (2009). Noninvasive functional imaging of the retina reveals outer retinal and hemodynamic intrinsic optical signal origins. *Japanese Journal of Ophthalmology*, *53*(4), 334–344. https://doi.org/10.1007/s10384-009-0687-2

Tu, J. H., Foote, K. G., Lujan, B. J., Ratnam, K., Qin, J., Gorin, M. B., Cunningham, E. T., Tuten, W. S., Duncan, J. L., & Roorda, A. (2017). Dysflective cones: Visual function and cone reflectivity in long-term follow-up of acute bilateral foveolitis. *American Journal of Ophthalmology Case Reports*, *7*, 14–19. https://doi.org/10.1016/j.ajoc.2017.04.001

Tuten, W. S., Harmening, W. M., Sabesan, R., Roorda, A., & Sincich, L. C. (2017). Spatiochromatic interactions between individual cone photoreceptors in the human Retina. *Journal of Neuroscience*, *37*(39), 9498–9509. https://doi.org/10.1523/JNEUROSCI.0529-17.2017

Tuten, W. S., Tiruveedhula, P., & Roorda, A. (2012). Adaptive optics scanning laser ophthalmoscope-based microperimetry. *Optometry and Vision Science*, *89*(5), 563–574. https://doi.org/10.1097/OPX.0b013e3182512b98.Adaptive

Tuten, W. S., Vergilio, G. K., Young, G. J., Bennett, J., Maguire, A. M., Aleman, T. S., Brainard, D. H., & Morgan, J. I. W. (2019). Visual Function at the Atrophic Border in Choroideremia Assessed with Adaptive Optics Microperimetry. *Ophthalmology Retina*, *3*(10), 888–899. https://doi.org/10.1016/j.oret.2019.05.002

Venkateswaran, K., Roorda, A., & Romero-Borja, F. (2004). Theoretical modeling and evaluation of the axial resolution of the adaptive optics scanning laser ophthalmoscope. *Journal of Biomedical Optics*, *9*(1), 132. https://doi.org/10.1117/1.1627775

Vienola, K. V., Braaf, B., Sheehy, C. K., Yang, Q., Tiruveedhula, P., Arathorn, D. W., de Boer, J. F., & Roorda, A. (2012). Real-time eye motion compensation for OCT imaging with tracking SLO. *Biomedical Optics Express*, *3*(11), 2950. https://doi.org/10.1364/boe.3.002950

Vinas, M., Dorronsoro, C., Cortes, D., Pascual, D., & Marcos, S. (2015). Longitudinal chromatic aberration of the human eye in the visible and near infrared from wavefront sensing, double-pass and psychophysics. *Biomedical Optics Express*, *6*(3), 948. https://doi.org/10.1364/boe.6.000948

Waller, L., & Tian, L. (2015). 3D Phase Retrieval with Computational Illumination. *Imaging and Applied Optics*, *111*, CW4E.1. https://doi.org/10.1364/cosi.2015.cw4e.1

Wang, J., Yang, M., Yang, L., Zhang, Y., Yuan, J., Liu, Q., Hou, X., & Fu, L. (2015). Medical Instrumentation — Article A Confocal Endoscope for Cellular Imaging. *Engineering*, *1*(3), 351–360. https://doi.org/10.15302/J-ENG-2015081

Webb, R. H., & Hughes, G. W. (1981). Scanning Laser Ophthalmoscope. *IEEE Transactions on*

Biomedical Engineering, *BME-28*(7), 488–492. https://doi.org/10.1109/TBME.1981.324734

Webb, R. H., Hughes, G. W., Delori, F. C., Sahu, C., & Sahu, C. (2011). Confocal Scanning Laser Ophthalmoscope. *Comprehensive Notes in Ophthalmology*, *26*(8), 204–204. https://doi.org/10.5005/jp/books/11266_39

Wilson, T., & Carlini, A. R. (1987). Size of the detector in confocal imaging systems. *Optics Letters*, *12*(4), 227. https://doi.org/10.1364/ol.12.000227

Winter, S., Sabesan, R., Tiruveedhula, P., Privitera, C. M., Unsbo, P., Lundström, L., & Roorda, A. (2016). Transverse chromatic aberration across the visual field of the human eye. *Journal of Vision*, *16*(14), 1–10. https://doi.org/10.1167/16.14.9

Wojtkowski, M., Kowalczyk, A., Leitgeb, R., & Fercher, A. F. (2002). Full range complex spectral optical coherence tomography technique in eye imaging. *Optics Letters*, *27*(16), 1415. https://doi.org/10.1364/ol.27.001415

Wojtkowski, Maciej, Leitgeb, R., Kowalczyk, A., Bajraszewski, T., & Fercher, A. F. (2002). In vivo human retinal imaging by Fourier domain optical coherence tomography. *Journal of Biomedical Optics*, *7*(3), 457. https://doi.org/10.1117/1.1482379

Wojtkowski, Maciej, Srinivasan, V. J., Ko, T. H., Fujimoto, J. G., Kowalczyk, A., & Duker, J. S. (2004). Ultrahigh-resolution, high-speed, Fourier domain optical coherence tomography and methods for dispersion compensation. *Optics Express*, *12*(11), 2404. https://doi.org/10.1364/opex.12.002404

Wornson, D. P., Hughes, G. W., & Webb, R. H. (1987). Fundus tracking with the scanning laser ophthalmoscope. *Applied Optics*, *26*(8), 1500. https://doi.org/10.1364/ao.26.001500

Yang, Q., Arathorn, D. W., Tiruveedhula, P., Vogel, C. R., & Roorda, A. (2010). Design of an integrated hardware interface for AOSLO image capture and cone-targeted stimulus delivery. *Optics Express*, *18*(17), 17841. https://doi.org/10.1364/oe.18.017841

Yao, X., & Wang, B. (2015). Intrinsic optical signal imaging of retinal physiology: a review. *Journal of Biomedical Optics*, *20*(9), 090901. https://doi.org/10.1117/1.jbo.20.9.090901

Yazdanfar, S., Yang, C., Sarunic, M. V., & Izatt, J. A. (2005). Frequency estimation precision in Doppler optical coherence tomography using the Cramer-Rao lower bound. *Optics Express*. https://doi.org/10.1364/opex.13.000410

York, A. G., Chandris, P., Nogare, D. D., Hebert, T. J., Wawrzusin, P., Fischer, R. S., Chitnis, A. B., & Shroff, H. (2013). Instant super-resolution imaging in live cells and embryos via analog image processing. *Nature Methods*, *10*(11), 1122–1130. https://doi.org/10.1038/nmeth.2687

York, A. G., Parekh, S. H., Dalle Nogare, D., Fischer, R. S., Temprine, K., Mione, M., Chitnis, A. B., Combs, C. A., & Shroff, H. (2012). Resolution doubling in live, multicellular organisms via multifocal structured illumination microscopy. *Nature Methods*, *9*(7), 749–754. https://doi.org/10.1038/nmeth.2025

Yun, S., Tearney, G., de Boer, J., Iftimia, N., & Bouma, B. E. (2003). High-speed optical

frequency-domain imaging. *Optics Express*, 22(11), 2953–2963. https://doi.org/10.1364/OE.11.002953

Zawadzki, R. J., Capps, A. G., Kim, D. Y., Panorgias, A., Stevenson, S. B., Hamann, B., & Werner, J. S. (2014). Progress on developing adaptive optics-optical coherence tomography for in vivo retinal imaging: Monitoring and correction of eye motion artifacts. *IEEE Journal on Selected Topics in Quantum Electronics*, *20*(2), 322–333. https://doi.org/10.1109/JSTQE.2013.2288302

Zawadzki, R. J., Cense, B., Zhang, Y., Choi, S. S., Miller, D. T., & Werner, J. S. (2008). Ultrahigh-resolution optical coherence tomography with monochromatic and chromatic aberration correction. *Optics Express*, *16*(11), 8126. https://doi.org/10.1364/oe.16.008126

Zawadzki, R. J., Jones, S. M., Olivier, S. S., Zhao, M., Bower, B. A., Izatt, J. A., Choi, S. S., Laut, S., & Werner, J. S. (2005). Adaptive-optics optical coherence tomography for high-resolution and high-speed 3D retinal in vivo imaging. *Optics Express*, *13*(21), 8532. https://doi.org/10.1364/opex.13.008532

Zawadzki, R. J., Jones, S. M., Pilli, S., Balderas-Mata, S., Kim, D. Y., Olivier, S. S., & Werner, J. S. (2011). Integrated adaptive optics optical coherence tomography and adaptive optics scanning laser ophthalmoscope system for simultaneous cellular resolution in vivo retinal imaging. *Biomedical Optics Express*, *2*(6), 1674–1686. https://doi.org/10.1364/BOE.2.001674

Zhang, F., Kurokawa, K., Lassoued, A., Crowell, J. A., & Miller, D. T. (2019). Cone photoreceptor classification in the living human eye from photostimulation-induced phase dynamics. *Proceedings of the National Academy of Sciences of the United States of America*, *116*(16), 7951–7956. https://doi.org/10.1073/pnas.1816360116

Zhang, P., Zawadzki, R. J., Goswami, M., Nguyen, P. T., Yarov-Yarovoy, V., Burns, M. E., & Pugh, E. N. (2017). In vivo optophysiology reveals that G-protein activation triggers osmotic swelling and increased light scattering of rod photoreceptors. *Proceedings of the National Academy of Sciences of the United States of America*, *114*(14), E2937–E2946. https://doi.org/10.1073/pnas.1620572114

Zhang, Y., Rha, J., Jonnal, R. S., & Miller, D. T. (2005). Adaptive optics parallel spectral domain optical coherence tomography for imaging the living retina. *Optics Express*, *13*(12), 4792. https://doi.org/10.1364/opex.13.004792

Zhenghan, L., Pandiyan, V. P., Maloney-Bertelli, A., Jiang, X., Li, X., & Sabesan, R. (2020). Correcting intra-volume distortion for AO-OCT using 3D correlation based registration. *Optics Express*, *28*(25), 38390. https://doi.org/10.1364/oe.410374

Zhu, D., Fang, Y., Chen, Y., Hussain, A., Kuang, C., Ding, Z., & Liu, X. (2017). Comparison of multi-mode parallel detection microscopy methods. *Optics Communications*, *387* (December 2016), 275–280. https://doi.org/10.1016/j.optcom.2016.11.067

Zhu, J., & Yang, J. (2002). Subpixel eye gaze tracking. *Proceedings - 5th IEEE International Conference on Automatic Face Gesture Recognition, FGR 2002*, 131–136. https://doi.org/10.1109/AFGR.2002.1004144